COMPOSITIONAL AND FUNDAMENTAL CHARACTERIZATION OF LI-ION CELL ELECTROLYTES

by

Tina Taskovic

Submitted in partial fulfilment of the requirements
for the degree of Master of Science

at

Dalhousie University
Halifax, Nova Scotia
August 2020

To my family in Halifax, Peterborough and Kragujevac

TABLE OF CONTENTS

LIST OF TABLES

LIST OF FIGURES

ABSTRACT

The electrolyte is crucial to successful lithium ion cell operation. The composition, including the solvents and additives used will dictate how long the cell lasts. There are only a few studies that study the electrolytes from cells that have gone through a prolonged cycling sequence, even fewer that do this while focusing on specific additive combinations. This work studies a matrix of Li-ion cells with additives vinylene carbonate and ethylene sulfate to determine which additive combination is optimal for long cell lifetimes. The results are determined through a novel electrolyte extraction technique that uses NMR and GC-MS to quantify known electrolyte components and identify unknowns.

The extraction method and NMR/GC-MS method are presented in this work along with the results from the tested cells. Cells with 1 or 2% VC and 1% DTD had the most stable cycling performance but a surprising amount of electrolyte salt consumption. μ-XRF transition metal analysis of the negative electrodes are also presented. The possible degradation mechanisms of electrolytes were described but the cells tested were absent of any such products. Many additional projects using the NMR/GC-MS method described are proposed as future work.

Lastly, NMR was used to additionally determine some transport properties of Li-ion cell electrolytes. Results found salts in methyl acetate to have faster diffusion rates compared to a DMC solution. The technique will be further used to measure physicochemical properties of modern Li-ion cell electrolytes

LIST OF ABBERIVATIONS AND SYMBOLS USED

CEI	Cathode electrolyte interphase
CPE	Constant phase element
DEC	Diethyl carbonate
DEOHC	Diethyl-2,5-dioxahexane carboxylate
DMC	Dimethyl carbonate
DMOHC	Dimethyl-2,5-dioxahexane carboxylate
DOSY	Diffusion-ordered spectroscopy
DTA	Differential thermal analysis
DTD	Ethylene sulphate
EC	Ethylene carbonate
EIS	Electrochemical impedance spectroscopy
EMC	Ethyl methyl carbonate
EMOHC	Ethyl methyl-2,5-dioxahexane carboxylate
ES	Ethylene sulphite
EV	Electric vehicle
FEC	Fluoroethylene carbonate
FEP	Fluorinated ethylene propylene
FID	Free induction decay
GC-MS	Gas chromatography- Mass spectroscopy
HOMO	Highest occupied molecular orbital
HP-LC	High pressure liquid chromatography
LC-MS	Liquid chromatography – mass spectroscopy
LCO	Lithium cobalt oxide
LEDC	Lithium ethylene dicarbonate
LEMC	Lithium ethylene mono-carbonate
LFP	Lithium iron phosphate
LPF	Lithium difluorophosphate
LMO	Lithium manganese oxide
LUMO	lowest unoccupied molecular orbital
LiDFOB	Lithium difluoro(oxalate)borate
LiTFOP	Lithium tetrafluoro(oxalato)phosphate
MA	Methyl Acetate
NaCMC	Sodium carboxymethylcellulose
NCA	Nickel cobalt aluminium
NMC	Nickel manganese cobalt
NMC111	$LiNi_{0.33}Mn_{0.33}Co_{0.33}O_2$
NMC532	$LiNi_{0.5}Mn_{0.3}Co_{0.2}O_2$

NMR	Nuclear magnetic resonance spectroscopy
PC	Propylene carbonate
PEG	Polyethylene glycol
PFG-NMR	Pulse field gradient-nuclear magnetic resonance spectroscopy
PULCON	Pulse length-based concentration determination
PVDF	Polyvinylidene fluoride
RF	Radio frequency
Rct	Charge transfer resistance
Rs	Solution resistance
SALLE	Salt assisted liquid-liquid extraction
SBR	Styrene butadiene rubber
SEI	Solid electrolyte interphase
TMNSNCS	(trimethylsilyl)isothiocyanate
VC	Vinylene carbonate
W	Warburg impedance
d-DMSO`	Deuterated dimethyl sulfoxide
μ-XRF	Micro-X-ray fluorescence

1D	One dimensional
2D	Two dimensional
A+	Cation fragment
AB	Molecule
B_o	Magnetic field strength
c_s	Number density of molecules
D	Diffusion coefficient
Dκ	Charge diffusivity
dQ/dV	Differential capacity
ΔV	Voltage polarization
G_i	Gradient strength
I	Nuclear spin quantum number
I	Intensity
I_o	Initial intensity
κ	Specific conductivity
k_B	Boltzmann constant
M_o	Net magnetisation vector
π	pi constant
Q	Capacity
Qc	Charge capacity
Q_d	Discharge capacity

T	Temperature
T_1	Spin-lattice relaxation
V	Voltage
E	Electron
$f\pm$	Activity coefficient
$\hbar$	Plank's constant
m	Spin-state
n	Number of samples
t^+	Transference number
t_R	Retention time
γ	Gyromagnetic ratio
Δ	Signal delay time
δ	Gradient width
σ	Standard deviation
ν	Larmour frequency

ACKNOWLEDGEMENTS

I would like to thank the Nova Scotia government, NSERC and Tesla Canada for partial funding of this work.

I would like to extend a deep gratitude to my supervisor, Dr. Jeff Dahn for his time, mentorship, feedback, passion, and encouragement. I am extremely thankful and humbled to learn from him and to become a better research scientist. I would also like to extend my sincere thanks to Dr. Mita Dasog for her support and guidance as my committee member.

I am also grateful to Lea Gawne along with the graduate chemistry office for their help throughout my degree. Special thanks to Dr. Mike Lumsden for his support and his NMR expertise. Thanks, should also go to Dr. Gianna Aleman, for her support and inspiring me to becoming a better teacher.

I am also incredibly thankful and inspired by the past and current members of the Dahn lab for their support, wisdom, and valued friendship. I am truly blessed to work with so many kind-hearted and hard-working people.

I am very thankful to my family for their love, encouragement, and reality checks. I also want to thank my friends in and out of the chemistry department for their friendship, support, and laughs throughout this degree.

Lastly, I would like to thank my furry friend Gerald for his comfort in getting though this pandemic and the thesis process.

CHAPTER 1 – INTRODUCTION

1.1 Justification

Over the past year, the world has seen public demand for action on issues of climate and environment increase dramatically.[1] This increase in interest is primarily led by the frustration of youth across the world. Most notably activists like Greta Thunberg from Sweden and Autumn Peltier from Canada have emphasized that climate change is a human rights issue with women, people of colour and other marginalized communities, likely to be disproportionately affected by climate change.[2–4]

Luckily, many countries have established targets to lower emissions, but it is yet to be determined if they take these targets seriously.[5,6] Canada, for example, has the goal to reach net-zero emissions by 2050. According to the Center for Climate and Energy Solutions, energy production of all types (electricity, heat, transportation) accounts for 72% of all global emissions, and subsequently, resources are being heavily invested into renewable, emission-free energy technologies.[7]

One of the most prevalent symbols of emission-free technology is the electric vehicle. Many countries are implementing policies to mandate the removal of combustion engines, and thus, battery research and manufacturing is rapidly expanding.[8] The battery of choice for most electric vehicles is the lithium-ion due to its long cycle life and high energy density.[9] They are the storage device also found in cell phones, laptops, and power tools, as well as in larger devices such as home and large-scale gird energy storage. It is estimated that the market for LIBs both for large and small scale applications is expected

to reach $129.3 billion (USD) by 2027.[10] However, many improvements are desired to reduce cost, improve lifetime, energy density and safety.

This thesis presents work primarily focusing on how to improve lithium-ion cell lifetimes with the spotlight on how making small changes to the electrolyte can result in significant improvements. Another portion of the thesis tries to understand why a specific electrolyte blend was so successful through using a variety of analysis techniques.

1.2 Li-ion cells

A Li-ion cell is an electrochemical storage device that uses electrode materials that can store lithium atoms. Figure 1.1 shows an example of a lithium-ion pouch cell, with only the external connections seen. Figure 1.2 shows a schematic of a Li-ion cell during charge and discharge. Figure 1.2a shows how the lithium atoms move from the anode (negative electrode) through the electrolyte to intercalate back into the cathode (positive electrode) during discharge. The movement of positive charge will be balanced by the flow of electrons from the negative electrode to the positive electrode resulting in a generated current throughout the external circuit. Concurrently, the potential of the positive electrode would decrease while the negative electrode increases until the lower discharge potential is reached (Figure 1.3).

During charge shown in Figure 1.2b, an electric current is provided to the cell, causing electrons to flow into the negative electrode. To balance the charge, Li^+ cations then travel through the electrolyte and intercalate between the graphene layers. During charge, the lithiated negative electrode potential decreases to ~0.08 V vs. Li/Li^+ (Figure 1.3a).

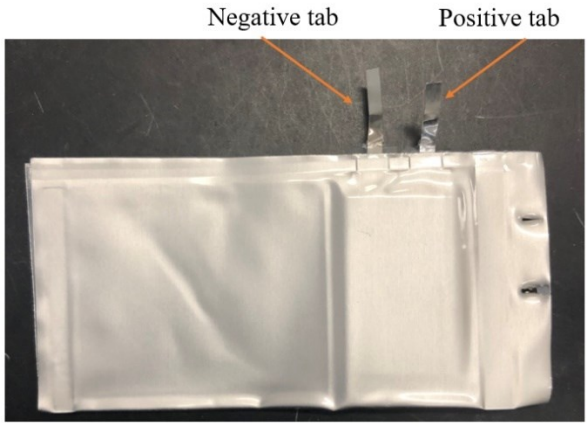

Figure 1.1 A pouch cell that is used in this work, showing the size of the cell (40 mm long, 20 mm wide, 3.5 mm thick) with additional gas bag and electrical connections.

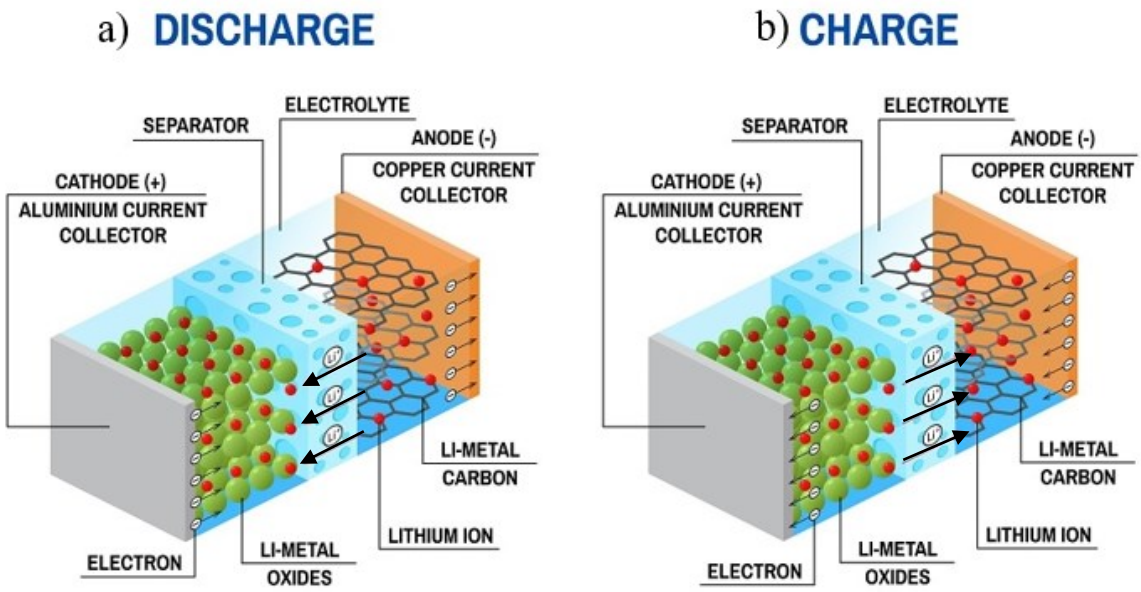

Figure 1.2 a) Li-ion cell during discharge. b) Li-ion cell during charging.[11]

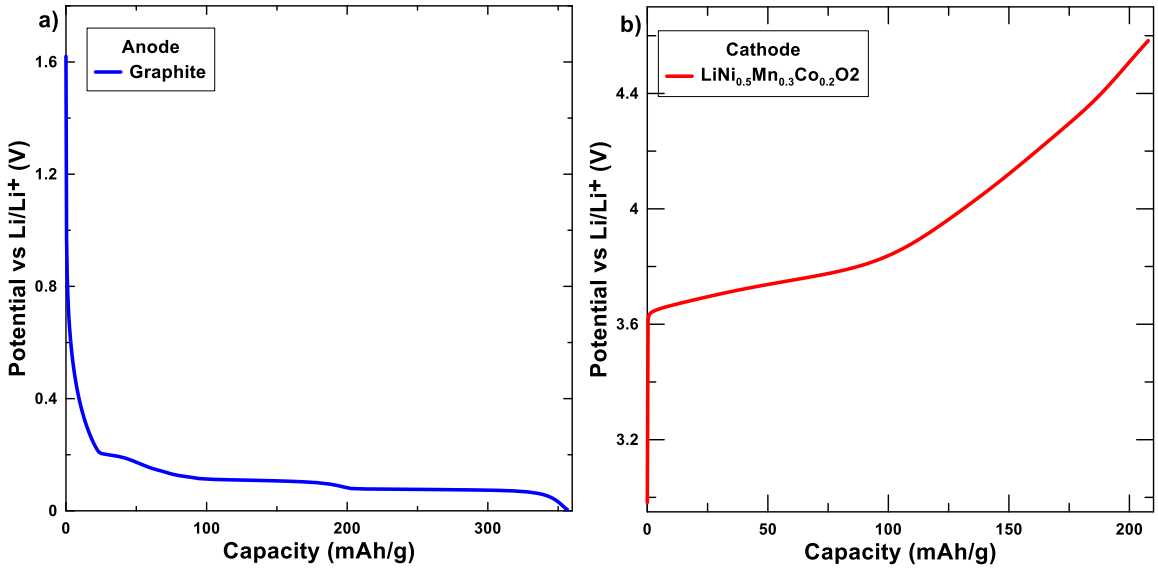

Figure 1.3 a) Voltage profiles for a) graphite anode and b) $LiNi_{0.5}Mn_{0.3}Co_{0.2}O_2$ cathode

while the delithiated positive electrode potential increased up to 4.3 V vs. Li/Li^+ (Figure 1.3b), the difference between the electrode potentials determines the potential of the full Li-ion cell. Figure 1.4 shows a partially opened pouch cell with its components partially unwound. The negative electrode is separated from the positive electrode by a separator. The negative electrode adheres to a copper current collector while the positive electrode uses an aluminum current collector. Both electrodes are connected to tabs at the end of the cell. The entire cell is wound together in a "jelly roll" then cased in a pouch bag made of a plastic-aluminum laminate.

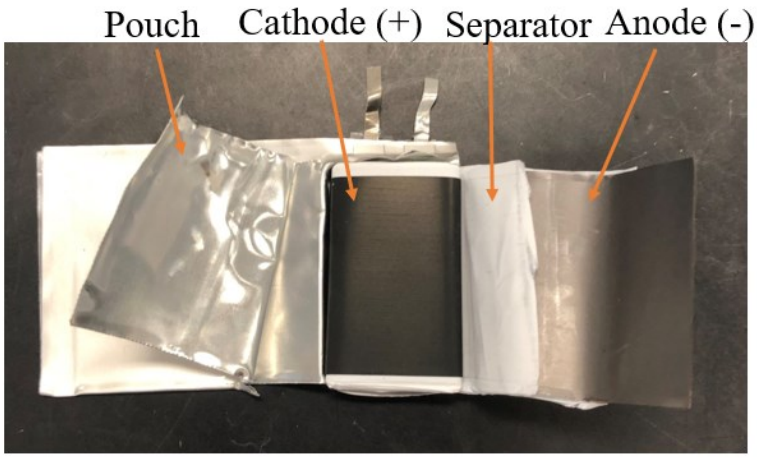

Figure 1.4 The inside components of a pouch cell with the jelly roll (anode, separator and cathode) visible.

1.3 Negative electrode

In Li-ion cells, the negative electrode is mainly graphite with small amounts of binder and conductive additive to ensure that the graphite particles are adhered together and are electrically connected to the copper current collector. Graphite is comprised of layers of graphene held together by weak Van der Waals forces allowing lithium ions to intercalate without significant structural changes. During charge, the lithium atoms intercalate between the graphene layers as per reaction:

$$yLi^+ + ye^- + C \rightarrow Li_yC. \quad (0 \leq y \leq 1) \qquad (1.1)$$

The reaction concurring on the positive electrode is given by:

$$Li[M]O_2 \rightarrow xLi^+ + xe^- + Li_{1-x}[M]O_2. \qquad (0 \leq x \leq 1) \qquad (1.2)$$

/*

The overall reaction is given by:

$$Li[M]O_2 + yC_6 \rightarrow Li_{1-x}[M]O_2 + yLi_{x/y}C_6. \quad (1.3)$$

Theoretically, the maximum storage capacity is 372 mAh/g for the LiC_6 phase. The negative electrode is shown in Figure 1.4.

Besides graphite, other materials of interest like silicon and graphite-silicon composites are explored as a silicon anode has a theoretical specific energy of 3600 mAh/g. However, the mechanism differs; instead of intercalation, the alloying of lithium to silicon causes extreme volume expansions leading to rapid capacity losses. Despite this, some Li-cell manufacturers are using silicon in their graphite to increase energy density.

1.4 Positive electrode

Positive electrode materials are commonly layered transition metal oxides like $LiNi_xMn_yCo_xO_2$ (NMC), $LiNi_xCo_yAl_yO_2$ (NCA), and $LiCoO_2$ (LCO) along with a binder and conductive additives that ensure proper adherence to the aluminum current collector and electrical conductivity. Other positive electrode materials having different crystallographic structures like olivine $LiFePO_4$ (LFP) and spinel $LiMnO_2$ (LMO) are also used in commercial Li-ion cells.[12,13] Nickel-containing materials take on a layered structure where the lithium-atoms are stored between the transition-metal/oxygen slabs. Upon charging, the Li atoms are removed from the material as it oxidizes, the spacing between the layers changes, but overall, the structure maintains its integrity.

This study will use $LiNi_{0.5}Mn_{0.3}Co_{0.2}O_2$ (NMC532), where the subscripts show the molar fraction of each transition metal. The current trend in the industry with positive

electrode materials is to increase the nickel content, thereby increasing specific capacity.[14] Higher nickel content results in shorter cell lifetimes and thermal instability. Another trend is to decrease the cobalt content due to ethical issues related to cobalt mining. The cathode material selected to be used in Li-ion cells depends on what concessions are willing to be made on specific capacity, thermal stability, and cost.

1.5 Electrolyte

The role of the electrolyte is to facilitate the exchange of Li-ions between the electrodes during cell operation. It is made of a dissolved lithium salt in organic solvents. The electrolyte is ionically conductive and electrically insulating and it should be resistive to reacting with charged electrode materials.

The most common lithium salt is lithium hexafluorophosphate ($LiPF_6$); it is highly soluble in polar organic solvents giving high ionic conductivity. Figure 1.5 shows the structure of several carbonate solvents that are used in Li-ion cells. Most modern electrolytes contain ethylene carbonate (EC) and one or more linear carbonates.[15,16]

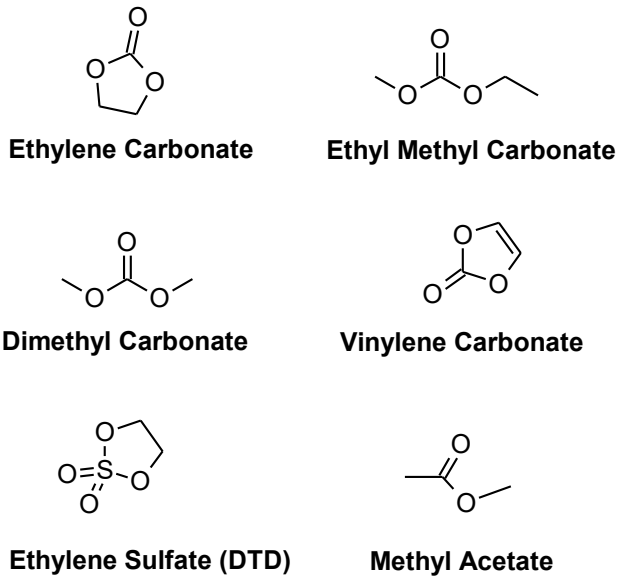

Figure 1.5 Chemical structure of some electrolyte solvent and additives.

An ideal electrolyte would have an electrochemical window larger than the operating potentials of the electrodes, low viscosity to promote Li-ion diffusion, and a high dielectric constant. It is also essential that the electrolyte remains liquid in a wide temperature range, is stable against other cell components, is safe, and has low toxicity and cost.

Chapter 2 goes into more detail about electrolytes for Li-ion cells and the unwanted reactions that can happen with charged electrode material surfaces.

1.6 Solid electrolyte interphase (SEI) on the negative electrode

Unfortunately, there are no electrolytes that can operate at the extreme potentials of Li-ion cell electrodes without reacting. Nevertheless, the cell operates due to the formation of the solid electrolyte interphase (SEI) comprised of the electrolyte reduction products when the cell is first charged. The SEI prevents long-term capacity losses from further reactions

between the electrolyte and electrode. This layer is passivating, ionically conductive, but electrically insulating. It is comprised of compounds that allow Li-ions to pass through, but further electrolyte reduction is impeded by the limited electron transport. A good SEI is also stable with time and temperature.

The mechanism(s) of how the Li-ion transports through the SEI from the bulk electrolyte is still unclear. It is known that this step is a barrier to efficient Li-ion transport. Li cations must get desolvated upon the surface of the SEI then migrate through the SEI to get intercalated into the graphite.[17] Various computational methods have been used to study this mechanism but are limited in scope due to the complexity of the SEI.[18] Our current understanding has been mostly a result of experimental work.

EC-based electrolytes result in an SEI that is primarily composed of the products of the reaction of EC with lithium.[19] However, simultaneously, the reduction of salts and other compounds can occur.

It was found that the composition of the SEI can be altered by adding compounds that have a reduction potential above EC.[20] The addition of such compounds has been shown to lower resistivity and provide better stability for the cell. Figure 1.5 also shows the structure of vinylene carbonate (VC) and ethylene sulphate (DTD), which are additives known to help improve cell lifetimes. They are added to the electrolyte in small amounts making up < 5 wt% in total.

The use of additives has been described as a “dark art” with little basis for using a specific compound.[21] This area of electrolyte development is also considered one of the most economical ways to improve Li-ion cells. However, it can be time-intensive, due to

the random nature of additive selection. Therefore, investing in understanding the fundamental chemistry and electrochemistry of additives should be a priority.

The term SEI was first introduced in 1979 by Peled.[22] Later in 1997, he suggested a mosaic structure for the SEI comprised of both organic and inorganic (Li -containing) insoluble or partially soluble compounds.[23] Since then, several other models of the SEI have been proposed.[18] It is generally accepted that the SEI thickness is between ~10-50 nm thick.[24–27] Figure 1.6 is a model of the SEI by Nie et al.[28] By analyzing the surfaces of cycled negative electrodes through various techniques, the group managed to deduce some components of the SEI.

In EC/$LiPF_6$ based electrolyte, the SEI produced in the work by Nie et al. is primarily composed of lithium ethylene dicarbonate (LEDC) and lithium fluoride (LiF). Chapter 2 will discuss the possible mechanism for the formation of LEDC and LiF. It should be noted that recently, after many years of consensus that LEDC is a component of the SEI, Wang et al, argue lithium ethylene mono-carbonate (LEMC) is in the primary SEI component and was mistaken for LEDC.[29] LEMC they argue has a significantly higher ionic conductivity compared to LEDC allowing for facile Li^+ diffusion. However, this work needs to be corroborated, but this discovery highlights the complexity and fluctuating nature of SEI research.

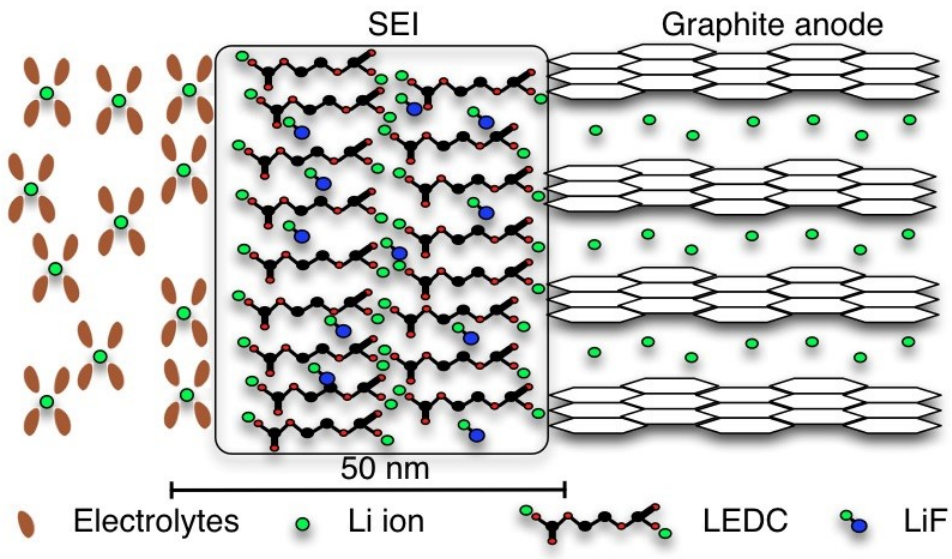

Figure 1.6 Figure from a 2013 publication by Nie et al[28] shows a schematic figure of SEI formed on graphite anodes during the first cycle. Reproduced with permission from *J. Phys. Chem. C,* **2013**, *117* (3), 1257–1267. Copyright 2013, American Chemical Society

The electrolyte used in a Li-ion cell dictates the composition and thickness of an SEI. The study by Nie et el, using no additives, provided information on what the SEI looks like on a fundamental level, however, most commercial cells use some type of additive, and their addition can dramatically change the composition.[28] Figure 1.7 shows a schematic of different SEI's by Madec et al. They studied the composition of the SEI with and without the additives VC and ES (ethylene sulfite).[30] They used x-ray photoelectron spectroscopy to determine the composition and relative thicknesses of SEIs of NMC111/graphite cells filled with 1M $LiPF_6$ in EC: EMC(3:7 wt). VC and ES were added in a 2 wt% amount, either solely or in combination. They tested cells repeatedly cycled and compared to cells that had only undergone a single cycle (formation).

Madec et al. used the repetition of species and the size of the text font in Figure 1.7 to represent the relative amount of each product in the SEI. The positioning of each compound estimates the location of species in the SEI layer, suggesting non-uniformity.

Most theories about the SEI composition suggest a non-uniform SEI.[31,32] Unlike the previous model, this work found evidence of lithium alkyl carbonates ($ROCO_2Li$) as a significant product in all electrolytes tested. However, similarly to Nie's work, LiF was found to be present in all SEI layers regardless of additives. LiF was found to be more present in the graphite/SEI interphase, where organic species were found more on the outskirts of the SEI. A significant amount of lithium oxide (Li_2O) was found in the control cells tested. Li_2O forms from further reduction of carbonate degradation compounds.[24] However, cells containing VC or ES found that Li_2O formation was suppressed, thus suggesting that the additives limit adverse reaction pathways.

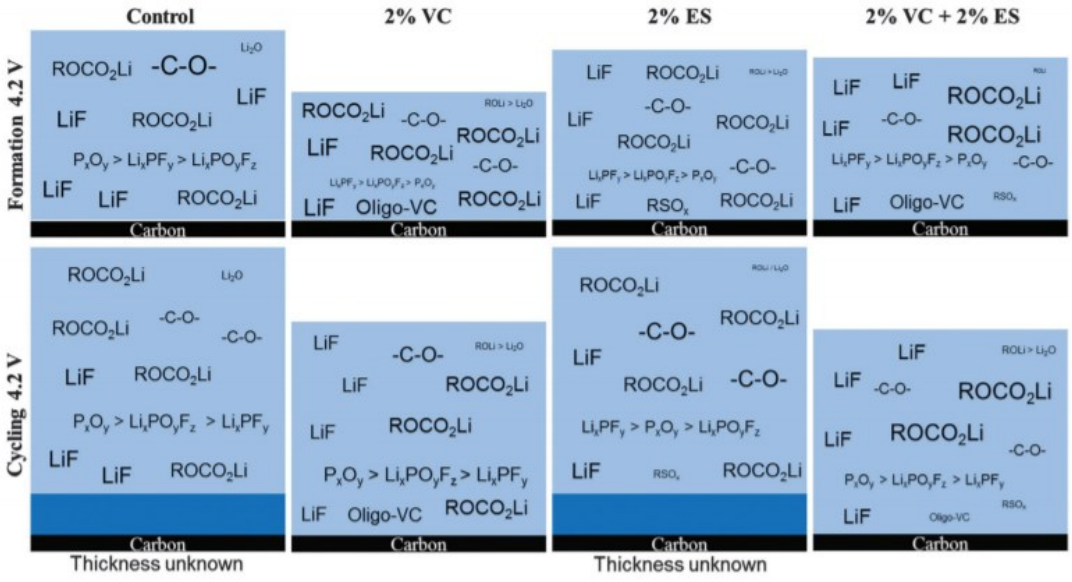

Figure 1.7 Figure from a 2015 publication by Madec et al[30] shows a schematic of the SEI formed on graphite anodes during the first cycle and cycling to 4.2V. Reproduced with permission from *Phys. Chem. Chem. Phys.* **2015**, *17* (40), 27062–27076. Copyright 2015, The Royal Society of Chemistry

Li_2O, also, is an inorganic compound that is a result of side reactions that can also produce Li_2CO_3, lithium fluorophosphates, lithium alkoxides, and lithium carboxylates, to name a few.[33] In the Madec paper, cells that contained VC had a thinner SEI and were

found to have a slightly higher organic content. A VC oligomer was detected in VC and VC+ES cells. Also, cells with VC had LiF dispersed more evenly throughout the SEI. Cells that contained ES only had SEIs that were thinner than control cells and had a higher inorganic component compared to VC only. Cells with ES only had an SEI that thickened during cycling significantly and included sulphur species. Combined, the presence of ES and VC, resembled the SEI of VC only cells with additional LiF, along with similar thicknesses.

LiF has low ionic and electron conductivity. LiF is thought to be crucial in blocking electron transfer from the graphite to the electrolyte.[18,34,35] Lastly, LiF is thermodynamically stable as a reduction product so the compound provides stability to the SEI. However, it is unclear why more LiF is produced when VC and ES are combined.

Modelling the SEI is a continual effort, but very challenging once additives are introduced. Recently, a model of the SEI created by Qian et el.[20] shown in Figure 1.8 compared VC and lithium difluorophosphate (LPF), another additive known to help promote Li-ion cell lifetimes. They used NMC532/graphite pouch cells with a base electrolyte consisting of 1M $LiPF_6$ in EC:DEC (3:7 wt). The additives were combined and tested separately against an additive-free cell. They also showed the cathode-electrolyte interphase (CEI) in their models. The CEI is also passivating but considered to be more stable compared to the SEI (at lower voltages) hence why SEI improvement and study have been a priority.

The model by Qian et al. was developed by testing two different additives in a similar manner to Madec et al. This paper is valuable as it discusses possible reasons behind the synergistic effect between the two additives. Figure 1.8 agrees with Madec et al that

VC only cells produce an SEI with a more significant portion being organic.[30] Figure 1.8 also agrees with Madec et al in that both models also discuss the presence of Li_2O in VC only cells. Figure 1.8 differs from Figure 1.7 by showing a more significant amount of Li_2CO_3 in the SEI of all the cells tested. Li_2CO_3 is found to be usefu1 in Li-transport across the SEI.[36]

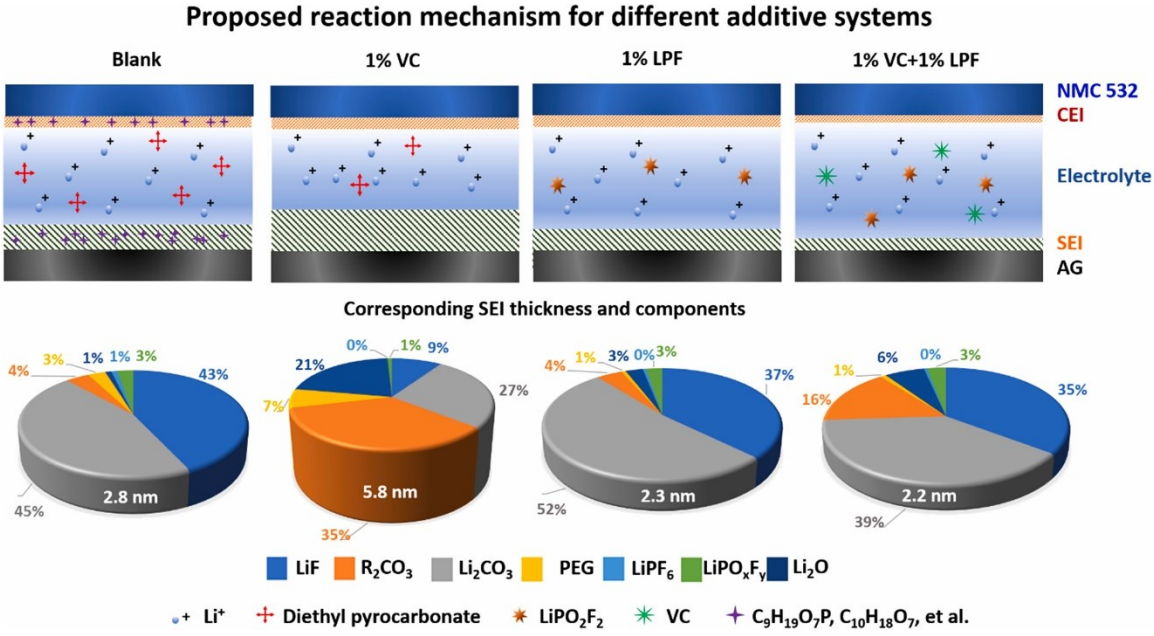

Figure 1.8 Figure from a 2019 publication by Qian et al[20] shows different schematics of the effect of additives on the SEI & CEI formation and electrolyte decomposition of NMC532/AG pouch bag cells, with the specific atomic ratio of different components in the corresponding SEI on the anode. Reproduced with permission from *Energy Storage Mater*. 2019, 20, 208–215. Copyright 2018, Elsevier B.V

Figure 1.8 shows that the thinnest SEI was produced when the two additives tested 1%VC +1%LPF were put into a cell together. Their theory is that LPF suppresses the consumption of VC enough that it still provides the passivating qualities from the organic content (R_2CO_3) without increasing impedance. Li_2O is present in the dual additive combination but in a lower quantity, and the overall inorganic portion has increased (LiF and Li_2CO_3) compared to the VC only cell. From this article, it is implied that a higher

fraction of inorganic compounds in the SEI tends to produce better SEIs. This agrees with Madec et al. despite the use of different electrolyte blends in their studies.

Overall, making models and analyzing the SEI is a way to understand the effect of additives on Li-ion cell performance. However, this thesis aims to understand if bulk electrolyte degradation occurs with additives and, if so, to what extent. Improving the electrolyte is an underappreciated and a far more economical approach to improving Li-ion cell lifetimes and energy density. Findings and techniques used in this work will hopefully be useful in guiding future electrolyte designs.

1.7 *Outline of the thesis*

Chapter 2 discusses modern electrolytes and specific electrolyte degradation reactions.

Chapter 3 discusses the methods used and developed to study the aged cells in this work.

Chapter 4 discusses the results using NMC532 cells containing various combinations of the additives VC and DTD. This work in chapter 4 has been prepared for publication and is waiting for approval to publish from Tesla.

Chapter 5 Introduces using Pulse field gradient NMR for measurements of Li-ion cell electrolytes. Methods and Results are described.

This work is published in The Journal of Physical Chemistry C, Ester-Based Electrolytes for Fast Charging of Energy Dense Lithium-Ion Batteries, E. R. Logan, D. S. Hall, Marc M. E. Cormier**, T. Taskovic**, Michael Bauer, Ines Hamam, Helena Hebecker, Laurent Molino, and J. R. Dahn. 2020, 124, 23, 12269-12280.

Chapter 6 summarizes the findings in chapters 4 and 5 and discusses future work.

CHAPTER 2 – OVERVIEW OF ELECTROLYTE SYSTEMS AND REACTIONS

Non-aqueous electrolytes used in Li-ion cells are a mix of lithium salts and organic solvents. The primary role of the electrolyte is to act as the medium in which ions can move between electrodes while being electronically insulating. The lithium-ion cell is a hostile environment, where many unwanted reactions can occur.[37] The main reason behind the instability comes from the fact that the potentials of the Li-ion cell electrodes are normally outside of the electrochemical stability window of the electrolyte. Specifically, the negative electrode has an electrochemical potential above the lowest unoccupied molecular orbital (LUMO) of the electrolyte.[38] When this happens it is thermodynamically favorable for the electrolyte to reduce. Luckily, the stability window is maintained due to the formation of the SEI. Modern electrolytes are all tailored to create a passivating layer on the negative electrode.

The electrolyte needs to support fast ion solvation and desolvation to enable the desired charge and discharge rates.[17] Ionic conductivity must also be high (>1 mS/cm) to allow for sufficient rate capacbility.[39] It must be thermally stable at the temperature of operating and stored cells. Safety is another critical factor; electrolytes should have high flashpoints and low toxicity. Lastly, it is desired that electrolytes have low production and materials cost and to be made of sustainable materials.[37]

2.*1 Modern Electrolytes*

One of the significant enablers to successful Li-ion cells was the realization that was using the solvent propylene carbonate (PC) over EC lead to severe structural damage to the graphite.[40] Figure 2.1 shows the chemical structure of PC. PC was initially used as it has a lower melting point (-48.8°C) compared to EC (36.4°C). PC was shown later to be unable to form a stable SEI. It is incredible that a single methylene group delayed the development of Li-ion cells for a few years. Fong et al. were the ones to discover that a passivating SEI on the graphite could be created by using EC.[41] EC is now considered an indispensable solvent for Li-ion batteries.

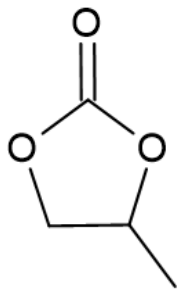

Figure 2.1 Chemical structure of propylene carbonate

Modern electrolytes also contain one or more linear carbonates to create a mixture with a melting point below room temperature.[42] Electrolyte blends have an EC content typically in the 35-30% range by weight. Linear carbonates typically have low viscosity and low dielectric constants. EMC is commonly chosen for its electrochemical stability window and low melting point.[43] However, using EMC or other linear carbonates alone does not produce a stable SEI.

The last major component of modern Li-ion battery electrolytes is the salt. The salt picked should provide stability for the solution and allow Li-ions to transport easily. The

salt should be electrochemically stable over the operating potentials. In addition, the salt should be thermally stable, cheap, and inert to the other cell parts.[42]

The most common salt used in commercial cells is $LiPF_6$, as it provides high conductivity and has good safety properties.[37] $LiPF_6$ was chosen as it has a decent conductivity, thermal and electrochemical stability. $LiPF_6$ is stable on carbon substrates up to 4.4 V is Li/Li^+ and $LiPF_6$ is less reactive to the aluminum current collector compared to other salts.[44,45] At high temperatures, $LiPF_6$ can decompose into LiF and PF_5, resulting in reactions with the electrolyte.[46] $LiPF_6$ is also very reactive with water; reacting to form HF.[12] $LiPF_6$ is therefore made in anhydrous conditions, leading to some additional costs.

The salt concentration is selected to maximize ion conductivity and Li^+ diffusivity. Diffusivity and conductivity depend on the viscosity of the electrolyte and the dielectric constant. Figure 2.2 shows multiple examples of the relationship between conductivity and salt concentration.

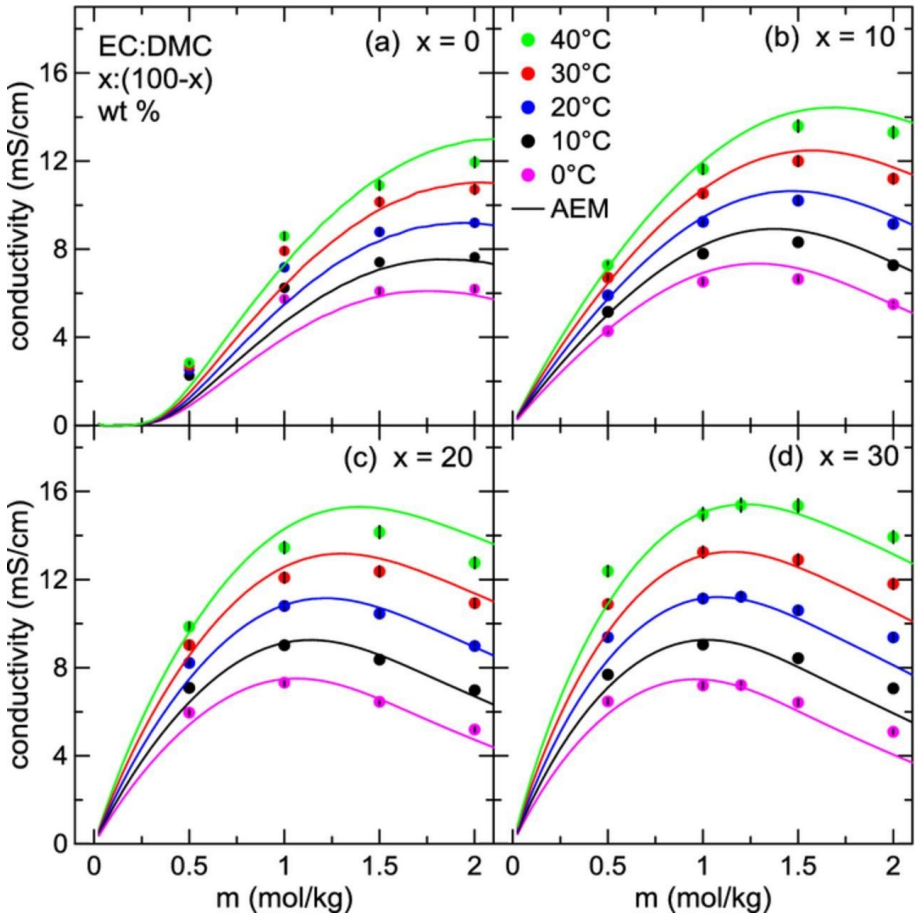

Figure 2.2 Ionic conductivity as a function of $LiPF_6$ concentration for electrolytes containing solvent mixtures (a) DMC, (b) EC:DMC 10:90, (c) EC:DMC 20:80, and (d) EC:DMC 30:70 (wt. %) for temperatures between 0°C and 40°C. Calculations from the AEM (Advanced electrolyte model) are shown as solid lines. Reproduced with permission from *J. Electrochem. Soc.* **2018**, *165* (3), 705–716. Copyright 2018, The Electrochemical Society. (CC BY 4.0)

Figure 2.2 also shows that for any solvent, at low salt concentrations the relationship to conductivity is linear. In this region the viscosity is low, and the dielectric constant is high. The curve then reaches a maximum conductivity, where the corresponding concentration would be ideal for that solvent. Once past that point, the conductivity starts to dip. This is due to an increase in viscosity and ion-pairing which both result in the hindering of ionic motion.[39,47]

Figure 2.2 also shows that conductivity and viscosity are dependent on temperature. High temperatures usually lead to lower viscosity electrolytes allowing for the salt concentration to increase and, therefore, give even higher conductivity.[48] Most electrolytes for commercial cells will have salt concentrations ranging from 1.0-1.5 M depending on solvents used and operating temperature.

A perfect electrolyte used in a lithium-ion cell would not react with other cell components or change in composition over its lifetime. Unfortunately, electrolytes go through changes caused by a variety of reactions. These reactions are either electrochemical or chemical, resulting in decomposition of the electrolyte during charge-discharge cycling or storage. The reduction and oxidation of the electrolyte can happen at the surfaces of the electrodes, with additional reactions involving reaction products. Changes to the surfaces of the electrode materials are also a possibility.[49] The kinetics of these reactions vary, completing over the course of days to decades.[50,51] Studies that identify electrolyte changes and components are typically limited to short-term tests at highly elevated temperatures. There are a limited number of studies that investigate electrolyte changes over-long term. In the subsequent parts of this chapter, common electrolyte reactions are reviewed to help provide context for the results in Chapter 4.

2.2 Electrolyte Reduction

When the negative electrode reaches low voltages vs. Li/Li^+ for the first time, the electrolyte will reduce at the interface.[52] As mentioned previously, this is where the SEI is formed. If sacrificial additives are used, they are preferably reduced at a higher voltage (vs. Li/Li^+) to modify the SEI for the better. The reduction mechanism of EC and linear

carbonates will be discussed. It is also common to see electrolyte reduction schemes to show the added electron to be paired with a neutralizing lithium cation. This is done to show the electronic neutrality of the electrolyte.

Figure 2.3 shows the EC reduction reaction occurring with either two electrons (Figure 2.3 a) or one (Figure 2.3 b).[15] The reduction creates a radical carbonate anion intermediate in the first step, followed by further reaction with another radical species to terminate the reaction. The intermediates produced in the reduction reactions for EC and the linear carbonates can combine in more ways than the examples shown.

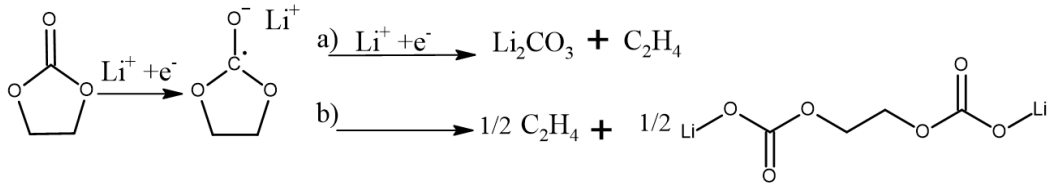

Figure 2.3 Reduction reactions of EC (routes a and b).

Figure 2.3 route (a) shows the two-electron reduction reaction of EC where the additional electron and lithium-ion forms $Li_2CO_{3(s)}$ and a significant amount of ethylene gas. From chapter 1, it was discussed that Li_2CO_3 could be a significant component of the SEI. However, reactions other those seen in Figure 2.3 could result in the formation of Li_2CO_3.

The one-electron reduction of EC (Figure 2.3) route (b) relies on the radical carbonate anion combining with an additional radical carbonate anion to form the dilithium alkoxide intermediate. This results in the formation of ethylene gas and LEDC. LEDC is a solid that is insoluble in electrolyte and has been widely reported to contribute to the SEI

by effectively passivating the negative electrode.[15] It should be noted that LEDC is suggested to be ionically and electronically insulating.[53]

Recent reports are disputing that LEDC is in the SEI and that LEMC is the primary component.[29] Wong, Xu, Eichhorn and colleagues argue that LEMC is the main reduction compound on the negative electrode surface. They concluded this by trying to synthesize the appropriate intermediates and were unable to do so for LEDC. They did find that LEDC and LEMC go through a facile reversible hydrolysis reaction.[54], which may explain the possible formation pathway to LEDC, and may explain how so many researchers claimed to find it in their electrolyte samples. The team argued that LEDC cannot exist in a cell environment as there will always be traces of protons. LEMC shows high Li^+ conductivity, and it is believed that the OH group in LEMC helps facilitate Li^+ motion through the SEI. Wang et al. have provided new mechanistic insights into EC reduction, however further study is needed to understand whether LEMC is produced via LEDC or through another nucleophilic attack of ethylene carbonate.

There is another proposed reduction mechanism of EC, where the intermediate has a radical on the central carbon atom. This intermediate would combine with an electron and a Li^+ ion to form carbon monoxide gas and lithium 1,2 ethanediolate $(CH_2OLi)_2$. However, gas analysis of cells post cycling showed ethylene gas to be the primary component, indicating the reduction reaction to favour the reaction shown in Figure 2.3.[55] In addition to the products described, it has been shown that EC can reduce to LiF in the presence of $LiPF_6$, lithium alkoxides, $LiOCO_2R$ and other polycarbonates on the negative electrode.[56–58]

As stated earlier, electrolytes are a combination of EC and other linear carbonates. Figure 2.4 routes (a) and (b) shows proposed linear carbonate reduction reactions. [59,60]

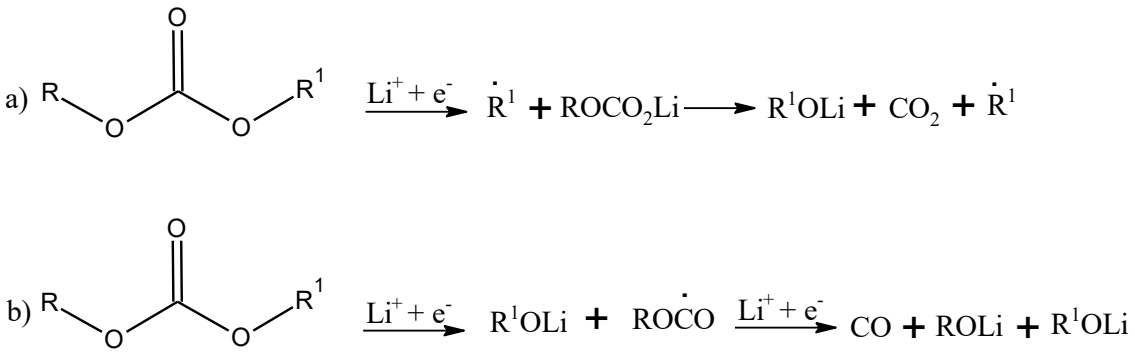

Figure 2.4 Proposed reduction mechanism of linear carbonates routes a and b.

Figure 2.3 route (a) shows a one-electron pathway where the linear carbonate combines with the lithium-ion and electron to form a Li-alkoxide (ROLi) and carbon dioxide. However, it has been shown that linear carbonates can also be reduced in a two-electron pathway.[59] The linear carbonate is shown in Figure 2.3 (route b) to reduce to form carbon monoxide and Li-alkoxides via a carbonate intermediate. Esters can also be formed from the radical carbon intermediate reacting with other radical hydrogens or alkyl groups.[19]

2.3 Transesterification reactions

Lithium alkoxides are primarily produced from the reduction of linear carbonates; however, they can also be produced from the nucleophilic reaction between lithium 1,2-ethanediolate and a linear carbonate. This reaction reforms EC and additional lithium alkoxides. Lithium alkoxides are nucleophiles that are able to react to both cyclic and linear carbonates; they are able to attack the carbon of the carbonate resulting in transesterification.[61,62] The reaction is an ester-exchange performed on the more positively

charged carbon atom of the carbonate and the stabilized intermediate with a delocalized charge from the oxygen atoms.

Reactions of lithium alkoxides and the bulk electrolyte results in substituted alkyl groups and alkyl-dicarbonates. If an electrolyte initially contained EC and EMC, the transesterification products are most likely to be DMC and diethyl carbonate (DEC). The transesterification of EMC to DMC and DEC is as follows. The reaction is acid catalyzed.[52,63,64]

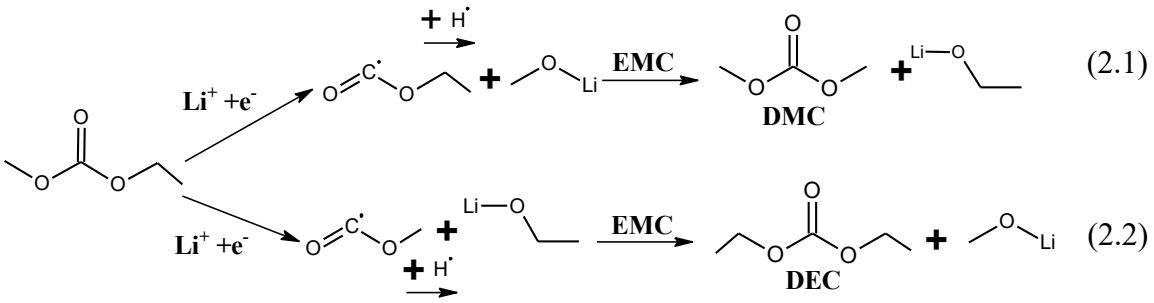

Li-alkoxides can also allow for the reaction between linear carbonates and EC to take place creating dimerization products:

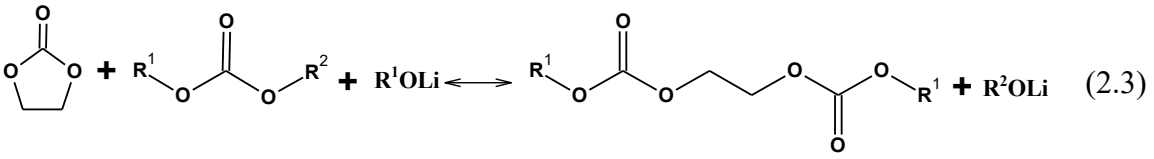

The dimerization products (reaction with EC) are expected to be dimethyl-2,5-dioxahexane carboxylate (DMOHC), diethyl-2,5-dioxahexane carboxylate (DEOHC) and ethylmethyl-2,5-dioxahexane carboxylate (EMOHC).[65] These dimerization products can be produced from any linear carbonate. The reduction of linear carbonates can follow many pathways and the by-products can further react. Therefore, the presence of esters,

aldehydes, methyl or methyl formate have all been reportedly found in electrolytes from cycled cells.[42]

Transesterification and subsequent reactions lead to products that are detrimental to cell lifetime. The production of DEOHC reflects the degree of transesterification and has been found to result in an increase in impedance of lithium-ion cells.[66,67] One theory suggests that these long-chain dicarbonates are more viscous than the bulk electrolyte and will result in a decrease in electrolyte conductivity.[68] The degree of transesterification and dimerization depends on the stability of the SEI, as well as the operating potential.[60] It is hypothesized that continual alkoxide formation on the anode surface may result in the anionic-alkoxide (meth or ethoxide) to diffuse (or migrate) to the cathode during cycling.[69] This would result in a build-up of electrolyte decomposition products on the positive electrode surface, resulting in an increase in resistance. Therefore, ineffective negative electrode passivation (formation of excessive alkoxide species) may result in resistance increases on the positive electrode. The cells in this thesis do not cycle to exceptionally high voltages and it is not expected that a significant transesterification will occur with the electrolyte systems used which passivate the negative electrodes well.[60,70]

Additives have also been shown to minimize lithium alkoxide formation and subsequent reactions.[20,52,56] The mechanism of how this happens is still not clear. One theory is that additives help form a stable SEI layer by reducing at a higher potential than electrolyte solvents preventing additional solvent from reducing.[52] Another theory is that additives could scavenge lithium alkoxides from solution.[56,71]

Qian, Hu, Zou and colleagues measured the amount of dimerization products using liquid chromatography-mass spectroscopy (LC-MS)[20] on cells that contained electrolytes

with the additives VC, $LiPO_2F_2$ (LPF), VC+LFP or blank. They found DEOHC to be present in the blank electrolyte (12.6% of the total amount) and in the VC only system (0.35% out of the total amount). VC thus inhibited the trans-esterification reaction between EC and DEC. Electrolytes that contained LPF or LPF+VC contained no DEOHC suggesting that LPF totally blocks transesterification between carbonate solvent molecules. It is assumed that Li-alkoxide formation is also impeded, but this was not explicitly stated in the article.

2.4 Decomposition of $LiPF_6$

$LiPF_6$ exhibits good stability but can decompose at elevated temperatures, especially over 60°C.[46,65] When this happens, $LiPF_6$ forms PF_5 and LiF, as shown in Equation 2.4.

$$LiPF_{6(sol)} \leftrightarrow LiF_{(s)} + PF_{5(sol)} \quad (2.4)$$

PF_5 is a strong Lewis acid, able to accept an electron pair, making it very reactive towards the electrolyte, electrodes and SEI. Water can also react with $LiPF_6$, even in trace amounts. [72] One reaction is shown in Equation 2.5.[64] PF_5 can further react with water to produce HF and POF_3, as shown in Equation 2.6.[64]

$$2H_2O_{(l)} + LiPF_{6(sol)} \rightarrow LiPO_2F_{2(sol)} + 4HF_{(sol)} \quad (2.4)$$

$$PF_{5(sol)} + H_2O_{(l)} \leftrightarrow POF_{3(sol)} + 2HF_{(sol)} \quad (2.6)$$

The products of the decomposition of salt have been shown to play a role in further reactions with the solvent.[73–76] PF_5 can catalyze the ring-opening of EC.[37,46,68] The resulting products can then further react with linear carbonates to form alkyl carbonates DMOHC,

DEOHC and EMOHC.[77] The reaction between water and salt can be suppressed if the solvent used has a high dielectric constant. This is due to the increased ionization of $LiPF_6$ in high dielectric solvents.[73]

Additives also have been shown to be useful in mitigating the damaging effects of salt decomposition. Han et al. showed that an additive (trimethylsilyl)isothiocyanate (TMNSNCS) acts as a Lewis base that can scavenge for HF and PF_5.[78] This additive did not help improve cycling performance but did allow for cells to operate longer at elevated temperatures. For specific applications, this may be useful.

2.5 Salt loss in solution

It is possible that the salt in electrolytes gets consumed over the course of charge and discharge cycling. Studies of electrolytes from cells cycled for a long time have shown a decrease in salt concentration.[79] To maintain the balance of charge in the electrolyte, for every Li^+ ion removed from the solution, an anion must also be removed or the generation of a proton or other cation must occur. It is not clear if transition metal cations dissolved in electrolyte from the positive electrode participate in maintaining electrolyte neutrality. One possibility is that the salt is removed to form Li-containing compounds LiF (insoluble) and $LiPO_2F_2$ (~1% soluble). [80]

2.6 Cross-talk in Li-ion cells

The term cross-talk in Li-ion cells refers to chemical or electrochemical side reactions on an electrode that produce soluble products.[81] These products can then physically cross the

separator and react chemically or electrochemically with the other electrode. When studying electrolytes, it is important to consider cross-talk reactions as a reason for the capacity fade sometimes seen in cells. However, cross-talk reactions can also be considered beneficial and sometimes benign to cell lifetime.[81] Any side reactions stemming from cross-talk can lead to loss of cyclable Li, impedance rises and loss of active material.[82,83] It is important to note that the cross-talk mechanism is highly dependent on the positive and negative electrode materials used.[84]

On the positive electrode, sources of cross-talk mainly come from transition metal dissolving into the electrolyte, formation of reactive oxygen species and CO_2/CO production.[83,85,86] For the negative electrode, gases produced can participate in cross-talk reactions along with long-chain oligomers discussed earlier in this chapter.[87]

A major source of CO_2 production in a cell comes from the oxidation of the organic electrolyte. CO_2 and to a lesser extent CO were found to be evolved at a potential as low as 4.2V vs Li/Li^+.[88] Full electrolyte oxidation is not observed until 4.8 V vs Li/Li^+.[89] The positive electrode material used can determine the extent of CO_2 evolution. Jung et al tracked CO_2 and CO evolution over a range of potentials for variety of positive electrode materials.[90] After normalizing for surface area, they found NMC materials had lower onset potentials for CO_2 and CO evolution compared to LNMO (lithium nickel manganese oxide) materials. Metzger et al used isotopic labeling of EC and EMC to find that most CO_2/CO evolution comes from electrolyte oxidation while the rest comes from electrode oxidation.[91]

It is suggested that CO_2 can be beneficial to cell lifetime and has been used as an additive.[92] Most likely it improves the passivation of the negative electrode SEI, although

the mechanism is not clear. Lucht et al created an SEI in a cell that was absent of any CO_2.[93] It was found that little to no Li_2CO_3 was formed. Schwenke et al studied CO_2 at low potentials and found the compound to reduce to form carbonates and oxalates.[94] These products have low solubilities and therefore can help contribute in creating a passivating layer on the negative electrode surface.

Lastly, on the positive electrode, reactive oxygen species can be produced that can influence the negative electrode performance. Oxygen from oxide active materials can be electrochemically reacted at high potentials. This can be in the form of a singlet oxygen, superoxide anion (O_2^-) and other reactive oxygen species.[81] However, it is expected that these oxygen species will react with the electrolyte before reaching the negative electrode and those products are expected to be capable of cross-talk, Gueguen et al, showed POF_3, a compound which is formed from a reactive oxygen species, was consumed on a graphite electrode but not on a delithiated LFP (lithium iron phosphate) electrode.[95]

Now, the negative electrode will be discussed. Specifically, how the degradation products discussed thus far in this thesis can cross over to the positive electrode and alter the cathode-electrolyte interface. Work by Sahore, Dogan and Bloom investigated the origin of electrolyte decomposition species.[96] To do that, they built a two-compartment pouch cell using a solid-state lithium-ion conducting separator that allowed only Li^+ ions to move through during cycling. The negative electrode and the positive electrode compartments could then be analyzed separately. The analysis of the aged electrolyte was done using high-performance-liquid chromatography coupled to an MS as well as NMR spectroscopy. They used a graphite negative electrode and an NMC-type positive electrode with 1.2M $LiPF_6$ in EC:EMC 3:7 by weight electrolyte with no beneficial additives. The

results are compared to electrolyte from a cell that had a typical microporous polypropylene-based separator.

Figure 2.5 shows the proposed products generated when cross-talk is allowed to happen (polypropylene separator cell). These compounds are unique as they were not seen in either compartment of the two-compartment cell. They proposed these structures based on the molecular weight, calculated number of carbons and several assumptions. Many of these species contain unsaturated carbon bonds and C-F bonds and had not been reported in the literature for Li-ion battery electrolytes. Removal of hydrogen bonds and the addition of F atoms could be an indication of oxidation reactions. They also found that some of these species contained phosphorus and likely originated from the reaction of PF_5 with EC, EMC, and the transesterification products described earlier. They also described that species were generated at the negative electrode then oxidized at the positive electrode to create the complex structures.

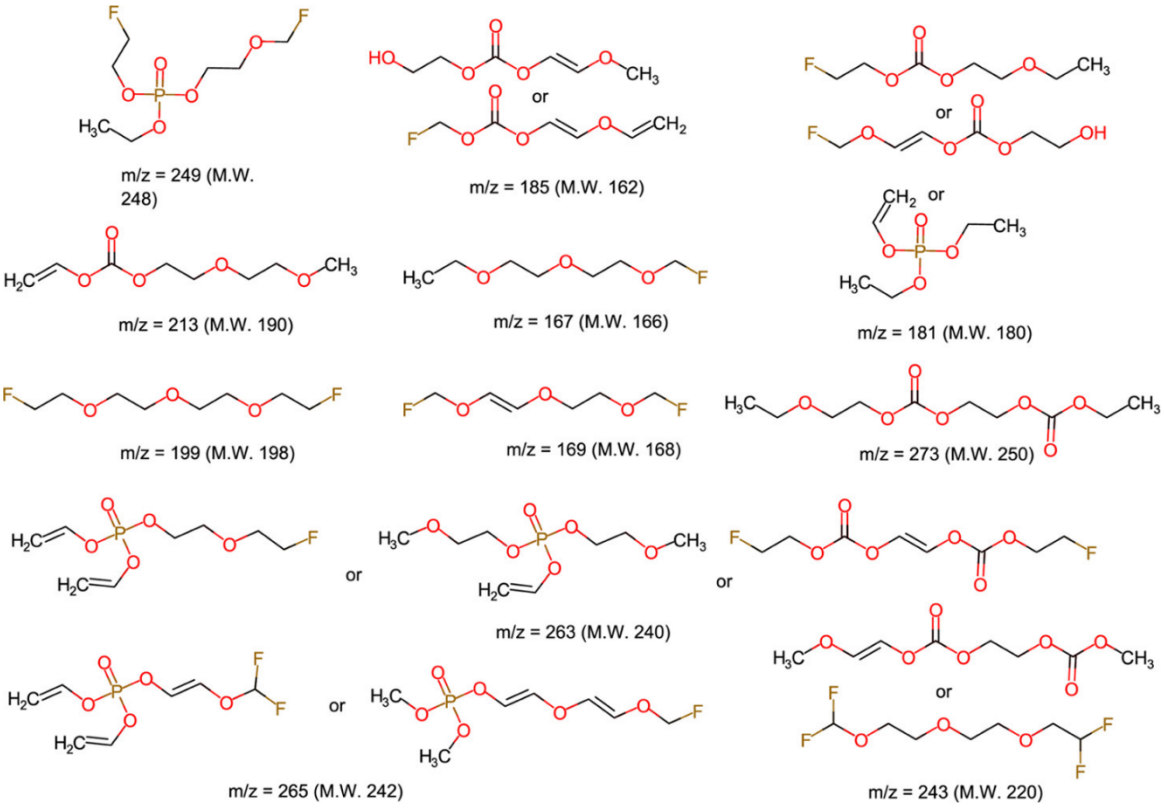

Figure 2.5 Proposed chemical structures for molecules corresponding to detected m/z peaks for species only present in an electrolyte where cross-talk reactions occurred.[96] Reprinted with permission from Chem. Mater. 2019 31 (8) 2884–91. Copyright 2019 American Chemical Society

The work by Sahore et al. was not quantitative, but in Figure 2.5, compounds at the top of the figure had higher measured intensities in the HP-LC chromatograms. It is important to note that no additives were used in that study. The compounds suggested may or may not be detrimental to cell lifetimes. Further work will be needed to make these conclusions. However, it is exciting that a method is available to study the products of electrolyte decomposition. Applying this method to study cells with additives in their electrolytes will also be very interesting.

2.7 Transition metal dissolution

During cycling, it is possible that metal from the positive electrode can dissolve into the electrolyte then travel to the negative electrode to deposit on the surface.[55,66] These metals can possibly alter the formation and growth of the SEI. It is still not clear what the mechanism of failure is for a metal contaminated SEI. Metals have been detected on the negative electrode surface for a variety of cathode materials, electrolytes and cycling conditions. [30,85,98,99] The mechanism of how metals end up on the negative electrode surface is still debated along with why or if the deposited metals are detrimental to battery life.[100,101]

Many different transition metal oxides materials, including NMC materials, have been shown to undergo transition metal dissolution. The reaction is exacerbated at higher temperatures for cycled cells.[101] In addition, higher upper-cut off voltages also have shown to promote metal dissolution.[60,80] The decomposition of $LiPF_6$ by heat or water possibly results in HF formation, which could then, in turn, promote transition metal dissolution.[80,102] In addition, long-chain electrolyte decomposition products may help promote metal dissolution by acting as chelating agents to the metal ion.[42]

For NMC materials, Mn has been reported to have the most severe dissolution.[42] Reports also suggest that when the positive electrode converted from a layered to a spinel structure, Mn dissolution was more pronounced.[103,104] The consensus is that dissolved Mn is in the Mn^{3+} or Mn^{2+} state.[105] Figure 2.6 shows two possible mechanisms for migration of Mn^{2+} ions.[106] Figure 2.6 (a) shows a simple mechanism where the charged Mn^{2+} ions get solvated and travel to the negative electrode surface.

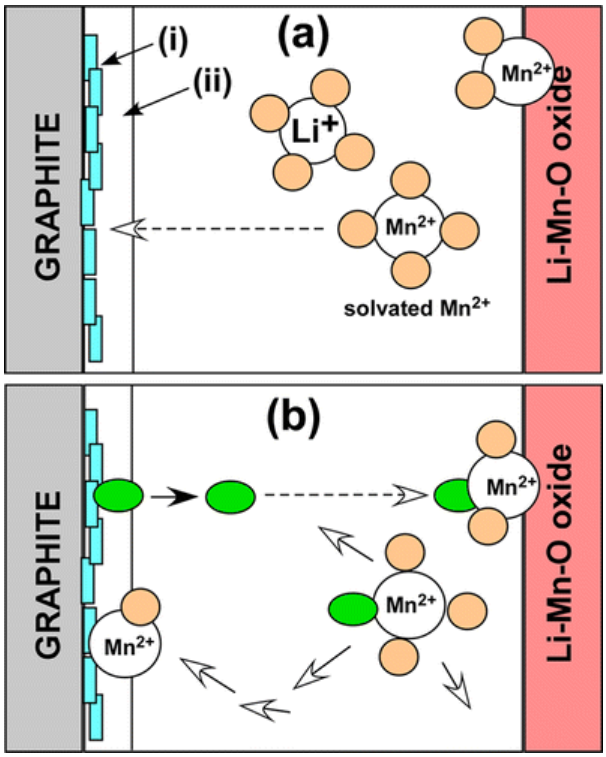

Figure 2.6 Two models of transport and deposition of Mn^{2+} ions in Li-ion batteries. (a) Mn^{2+} ions are solvated by carbonate molecules in the same fashion as Li^{+} ions, and drift along the field lines penetrating through the outer (organic) SEI (ii) and become deposited into the inner (mineral) SEI layer at the graphite particle surface (i). (b) Electrolyte decomposition products with chelating groups reach the cathode and form neutral complexes of Mn(II) that diffusively migrate to the graphite surface, bypassing the outer SEI, and these complexes become chemisorbed on the surface of lithium carbonate crystallites in the inner SEI layer that serves as an ion exchanger.[106] Reprinted with permission from J. Phys. Chem. C 2014 118 (42) 24 335–48. Copyright 2014 American Chemical Society

Many groups report a range of 50-200 ppm of dissolved metals (not just Mn).[107] Compared to the concentration of conductive salt ~1M or greater expected in the electrolyte, transition metals are extremely diluted. Transition metal ion transport is to be governed by diffusion.

Figure 2.6 (b) shows the metal ions coordinating to the decomposition products of the electrolyte like LEDC. The complex then gets chemisorbed onto the inner SEI layer.

Again, more recent reports refute that LEDC or other decomposition products will solvate the metal ion.[108,109] Wang demonstrated that Mn^{2+} is preferentially solvated over Li^{+} by the PF^{-}_{6} anion and EC.[109] However, Wang also describes that this solvation sheath is unstable even before it reaches the SEI. This instability is what results in electrolyte reduction on the negative electrode with the deposited metals.

Figure 2.6 (b) is also partially refuted as it was found by Tornheim et al. that Mn can also be observed at the surface of the SEI when highly fluorinated electrolytes are used.[108] It was found that highly fluorinated electrolytes could lower the HOMO and LUMO of the solvent leading to an increase in anodic stability.[110] The lower LUMO levels also thermodynamically favor cathodic reactions on the surface of the negative electrode. In conventional electrolytes, Mn ions are found in the bulk of the SEI.[108] The electrolyte environment around the solvated metal is what governs the deposition at the negative electrode, and the SEI composition determines where the metal will be found.[81]

Ideas to prevent transition metal ions from depositing on the negative electrode surface, revolve around creating a strong SEI. Therefore, using additives that can limit the production of problematic decomposition products may hinder or prevent metal dissolution. It was also suggested that coatings can help stabilize the positive electrode surface, neutralizing the mechanisms of metal dissolution.[81] However, there is no known way to prevent this phenomenon entirely. The key to understanding transition metal dissolution will be to study the positive electrode-electrolyte interface further.

2.8 Summary

The content discussed in Chapters 1 and 2 was included to provide background information for the work presented in Chapters 4. Key considerations include the role additives play for the electrode surface, electrolyte decomposition products and the transition metal dissolution of the positive electrode.

CHAPTER 3 – EXPERIMENTAL METHODS

Li-ion cells used in this work are wound pouch cells that were produced without electrolyte by a large manufacturer. The cells are machine-made and hence very uniform. Therefore, the effect of electrolyte and additives on cell performance can be confidently ascribed to those variables and not to cell-to-cell variation.

3.1 Cell specifications

Cells studied in Chapter 4 consisted of dry $Li(Ni_{0.5}Mn_{0.3}Co_{0.2})O_2$ (NMC532)/graphite pouch cells (215 mAh at 4.3V) which arrived sealed from Li-FUN Technology (Xinma Industry Zone, Golden Dragon Road, Tianyuan District, Zhuzhou City, Hunan Province, China, 412000). The positive electrodes used single-crystal NMC532 (94% by weight), 4% conducting diluents and 2% polyvinylidene fluoride (PVDF) binder. The NMC532 particles were coated with a Ti-based coating as described by Ma et al.[111] The negative electrode consisted of 95.4% artificial graphite (15–30 μm particle size), 2% carbon black and 2.6% sodium carboxymethylcellulose (NaCMC)/styrene butadiene rubber (SBR) binder. The positive and negative electrode single side loadings were 21.1 mg/cm^2 and 11.5 mg/cm^2, respectively. Before filling with the designed electrolytes, pouch cells were cut open and dried at 100 °C under vacuum for 14 h to remove residual moisture.

3.2 Cell filling

Pouch cells were filled with 0.85 mL (~1.0 g) electrolyte in an Ar-filled glove box and sealed with a pouch sealer (MSK-115A Vacuum Sealing Machine, MTI Instruments) at 170°C under vacuum at -90 kPa of pressure. Figure 3.1 (a-b) shows the process of filling a cell.

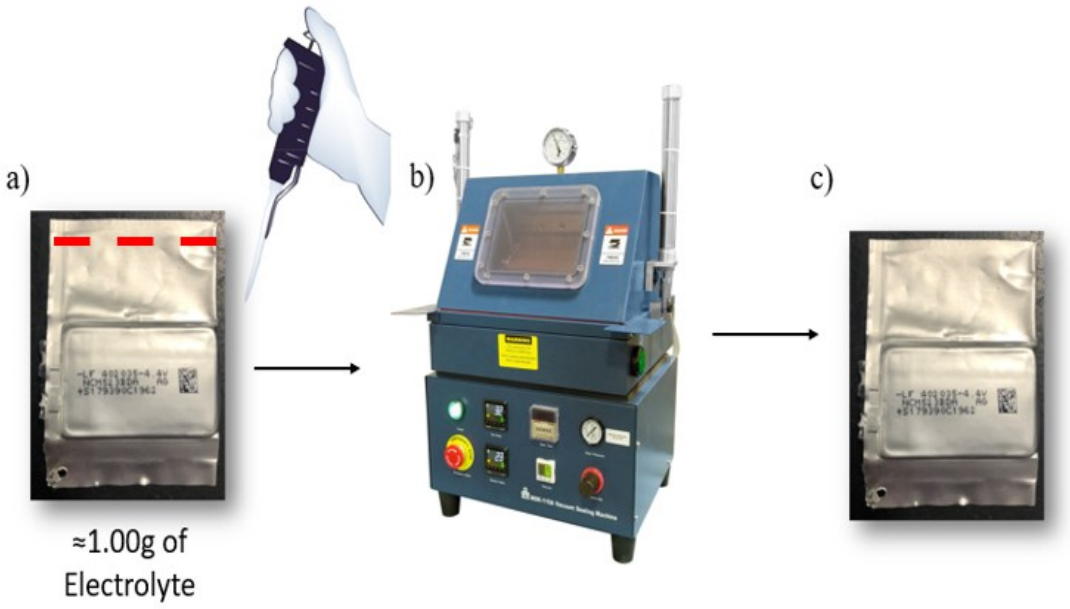

Figure 3.1- Shows the process of filing cells. a) cells filled with 0.85 ml of electrolyte. b) vacuumed sealed and c) cell ready to start the formation cycle.

3.3 Electrolytes

All electrolytes were prepared to contain 1.33 m $LiPF_6$ (Shenzhen Capchem, China ≥ 99.9%) in EC:EMC:DMC 25:5:70 (by volume) (Shenzhen Capchem, ≥99.5%, water content 19.7 ppm). The two additives used in this study were VC and DTD (Shenzhen Capchem ≥99.8% and Suzhou Yacoo Chemical Reagent Co ≥ 98%, respectively). In total, eight electrolytes were prepared by varying the combinations of VC and DTD by weight. Table 3.1 shows the combinations created.

Table 3.1 Additive combinations used in cells discussed in Chapter 4.

Weight % VC	Weight %DTD
1	*0*
1	*1*
1	*2*
1	*3*
2	*0*
2	*1*
2	*2*
2	*3*

3.4 Cell formation

After filling, sealed cells were held at 1.5 V for 24 hours at room temperature to ensure the full wetting of the electrodes. The cells were then transferred to a 40°C temperature-controlled box to undergo formation. Cells were charged using a Maccor 4000 series charger to their upper cut-off voltage at C/20 (10.75 mA) then discharged at the same rate to 3.8 V. The cells were transferred back to an Ar-filled glovebox, degassed (to remove SEI formation products) and vacuum-sealed again in the same manner previously described.

The formation cycle is important for SEI formation. Figure 3.2 shows a part of the differential capacity (dQ/dV) vs. voltage (V) curve for two cells with different electrolytes. Where Q is the capacity in units of ampere hour. It is the number of hours for which a cell delivers a current equal to the discharge rate at the nominal voltage of the battery. The dQ/dV curve will have peaks that correspond to the reduction of specific species.[52] The reduced species will form the passivating film on the negative electrode if they are not

liquid or gases thus hindering further electrolyte reduction during subsequent cycles. Burns et al. found that EC will start reducing at ~2.9V (~0.4 V vs. Li/Li^+) during the first cycle.[112] Figure 3.2 compares the dQ/dV curves during formation for cells with no additives present (black) to an electrolyte with VC and DTD present (red). Figure 3.2 shows the expected EC reduction region. The additives suppress EC reduction by being preferentially reduced and thereby successfully passivating the electrode.

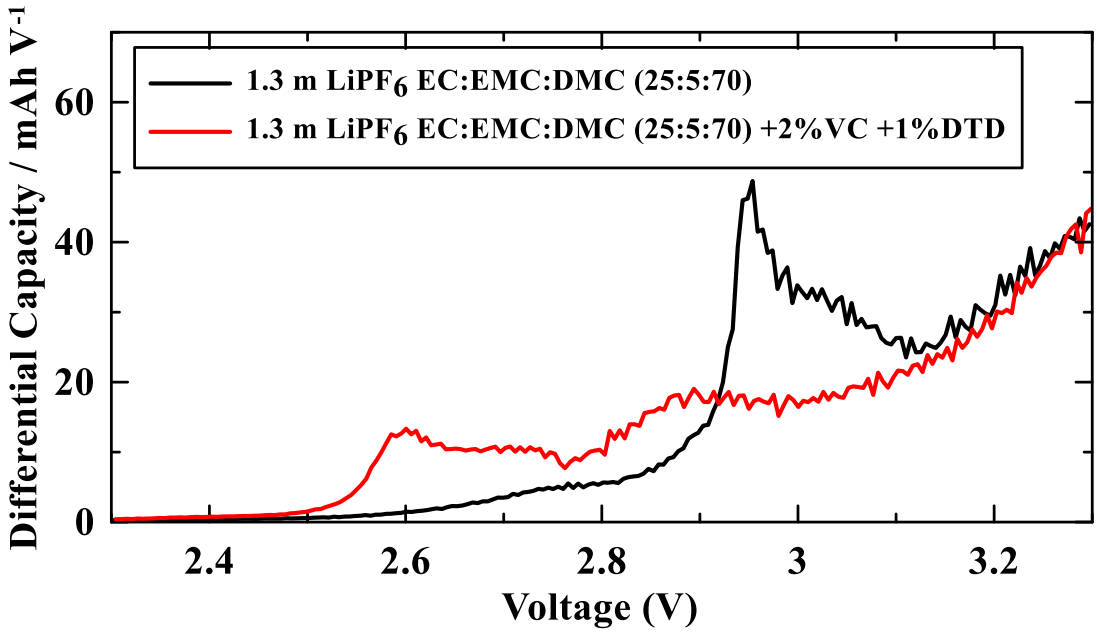

Figure 3.2 – Differential capacity (mAh V^{-1}) vs voltage (V) profile for two cells. Cell with no additives (black) shows EC reduction around 2.9 V. Cell with additives 2%VC +1%DTD (red) starts reducing around 2.6 V.

3.5 Cell Cycling

When studying cell performance, it is important that the cycling equipment used can provide the necessary data for interpretation. These systems can record the voltage, current,

charge capacity, discharge capacity and time for a cell as it cycles. Prepared cells were tested for long-term cycling following the same protocol described in Ma et al.[113] Cells were charged and discharged at 1C rate between 3.0 and 4.3V. After 100 cycles of 1C/1C, each cell was cycled at C/20 for 1.5 cycles then an additional sequence of increasing discharge rates of C/2, 1C, 2C and 3C with the charging rate maintained at 1C was preferred. The tests were made at (20.0 ± 0.5)°C in a climate-controlled room or (40.0 ± 0.1)°C in a temperature-controlled box. Neware (Shenzhen, China) chargers were used for these tests.

The charge (Q_c) and discharge (Q_d) capacities were recorded vs. the charge-discharge cycle number. During the charge and discharge cycles, the cell potential is also recorded. The difference between the average charge and discharge potential is ΔV. Increases in ΔV can be due to impedance growth in the cell.[114] This property of a cell can be used to estimate SEI resistance growth during cycling.

3.6 Gas measurements

The amount of gas produced in the cells during formation and cycling was measured using the Archimedes' principle. The cells were at 3.8 V for the volume measurements. The procedure used is described in Aiken et al.[115] Cells are hung below an analytical balance (Shimadzu, AUW00D) and submerged in room temperature de-ionized water (18.2 MΩ-cm, Thermo Scientific Barnstead Nanopure Water Purification System) and weighed. Figure 3.3 shows photographs of the apparatus (a) and an example of a cell submerged in water (b). Due to the cells being sealed the mass of the cell remains constant. The difference between the weight of a cell before and after testing is proportional to the volume of gas produced.

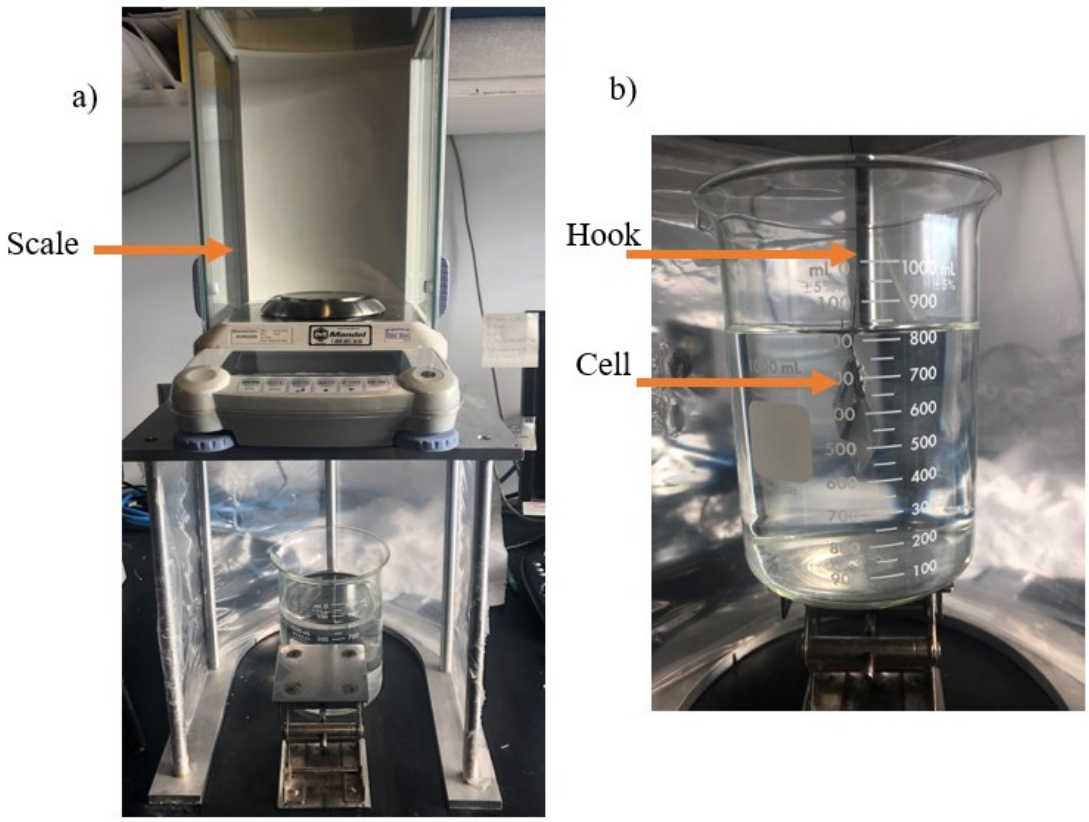

Figure 3.3 shows the gas measurement apparatus (a) and an example of a cell being submerged in water while being weighed (b).

3.7 Electrochemical impedance spectroscopy (EIS)

EIS is a technique that gives impedance information on an electrochemical system (in-situ). EIS measures cell impedance for a range of frequencies. Typically, a sinusoidal voltage signal is applied to the system at a specific frequency, then the resulting current at that frequency is measured. The process repeats for the desired frequency range.[116] The voltage must be small enough to get a linear current response from the cell. Figure 3.4 (a) shows a simple circuit model of a full cell. This work measures full-cell impedance and reports the charge-transfer resistance (R_{ct}) extracted from the Nyquist plots produced from the raw EIS data (Figure 3.4 (b)). Nyquist plots are commonly used to plot EIS data, where

the real part of the impedance is plotted on the x-axis and the negative imaginary part of the impedance (from the capacitor) is plotted on the y-axis. R_{ct} is found from the Nyquist plots as the total dimeter from the "semi-circle" portion of the spectrum.

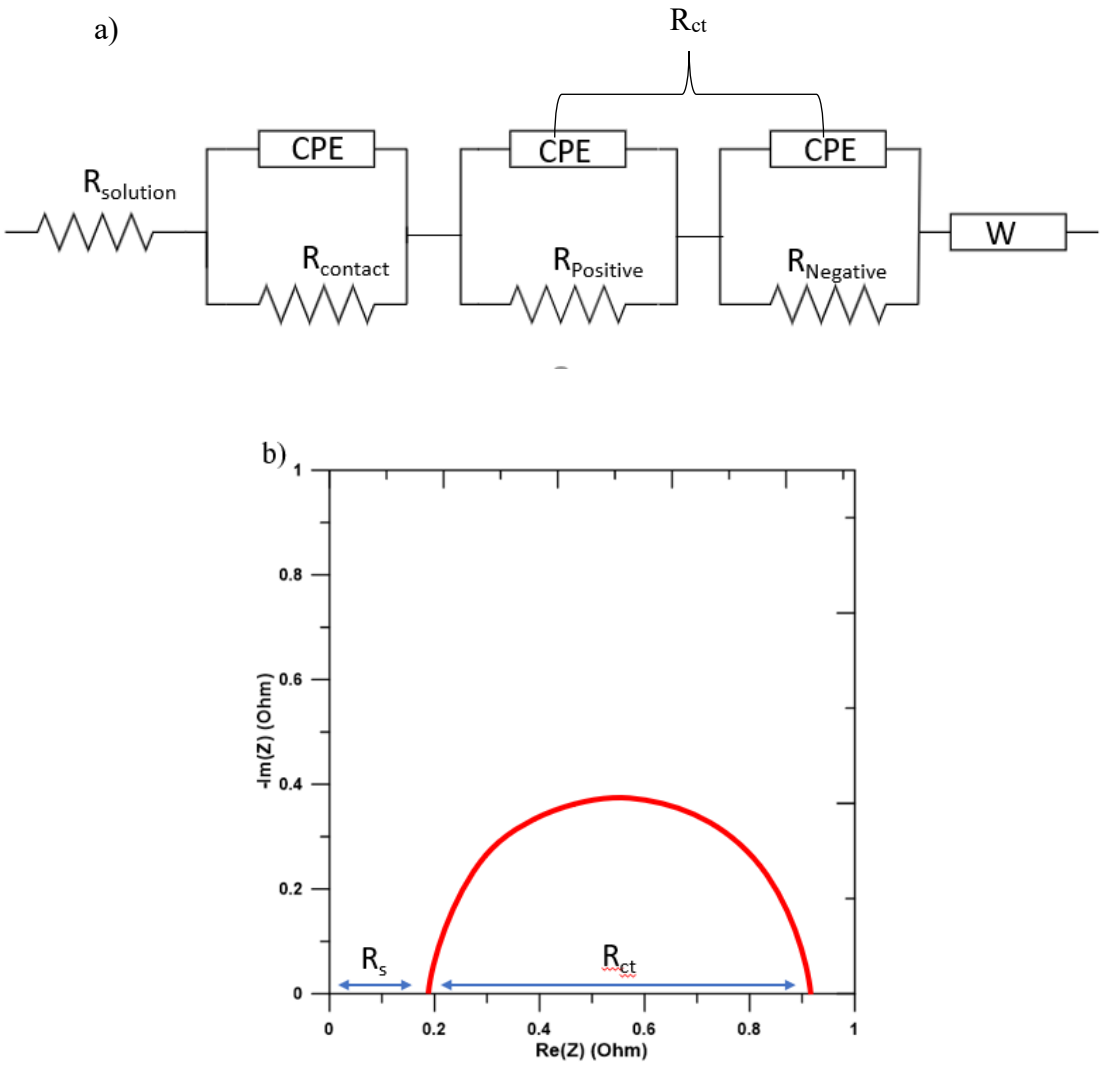

Figure 3.4 a) Circuit model of a full lithium-ion cell, b) an example of a Nyquist plot that is absent of contact impedance and diffusion (W) contributions.

Figure 3.4 (a) shows a circuit model used to describe sources of impedance a cell. The solution resistance (R_s) is modelled as a resistor to manifest as a single point on the real axis of a Nyquist plot. The solution resistance is the resistance of the lithium-ion moving through the electrolyte. The contact impedance ($R_{contact}$) represents the impedance from the electrode material current collector interface. This is modelled as a CPE (constant phase element), which can be considered as an imperfect capacitor, in parallel with a resistor. Faradaic reactions are modelled with two circuit components, where CPE models charging of the double layer, and R is the resistance to charge transfer. W is the Warburg impedance used to represent diffusion effects. $R_{contact}$ and W are not considered in this work. Here, R_{ct} is a combination charge transfer resistance of the of negative and positive electrodes of a lithium-ion cell. It includes the resistance of the lithium-ion moving through the SEI and resistance due to the desolvation of lithium ions at the negative electrode surface.

A Biologic VMP3 (Seyssient-Pariset, France) electrochemical test station performed the EIS tests. The measurements done on the cell were at (10.0 ± 0.1)°C in a controlled temperature box (Novonix, Bedford, N.S., Canada).[117] Data were collected with ten points per decade from 100 kHz to 10 MHz with a signal amplitude of 10 mV. The charge transfer resistance (R_{ct}) from the full cell is reported.

3.8 Electrolyte extraction method

Often, when trying to extract electrolyte from a heavily cycled pouch cell, the amount of electrolyte which can be extracted, compared to that initially added, is severely diminished.

The cell appears practically dry upon opening. However, long-lived cells are some of the most valuable and analyzing their electrolytes is important in understanding the reason behind their longevity. A method was developed to ensure that the analysis would not be limited by extraction volume. After cycling, cells were discharged to 2.5 V and moved into an Ar-filled glovebox.[60] Figure 3.5 shows a visual representation of all the steps to extract electrolyte from a cell. A small opening was made in the pouch cell using scissors where 0.6 mL of acetonitrile (Sigma, HPLC grade) was added using a syringe (Figure 3.5 (b)). The solvent was then massaged into the pouch cell to promote mixing. To prevent evaporation of the solvent-electrolyte mixture, the opening made in the cells was sealed with atactic polypropylene using a Mastercraft (Canadian Tire, Canada) dual-temperature glue gun (Figure 3.5 (c)). Cells were weighed after sealing, then stored upright in the Ar-filled glove box for 24 hours to allow for thorough mixing of the electrolyte and solvent throughout the jellyroll. Before unsealing, cells were weighed again to verify that no mass loss occurred. Once reopened, a 1 mL syringe was used to remove as much of the extract as possible, normally between 0.5 and 0.8 mL.

The extracted electrolyte mixture was added to a 10.00 mL glass volumetric flask containing (Figure 3.5 (d)) 1.00 mL of acetonitrile, 0.50 mL of deuterated acetonitrile (Sigma), and 0.20 mL of 1,4 bis(trifluoromethyl)benzene (Sigma, internal standard) before final dilution to 10.00 mL with acetonitrile. 0.70 mL of the mixed solution was transferred to a Wilmad glass NMR tube (Wilmad 506-PP-8) and capped with a gas-tight Wilmad NMR cap (WG-3891-100). Figure 3.6 shows an image of samples sealed with the gas-tight cap.

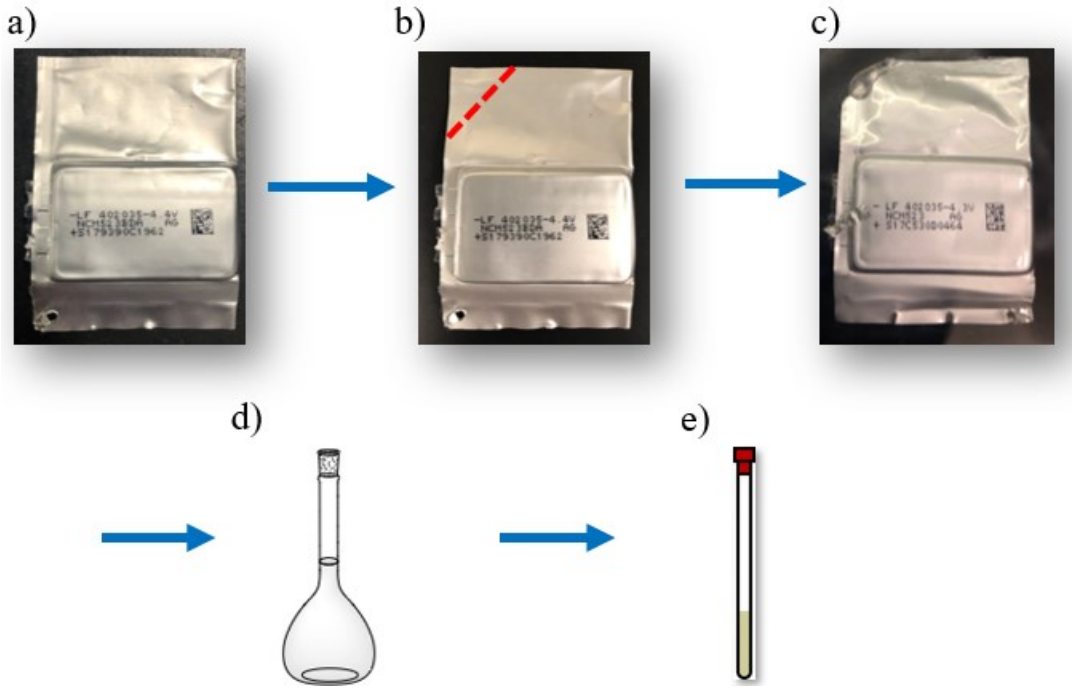

Figure 3.5 a) Cell before extraction; b) where cell would be initially cut open. c) Cell sealed with polypropylene after the addition of acetonitrile. d) extraction moved to a volumetric flask for sample preparation for NMR measurement (e).

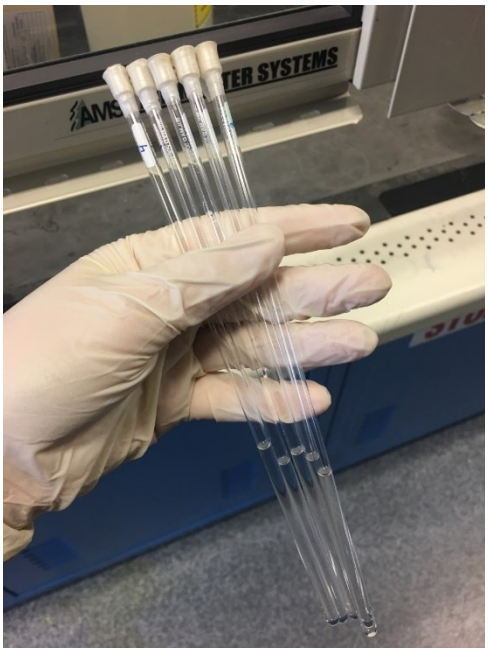

Figure 3.6 Photograph of NMR samples with gas-tight caps.

To confirm that acetonitrile was not reacting with the electrolyte or electrodes, a simple NMR (nuclear magnetic resonance spectroscopy) experiment was performed. An NMR technique reported by Schwenke et al. was used to see if acetonitrile would dissolve any SEI (solid electrolyte interphase) components.[94] In this case, tests were performed using a single pouch cell that was completely discharged after cycling and dismantled. The negative electrode pieces (from the same cell) were all washed with DMC 3 times, then left to dry in a fumehood. After drying, they were immersed in 0.5mL acetonitrile or water for 30 minutes. Samples washed with water had a few drops of D_2O added, and samples washed with acetonitrile had a few drops of d-acetonitrile added for shimming. Figure 3.7 shows the results of the ^1H NMR experiment and show that acetonitrile does not dissolve any SEI components. It should be noted that acetonitrile has high chemical and oxidative stability.[118]

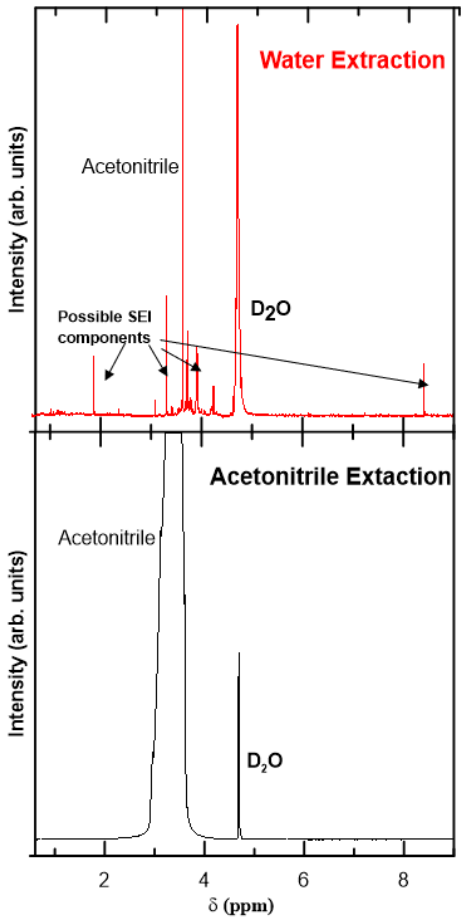

Figure 3.7 The results of the NMR experiment where acetonitrile was verified not to dissolve SEI components. The acetonitrile spectrum (lower half) has a broad peak, most likely due to poor shimming. However, the acetonitrile is not dissolving components of the negative electrode SEI.

The cell electrolyte extraction method was also verified using ^{1}H NMR and ^{7}Li NMR by comparing extracted electrolyte from a cell held at 1.5 V for 24 hours to that of a fresh sample. Table 3.2 shows small differences between the measured original electrolyte and the sample obtained from the wetted cell, for Li, EC, EMC and DMC concentrations. No other products were observed in the extracted electrolyte sample.

Table 3.2 Comparing the results from ^{1}H and ^{7}Li NMR between fresh electrolyte (1.4 m $LiPF_6$ in EC:EMC:DMC (20:47:33 wt%) electrolyte) and the same composition extracted from a wetted cell.

	Li conc / m	***σ***	***EC Conc / % total solvent***	***σ***	***EMC Conc / % total solvent***	***σ***	***DMC Conc / % total solvent***	***σ***
Fresh Electrolyte n=3	1.36	0.07	20.7	0.20	47.4	0.30	32.0	0.50
Extracted Electrolyte n=2	1.368	0.003	17.8	0.30	44.90	0.14	37.4	0.50

3.9 Gas chromatography (GC) -Mass Spectroscopy (MS)

A GC is an instrument used to separate multiple analytes of interest in a sample. Figure 3.8 shows a schematic of a gas chromatograph and mass spectrometer. The GC sample is first injected through a septum into the inlet. The sample moves into the column by the carrier gas (mobile phase), which is continuously flushed through the system. The components separate based on the different interactions of the analyte with the stationary phase (the column).[119] The separated components then elute out of the column with different retention times (t_R). The carrier gas used and the column will determine the extent of mixture separation. Retention time can be estimated by summing the projected travel time of a specific analyte through a column and the delay time of the analyte due to its interactions with the stationary phase.

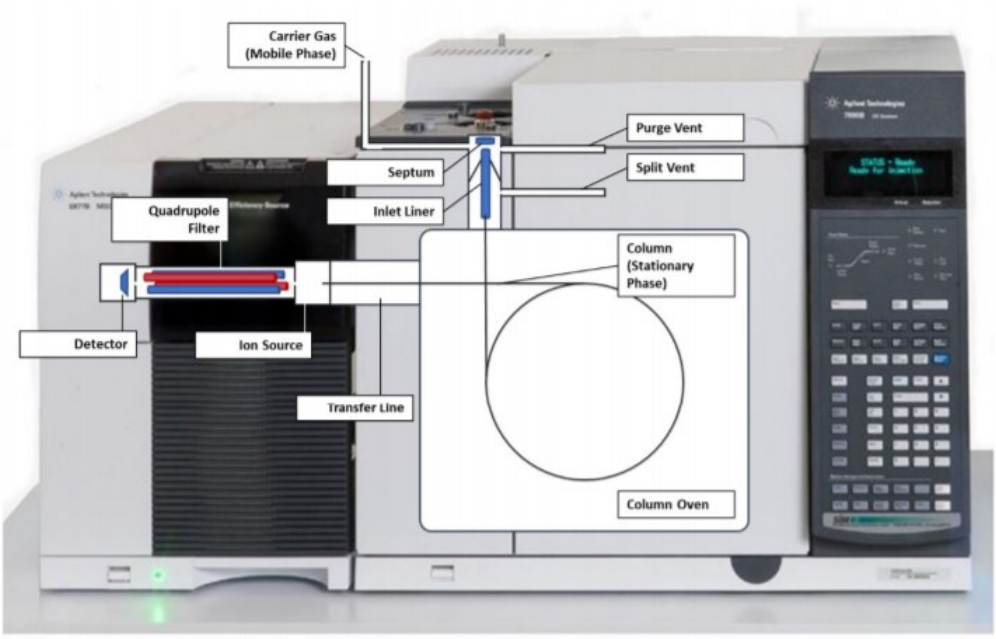

Figure 3.8 Schematic of a GC-MS. Taken with permission from Lauren Thompson, *Changes to the electrolyte in aged Li-ion cells,* M.SC. thesis, Dalhousie University, Halifax, NS (2018).[120]

The temperature profile used in a GC system can improve the separation of compounds in a mixture by emphasizing the separation of compounds with a lower boiling point from a compound with a higher boiling point. This technique does not help separate compounds with similar boiling points, only a specifically designed column can force the separation.[121] The separated components can only be identified and quantified by using a detector. This thesis uses a mass spectrometer as a detector.

Mass spectroscopy

Figure 3.8 shows a schematic of a mass spectrometer in addition to the GC system. Once compounds elute from the GC column, they enter the transfer line to get ionized in the

electron ionization chamber.[122] In the chamber, electrons bombard the sample causing a radical cation to be generated. Equation 3.1 shows the radical cation to be ionized with a 1+ charge. The ionization process can also fragment molecules further, as shown in Equation 3.2 where AB gets fragmented into a cation and a neutral radical.

$$M + e^- \rightarrow M^{\cdot +} + 2e^- \quad (3.1)$$

$$AB + e^- \rightarrow A^+ + B^{\cdot} + 2e^- \quad (3.2)$$

In the next step, all fragmented ions get accelerated into a finely focused beam so that they all have the same kinetic energy. The fragments then get sorted in a quadrupole mass analyzer. Figure 3.7 shows the analyzer to have four rods, two have a positive potential (red), and two have a negative potential (blue). A voltage is applied to the rods, and it is applied either as an alternating current or direct current with variable frequency. Any charged species that pass through will interact with the electric field. The manner of in an ion interacts with the rods depends on the charge of the ion, the mass of the ion and the potential, which is applied to the rods. Potentials are set for a specific mass-to-charge ratio. Any ion that is not that specific ratio will collide into the rods and are filtered out. The system then scans various mass-to-charge ratios by changing the voltage applied to the rods. By increasing the potential, higher mass-to-charge ratios can reach the detector.

The final destination for the filtered ions is the electron multiplier detector. Ions collide within the walls of the detector to eject electrons. The ejected electrons produce a current that is converted into a voltage reading for quantification.

3.11 Gas Chromatography-Mass spectrometry sample preparation

After NMR sample preparation, the remaining extracted electrolyte was removed from the Ar-filled glovebox for GC-MS analysis. Potentially damaging lithium salt and HF were removed from the GC-MS sample using a salt assisted liquid-liquid extraction (SALLE) method.[123] Due to water and acetonitrile being miscible, the addition of inorganic salt in the aqueous layer increases the polarity difference between the aqueous layer and organic layer, effectively removing the $LiPF_6$ salt. Figure 3.9 shows the steps to prepare the electrolyte for sample preparation. First, a 3.0 mL aliquot of 10.0 mL electrolyte sample mixture was transferred to a 15 mL polypropylene vial (a) with the addition of 0.4 mL of highly concentrated aqueous ammonium sulfate solution (~3 M) (b), capped and mixed for 30 seconds. The salt was added to ensure that no lithium was left in the organic layer. The tube was then centrifuged at 920 g at 12°C for 20 minutes to promote the separation of the organic and aqueous layers. Three drops of the organic top layer were further diluted with ~1.5 mL of acetonitrile in a small, 1.5 mL GC vial.

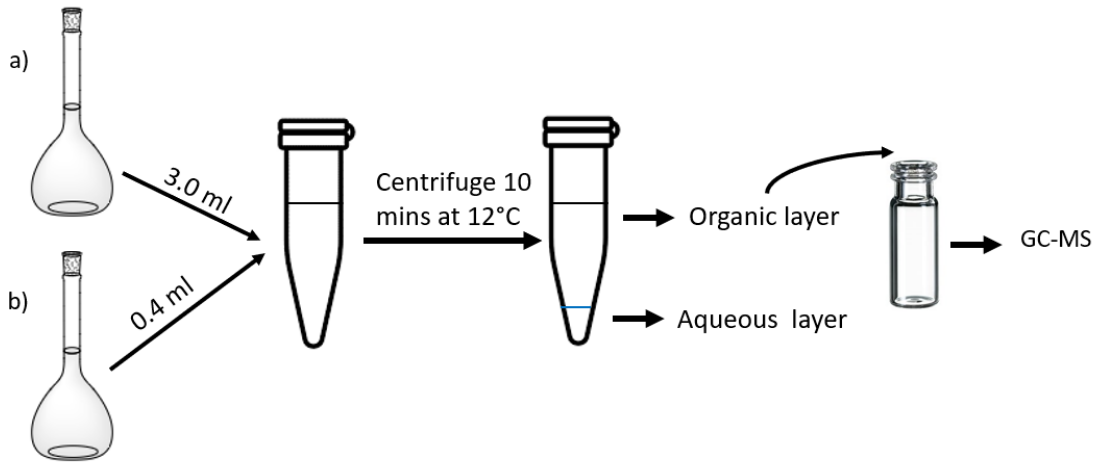

Figure 3.9- Steps to complete sample preparation for GC-MS analysis using a) 3 ml of extracted electrolyte and b) 0.4 ml ammonium salt solution.

Standard solutions were created to quantify and determine the detection limits of degraded electrolyte components. A calibration solution with known amounts of EC, DMC, DEC, EMC, VC, DEOHC (diethyl-2,5-dioxahexane carboxylate) and DMOHC (dimethyl-2,5-dioxahexane carboxylate) was added to a known amount of acetonitrile.

An Agilent 7890 gas chromatograph (Bruker BR-5MS, 30 m column) coupled to an Agilent 5977b single-quadrupole mass spectrometer was used for organic analysis. The carrier gas was helium (99.999%) at a constant flow of 0.68 mL/min. 1.5 uL of the sample was injected into the inlet (260°C, split ratio 100:1) then carried onto the column at 35°C for 5 minutes before ramping column temperature to 100°C at 15 °C/min, then to 240°C at 30°C/min where the oven was held for the duration of the 20-minute run. Samples were ionized via electron impact in the mass spectrometer.

Calibration standards were measured for each sample set. Each sample and standard were injected twice for reproducibility. Peaks were identified based on retention time and expected mass/charge ratios and quantified based on the integration of appropriate

mass/charge ratio signals. Detection limits for each compound were determined based on standard deviations of the blank sample, and uncertainty in quantifying the samples was estimated by the deviation of the calibration curve ($R^2 > 0.98$) from linearity.

3.12 Nuclear magnetic spectroscopy (NMR)

A significant portion of the work in this thesis uses NMR for the analysis of electrolytes. NMR is a spectroscopic technique that relies on the magnetic dipoles generated from certain atomic nuclei. Examples include hydrogen (^{1}H), carbon(^{13}C), fluorine(^{19}F) and lithium(^{7}Li).[124] The commonality between these nuclei is that they have an odd number of protons or neutrons (or both), resulting in a net magnetic moment. These nuclei have an intrinsic spin that is described by their nuclear spin quantum number *I*. *I*=0 denotes no spin followed by values of ½, 1, 3/2, etc. *I* determines the number of quantum mechanical states in an external uniform magnetic field with the formula $2I+1$. For the proton, it has *I*=1/2; therefore this nucleus has 2 possible states.

Magnetic moment is quantized as spin up (m=+1/2) and spin down (m= -1/2). Figure 3.10 shows an example of an NMR system with all the components labelled. A sample is inserted into the bore where it is held above a superconducting magnetic producing a large magnetic field B_o. The magnetic field will force the magnetic moments of the nuclei to either align in the direction of the field (spin up-preferred) or in the opposite direction (spin down). Figure 3.11 shows the energy difference between the two states as a function of B_o. The energy of the dipole moment for each nucleus is:

$$E = -\gamma m \hbar B_0 \quad (3.3)$$

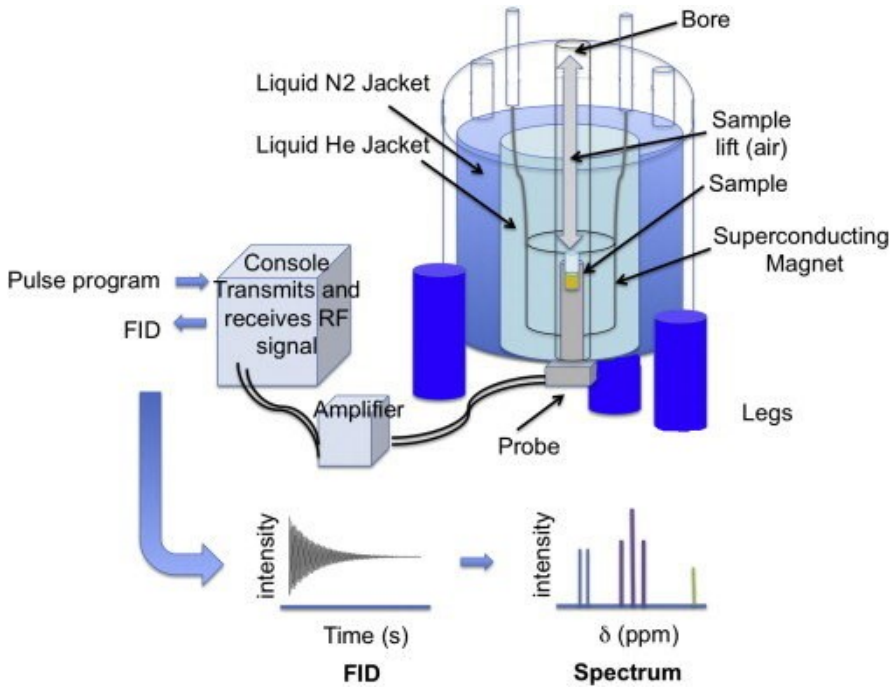

Figure 3.10 −Simplified diagram of a nuclear magnetic resonance spectrometer. At the heart of the 1 H NMR spectrometer is a superconducting magnet. This must be kept at 4 K, so needs to be emerged in liquid helium, which is hindered from evaporating by vacuum and nitrogen jackets. The probe, containing the RF coil sits in the bottom of the magnet within its bore. The sample is always contained within the 1 H NMR tube; it is gently dropped into the probe on a cushion of air. Here the superconducting magnet causes the protons magnetic moments to align with the magnetic field and the RF coil sends RF pulses to excite them and collects the free-induction decay (FID) as they relax back to equilibrium. The pulse programs are created using the computer and sent to the console, which acts both as a radiofrequency transmitter and receiver. The signals are amplified on transmission and receipt. The FIDs are Fourier transformed (mathematically deconvoluted) to produce 1 H NMR spectra of intensity versus chemical shift (d) using the computer. Reproduced with permission from *Atherosclerosis*, 2014, 237 (1), 287-300.[125] Copyright 2014 Elsevier. (CC By 3.0)

where γ is the gyromagnetic ratio, a constant that depends on the specific nucleus, m is the magnetic moment, and $\hbar$ is Plank's constant. At a specific B_o the energy difference between the two spin states is equal to:

$$E = \gamma \hbar B_o \tag{3.4}$$

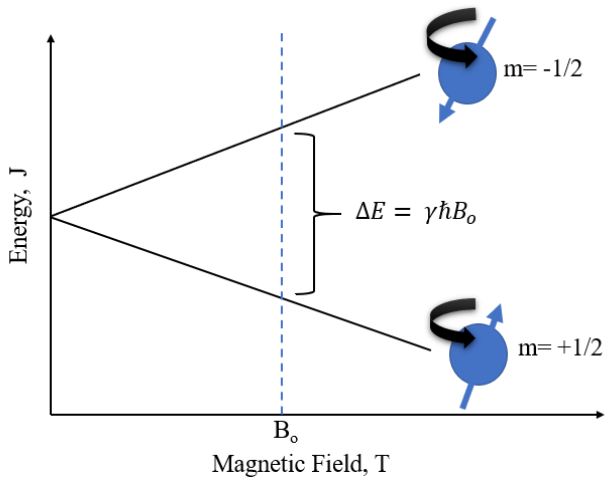

Figure 3.11− The energy difference between nuclei with spin-up (+1/2) and spin-down (-1/2) in an external magnetic field.

If no magnetic field is applied, the two states will be equally populated by nuclei. If a field is applied, the lower energy spin-state m=+1/2 will have a higher population of nuclei, resulting in the nuclei having a net alignment in the direction of the magnetic field.

The transition from the lower energy state (spin-up) to a higher energy state (spin-down) is done by applying a pulse of radiation at the specific frequency and given magnetic field strength for a short amount of time. The relationship between the applied radio frequency (Larmour frequency) ν, and magnetic field strength B_O is as follows:

$$v = (\frac{\gamma}{2\pi})B_o \qquad (3.5)$$

Therefore, to achieve resonance for the proton (^{1}H) the ratio of v to B_o must equal $\frac{\gamma}{2\pi}$. It should be noted that modern spectrometers use a superconducting magnet (Figure 3.10) that have magnetic fields that are extremely stable. Typically, frequency is varied to achieve resonance with a specific nucleus. However, the naming convention of NMR

spectrometers still uses the resonance frequency of ^{1}H NMR to describe the system. For example, a 7.05T magnet is referred to as a 300 MHz spectrometer.

The process of recording NMR spectra is done through the pulsed-Fourier transform (FT) method. When the sample is in the bore, in the magnetic field, a short pulse of high-power radiofrequency energy is applied. This pulse will excite all the nuclei of interest in the sample. Immediately after the pulse, the excited spins will precess around the external magnetic fields as a unit. Figure 3.12 shows the net magnetization vector (M_o) before (a) and after (b) an applied pulse. M_o is a sum of magnetic moments of all the spinning (precessing) nuclei that are aligned to the B_o direction.[126] Since the spin-up (+1/2) direction is the lower energy state, the M_o vector is in the +z direction. Figure 3.12 (b) shows the M, after a pulse was applied. M_o will start to tip into the xy plane. The magnetic component generated in the xy plane (FID) is detected as a function of time by a receiver coil that is in the xy plane. After the pulse, M will start to relax back down to the ground state (z-axis) also in a precessing motion. It should be noted that this relaxation does not give rise to an FID. The acquired FID is converted into the frequency domain using a Fourier transform. The frequency scale is then typically converted to the chemical shift scale (ppm) to be independent of magnetic field strength.

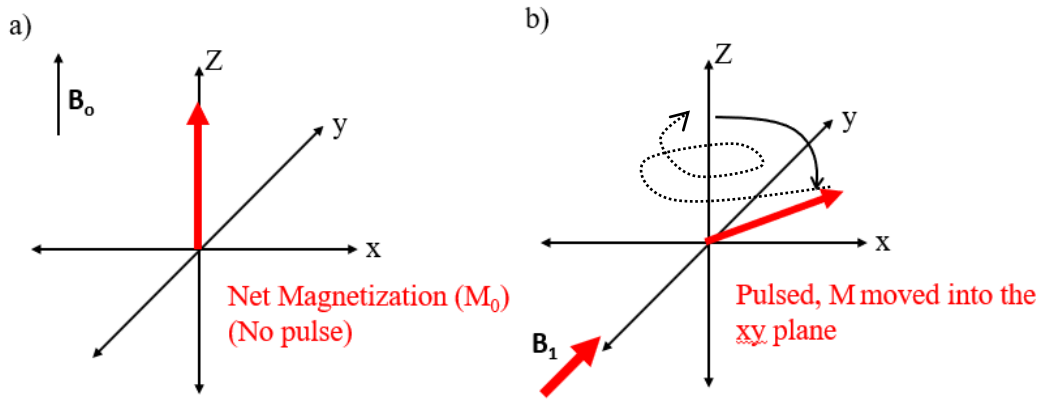

Figure 3.12−Representation of the net magnetization vector (M_o) before (a) and after (b) an applied pulse on a cartesian plane.

To increase the signal to noise ratio (S/N), the number of scans is increased. To double the S/N ratio, the number of scans needs to be quadrupled. However, the benefit of increasing the number of scans diminishes after a point. The work in Chapter 4 is quantitative, but it can only be considered quantitative if the appropriate time between scans is used. The spin-lattice relaxation or pulse delay time (T1) is the time it takes for the net magnetization (M) to return to the ground state. The time used between scans is normally recommended to be 5xT1 due to the exponential relationship between magnetization and time. Different nuclei relax at different rates. T1 values are dependent on nuclear environment, temperature, and solvent. If the T1 time selected is too short, the subsequent pulse could potentially push the signal out of the xy plane, resulting in attenuation or removal of the signal. For quantitative analysis, T1 values must be long enough to ensure that the nuclei can return to the ground state before the next pulse.

The NMR spectra contain characteristic peaks of each nuclei of interest. The peak location and splitting pattern depend on the local electronic environment of each nucleus.

Using ^{1}H NMR as an example, if the electron density around the protons is high, these protons will be shielded (closer to the 0 ppm point); if it is low, the peak is expected to be found downfield. The splitting pattern of each proton depends on how many unique neighbouring protons are next to it. The splitting pattern follows the *n+1* rule, where n is the number of unique neighbours.[124]

In Chapter 4, a Bruker Avance 300 MHz spectrometer was used to collect ^{7}Li, ^{1}H, and ^{19}F NMR spectra. A pulse length-based concentration determination (PULCON) method was used, allowing for an external standard to be used for quantitative ^{7}Li analysis.[127] For the ^{7}Li NMR measurements, 16 scans were done with a pulse delay time of 2 seconds. The external standard used was of the same composition described in Table 3.5. The PULCON set up was done using Bruker Topspin software 2.1.[128]The Pulcon method was used for ^{7}Li NMR measurements due to the difficulty in finding an internal standard that is inert to the lithium salt found in electrolytes. ^{1}H NMR and ^{19}F NMR experiments used the internal standard, 1,4-bis(trifluoromethyl)benzene, for quantitative analysis. For purposes of quantification and based upon relaxation time (T1) measurements, the pulse delay time was increased to 80 seconds for ^{1}H NMR and 10 seconds for ^{19}F NMR to ensure complete relaxation of the spins. The long relaxation times improve the accuracy of the results. ^{1}H NMR and ^{19}F NMR spectra were collected, accumulating 16 and 32 scans, respectively.

Figure 3.13 shows an example of a ^{19}F NMR spectra. The internal standard, 1,4-bis(trifluoromethyl)benzene peak at -63.8 ppm, was cut off for clarity. Figure 3.14 shows an example of a ^{1}H NMR spectra. The acetonitrile peak at 1.9 ppm was cut off for clarity. Lastly, Figure 3.15 shows an example of ^{7}Li NMR spectra containing $LiPF_6$ in solution. It

should be noted that any solvated Li ions will appear as a single peak in the ^{7}Li NMR spectra.

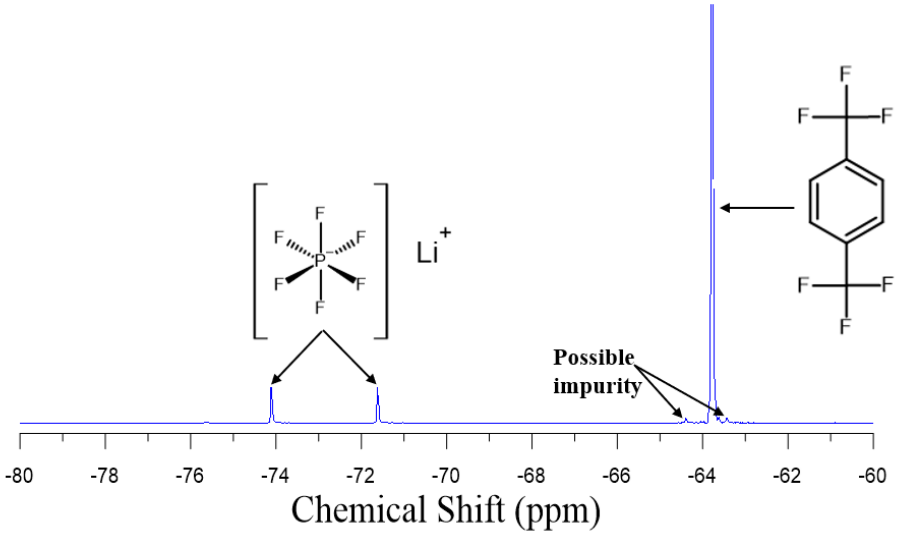

Figure 3.13− An example of ^{19}F NMR spectra. The peaks are identified.

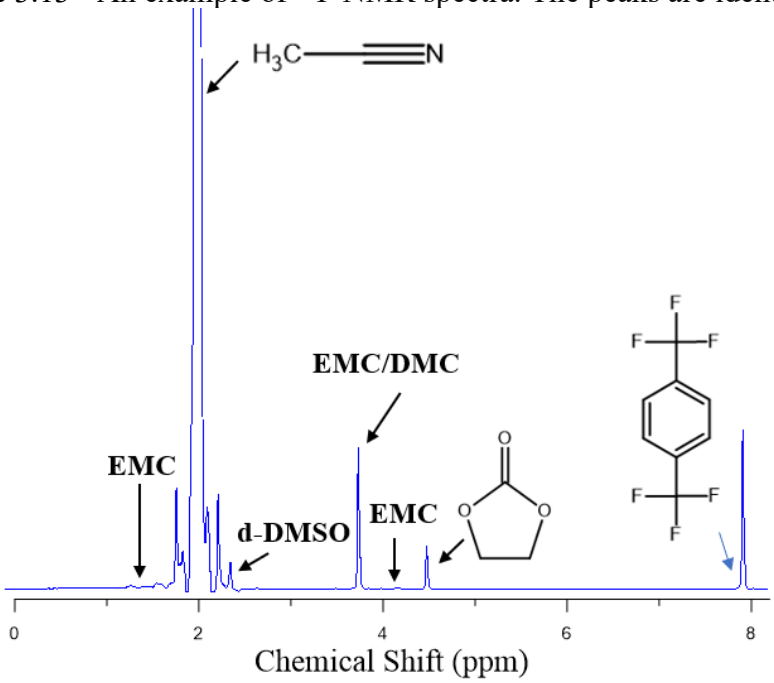

Figure 3.14−An example of ^{1}H NMR spectra. The acetonitrile peak is cut off for clarity.

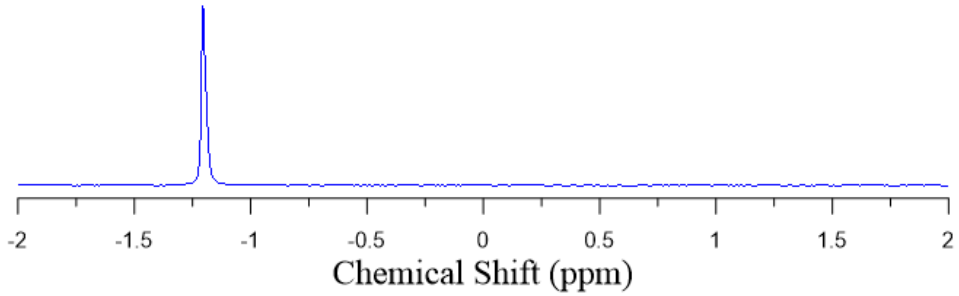

Figure 3.15- An example of a ^{7}Li NMR spectra.

3.13 NMR error treatment

NMR samples of known composition and concentration went through testing to verify the precision and accuracy of the measurements. Samples were prepared from 1.35 m $LiPF_6$ in EC:EMC (3:7 wt%) and diluted using the above-mentioned compounds. Consecutive ^{7}Li NMR measurements of a known solution were accurate (< 0.23% relative error) and precise (relative standard deviation ~1%). Table 3.3 shows results that describe the accuracy and precision of the method.

Table 3.3: Showing the accuracy and precision of Li measurements using a sample of known $LiPF_6$ concentration of 24.8 ± 0.3 mM prepared from a 1.35 m $LiPF_6$ in EC:EMC (3:7 wt%) electrolyte by dilution.

Trial	*Li^+ concentration in NMR sample reported by the spectrometer (mM)*	*% Error from Expected*
1	*24.79*	*0.2*
2	*24.77*	*0.2*
3	*24.81*	*0.1*
σ	*0.02*	

A different sample was prepared to verify instrument stability. This was also from a prepared 1.35 m $LiPF_6$ in EC:EMC (3:7) electrolyte by dilution. Table 3.4 shows that low variations were seen over the 4 day period.

Table 3.4: NMR sample containing 16.1 ± 0.3 mM $LiPF_6$, internal standard (1,4-bis(trifluoromethyl)benzene), d-DMSO and acetonitrile. Tested once a day over 4 days. Prepared from a 1.35 m $LiPF_6$ in EC:EMC (3:7) electrolyte by dilution.

Day	*Li^+ Concentration Result from NMR (mM)*	*% Error from Expected*
1	*16.25*	*0.8*
2	*16.29*	*1.0*
3	*16.36*	*1.5*
4	*16.30*	*1.1*
σ	*0.05*	

Table 3.5 shows that ^1H NMR and ^{19}F NMR experiments on a known sample found small differences between the measured and expected organic compound concentrations. These measurements were done consecutively.

Table 3.5: Prepared extraction solution containing (16.2 ± 0.3) mM of $LiPF_6$ in EC(66.3 ± 0.3 mM):EMC, internal standard (1,4-Bis(trifluoromethyl)benzene), d-DMSO and acetonitrile. Prepared from a 1.35 m $LiPF_6$ in EC:EMC (3:7 wt%) electrolyte by dilution.

Trial Number	*PF_6^- concentration reported by ^{19}F NMR (mM)*	*% Error from expected*	*EC concentration reported by ^1H NMR (mM)*	*% Error from expected*
1	*16.8*	*3.5*	*65.5*	*1.2*
2	*16.6*	*2.3*	*69.7*	*5.1*
3	*16.6*	*2.2*	*64.7*	*2.5*
σ	*0.1*		*3.0*	

The same sample was also measured over four days to verify instrument stability. Table 3.6 shows that low variations were seen over the 4-day period.

Table 3.6: NMR sample of containing 16.2± 0.3 mM of $LiPF_6$ in EC (66.3 ±0.3 mM):EMC, internal standard (1,4-bis(trifluoromethyl)benzene), d-DMSO and acetonitrile tested once a day over 4 days. Prepared from a 1.2 m $LiPF_6$ in EC:EMC (3:7 wt%) electrolyte by dilution.

Day	*PF_6^- concentration from ^{19}F NMR measurements (mM)*	*% Error from expected*	*EC Concentration from ^1H NMR (mM)*	*% Error from expected*
1	*16.83*	*4.40*	*65.7*	*0.9*
2	*16.98*	*5.33*	*63.2*	*4.7*
3	*16.45*	*2.05*	*68.5*	*3.3*
4	*16.52*	*2.48*	*65.3*	*1.5*
σ	*0.3*		*2.2*	

3.14 Calculating $LiPF_6$ concentrations

To calculate $LiPF_6$ concentrations, quantitative results from NMR and semi-quantitative results from GC-MS were combined. GC-MS can only report the concentrations of analytes within the GC vial. Therefore, the ratios between known components are only used for analysis. First, GC-MS mass ratios were used to determine the mole ratios of EC, EMC and DMC. This was necessary as electrolyte systems for LIB's often comprise several organic carbonates with similar chemical structures varying even just by a single methyl group (i.e. methyl group on EMC vs. DMC) and are difficult to distinguish with this NMR instrumentation. The mass ratios from GC-MS are applied to the EC concentration (determined from ^1H NMR) to determine the concentration of EMC and DMC. Using ^{19}F NMR or ^7Li NMR acquired spectra, the number of mols of the PF_6^- anion or Li^+ cation is

determined, respectively. The molality is then able to be calculated using moles of salt and total mass of solvent (uncertainty propagated appropriately).

3.14 Micro-X-ray Fluorescence spectroscopy (μ-XRF)

Micro-X-ray Fluorescence spectroscopy (μ-XRF) is used in Chapter 4 to see the degree of Ni, Mn and Co deposition at the negative electrode. This technique follows the same principles of X-ray Fluorescence (XRF) but at a higher spatial resolution that allows for fine two-dimensional mapping of the sample.[129]

Figure 3.16 shows a diagram of the basic principles of XRF. To begin, the sample is bombarded with an X-ray beam, which causes inner shell electrons in the K shell to get ejected out of the atom. Electrons from the outer L or M shell fill the void left behind, emitting fluorescence radiation K_α and K_β respectfully. The emitted radiation is measured by a photon detector where the specific radiation can be identified and quantified. Different atoms have different relaxation processes that have specific energies associated with these processes. For example, $Mn_{K\alpha 1}$ has an energy of 5.900 keV and $Ni_{K\alpha 1}$ is 7.48 keV.[130]

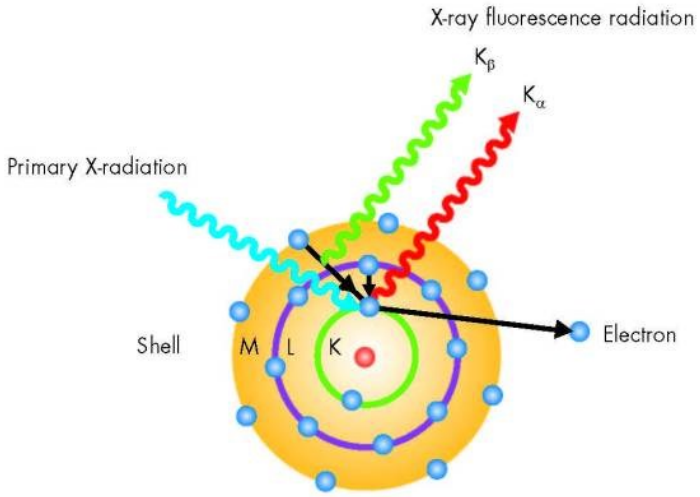

Figure 3.16−A diagram showing the basic principles behind XRF.[131]

3.15 *μ-XRF Measurements (performed by Ahmed Eldesoky)*

μXRF calibrants for Ni. Mn and Co were prepared as previously described.[60] A M4 Tornado Micro-X-Ray Fluorescence Instrument at the University of New Brunswick (Bruker, Madison, WI, USA) was used to obtain the *μ-XRF* data. The Mn-coated fresh electrode was used to calibrate signal counts measured. The transition metal (TM) signal to known mass loading ratio was determined at four different positions on the calibrant and their average determined the signal count to mass ratio used to convert TM net counts from each sample to a mass loading in terms of μg/cm^2. The fractional error in the data was taken to be the same as the ratio of the standard deviation of the four calibration measurements divided by their average. Cells were discharged to 2.5 V and were cut open in a fume hood. The cell stack was unrolled and allowed to dry completely before μXRF analysis. A portion of the negative electrode was cut and mounted on a flat polyacrylic plate with double-sided tape, which was placed on the μXRF stage. Sample scanning was carried out using a 45

μm step size with a 25 μm spot size, a scanning rate of 4.00 mm/sec and a 200 μA tube current in the range of 0 to 50 keV under vacuum (<20 mbar).

Figure 3.17 (a) shows an example of Mn loading on a negative electrode from a dry NM532/graphite cell (0.0 ± 0.0 ug cm^{-2}). Figure 3.17 (b) shows Mn loading on a negative electrode from an NM532/graphite cell that went through multiple charge and discharge cycles.

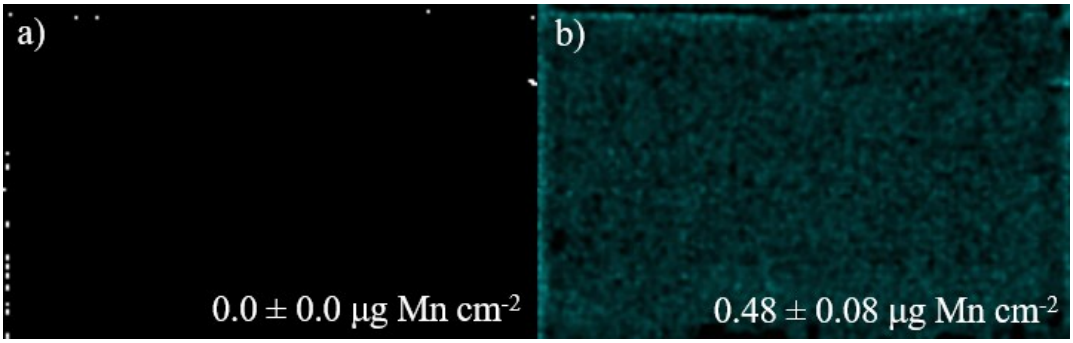

Figure 3.0.17 −a) Mn μ-XRF signal for a negative electrode from a dry NM532/graphite cell. b) Mn μ-XRF for a negative electrode from a NM532/graphite cell that went through multiple charge and discharge cycles.

3.16 Summary

Methods used in Chapters 4 and 5 have been described in this chapter. The extraction technique and the sample preparation technique were developed to obtain as much electrolyte from an intact cell studied in Chapter 4. The combination of GC-MS and NMR allowed for quantification of the salt content. After analysis, electrodes were able to be recovered for additional analysis by μ-XRF. The NMR method will be used solely in Chapter 5; however, further details specific to the measurement will be described in that chapter.

CHAPTER 4 − INVESTIGATING OPTIMAL VINYLENE CARBONATE AND ETHYLENE SULFATE LOADINGS IN NMC532/GRAPHITE CELLS

This work was adapted from the prepared manuscript:

T. Taskovic, L.M Thompson, A. Eldesoky, M.D Lumsden, and J.R Dahn

Optimizing Electrolyte Additive Loadings in NMC532/graphite Cells: Vinylene Carbonate and Ethylene Sulfate

Tina Taskovic, prepared the pouch cells, measured the volume of gas produced and performed the EIS measurements. Tina Taskovic and Lauren Thompson developed the electrolyte extraction method, and validation. The NMR method was developed by Tina Taskovic, Lauren Thompson and Mike Lumsden. The GC-MS sample preparation and method were developed by Tina Taskovic and Lauren Thompson. Ahmed Eldesoky performed μ-XRF analysis. Tina Taskovic prepared all the figures. Lauren Thompson and Jeff Dahn provided guidance throughout method developments, validation, and interpretation. Tina Taskovic prepared the manuscript which was edited by the appropriate authors.

This chapter shows the cycling results along with post-cycling analysis of cells with different weight percentages of additives vinylene carbonate (VC) and ethylene sulfate (DTD). Cells underwent prolonged charge-discharge cycling at 20°C and 40°C. The volume of gas produced during formation and cycle testing was measured. The impedance spectra of the cells before and after cycling was measured. After testing, the electrolyte was extracted for study by nuclear magnetic resonance spectroscopy (NMR) and gas chromatography/mass spectroscopy (GC-MS) to determine what changes in electrolyte

composition had occurred. Some cells had their negative electrodes studied by scanning micro-X-ray fluorescence to quantify the amount of transition metals which transferred from the positive electrode to the negative electrode during the testing.

4.1 Cycling, Gas and EIS Results

The combination of VC and DTD, discussed by Li et al., works synergistically to improve cell lifetime.[132] Cells containing VC in combination with other additives like DTD mitigate against impedance growth seen in cells only containing VC.[113] Cells only containing DTD have been shown to have shorter lifetimes compared to dual additive cells.[133] VC and DTD combinations were only considered because a significant amount of work is required to optimize a binary combination.

Figure 4.1 and 4.2 shows the normalized capacity and ΔV versus cycle number for the NMC532/graphite cell testing. Four replicate cells were filled with one of the eight electrolyte blends, so that one pair was cycled at 20°C and other at 40°C. The post-cycling analysis was split between the pairs; one underwent NMR and GC-MS analysis, and the other was used for μ-XRF analysis. Most combinations of VC and DTD lead to cycle lifetimes reaching over 2000 cycles with less than 20% capacity loss. At 40ºC, cells with 1% VC or 2% VC+3% DTD showed the largest capacity losses. At 20ºC, cells with 2% VC or 2% VC+3% DTD had the largest capacity losses, which also had the largest changes in ΔV during cycling. Cells containing high amounts of VC and DTD (sum being 4% by weight or greater) displayed higher capacity losses than those with less additive. As expected, cells solely containing VC underperformed.[134] The underperforming cells had

the commonality that their respective ΔV values increased during cycling, signifying an increase in internal resistance.

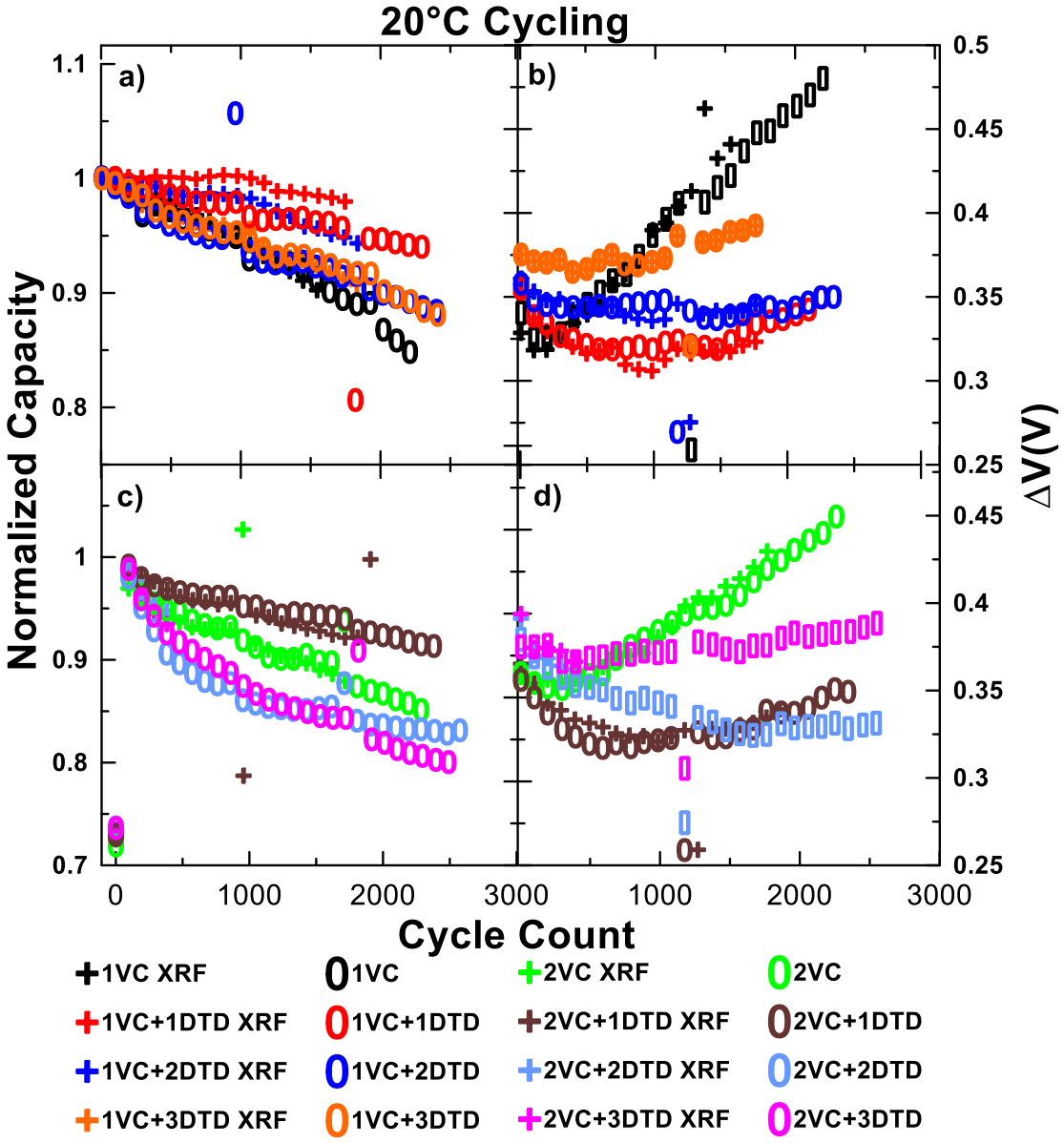

Figure 4.1 Normalized capacity (cycle 5) and voltage polarization (ΔV) vs cycle count results for the prepared cells. a-d, show the results for the 20°C cycling.

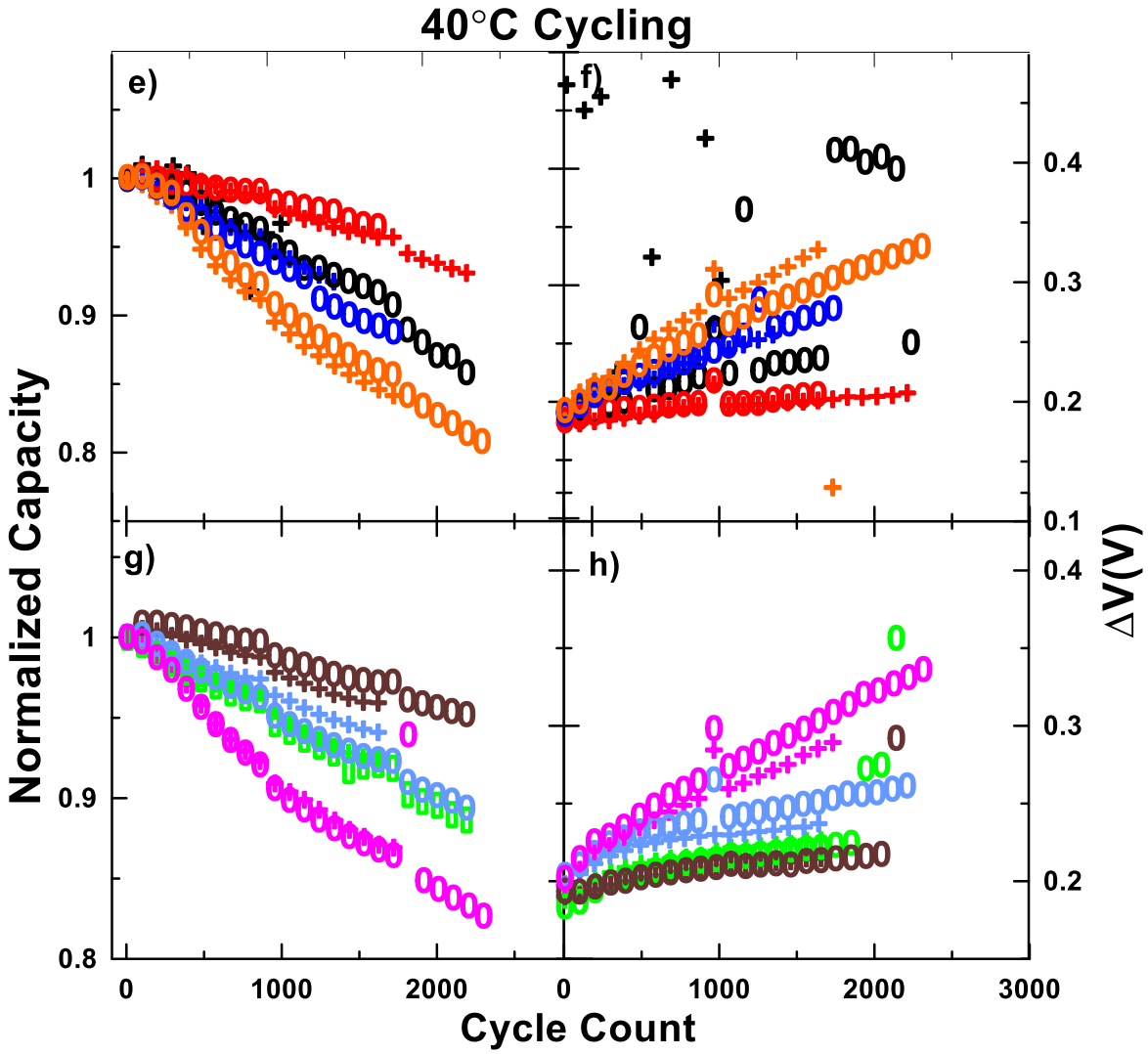

Figure 4.2 Normalized capacity (cycle 5) and voltage polarization (ΔV) vs cycle count results for the prepared cells. e-h, show the results for the 40°C. The legend in Figure 4.1 also applies to all the graphs in this figure.

The best performing cells were those that contained 1% DTD with either 1% VC or 2% VC at 20 and 40°C. In Figure 4.3, the influence of the amount of DTD on capacity retention in a cell is clearly demonstrated. Cells with 1% DTD had the best capacity retention at cycle 1700. Cells containing greater than 1% DTD had similar results to cells with only VC. This suggests that excess DTD is not desirable.

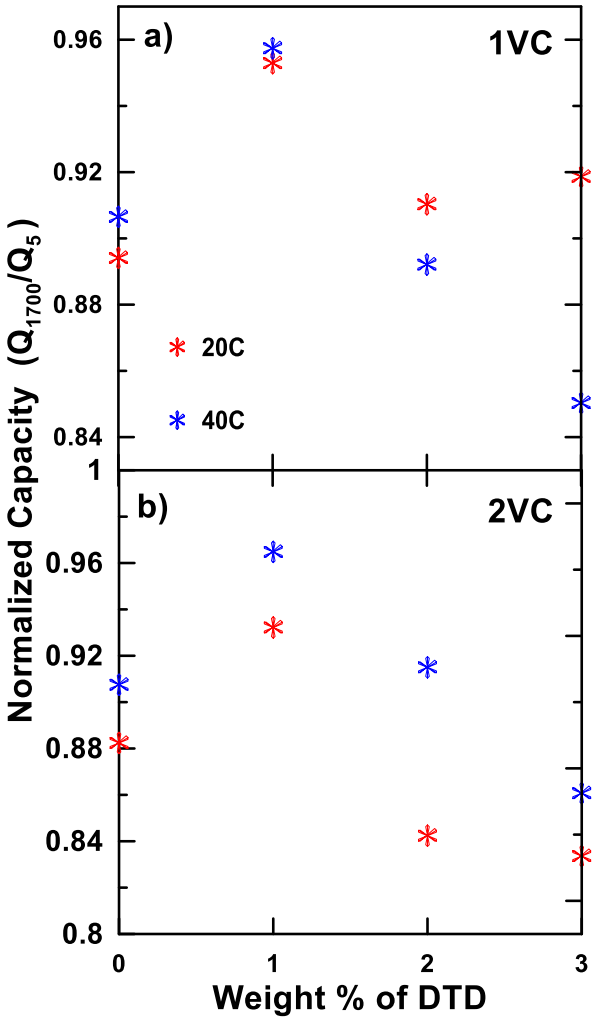

Figure 4.3 Normalized capacity at cycle 1700 (Q1700) taken from the normalized capacity (Q5) data seen in Figure 1 vs the percent amount of DTD in the cell. Panel a) shows results for 1VC cells. Panel b) shows results for 2VC, results are shown for both 20°C and 40°C cycling.

Madec et al. showed that cells with only DTD tend to eventually fail.[135] Li et al. also studied DTD without VC in Li/graphite half cells and reached a similar conclusion that 1% DTD had the best cycling performance.[136] DTD has been shown to be beneficial to the formation of the SEI.[137] DTD has been described to go through a ring-opening reduction similar to EC, producing lithium sulphites, lithium sulfates, ethylene gas and other lithium alkyl sulphites that are involved in the creation of a robust SEI.[136,138]

Figure 4.4 (a) shows the average volume of gas produced after formation. The more DTD is added to the cell, the more gas is produced. This is observation has been made before.[138] However, less than 1 mL (4 mL/Ahr) of gas was produced. The excess gas is a result of the decomposition of DTD and most likely this gas is ethylene.[138] The cells with 2% VC had slightly less gas production on average. There are no correlations between the cycling results and the amount of gas produced during formation, which was removed from the cells after formation by degassing. Further analysis is needed to identify and quantify the various gasses formed after the initial cycle. Figure 4.4 (b) shows the average volume change of cycled cells sorted by temperature. The volume change could have additionally come from possible electrode swelling. Overall, for all electrolyte blends, less gas was produced during cycling than during formation. Volume is greater for the cells cycled at 40°C compared to 20°C because increased temperature promotes the kinetics of parasitic reactions. Cells containing 1% DTD and either 1% VC or 2% VC show less volume change than the other additive combinations; however, this is more noticeable at 40 °C.

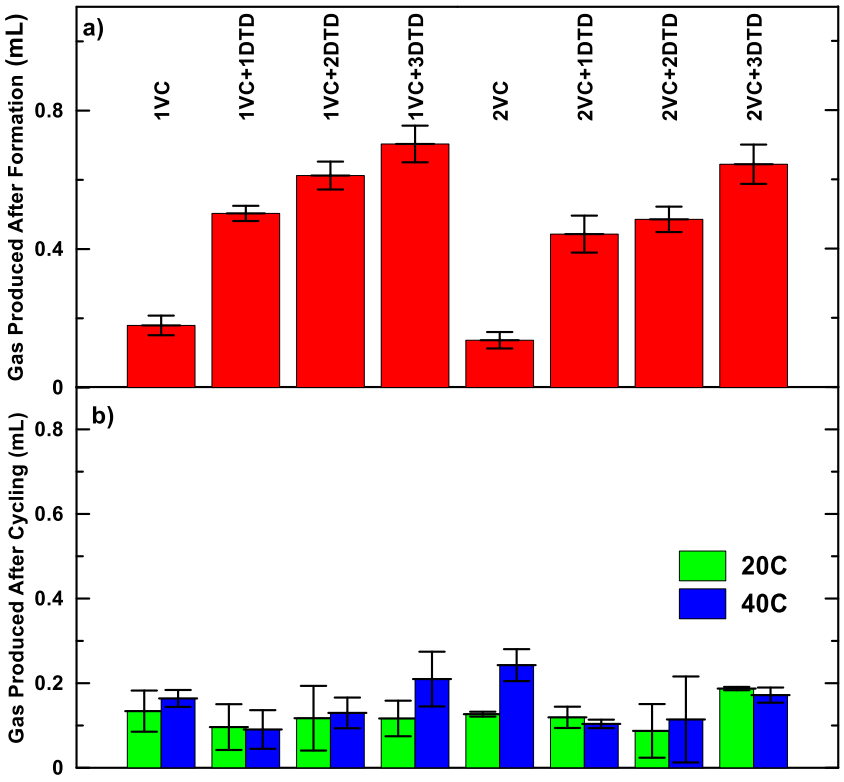

Figure 4.4 a) Average volume of gas produced (mL) after formation. b) Average volume of gas produced (mL) after cycling for each electrolyte blend. Separated by temperature.

Figure 4.5 (a) shows EIS results for the cells before and after cycling. Figure 4.6 a) and b) shows an example of the corresponding Nyquist plots for cells before cycling. The graph displays the average R_{ct} (Ω/cm^2) measured for each cell type. The results are further separated by cycling temperature. Results for 20°C are in green and for 40°C in blue. Cells containing DTD in most cases had lower R_{ct} values on average after cycling when compared to the results after formation. Cells without DTD saw R_{ct} increase after cycling. Figure 4.5b shows the percentage increase in ΔV per cycle which occurred during the testing in Figure 4.1 and 4.2. There is little correlation between Figures 4.5a and 4.5b which suggests the change in DC resistance of the cell is not dominated by changes in charge transfer resistance. All cells with 1% DTD and either 1 or 2% VC show very little increase in ΔV during testing at either 20 or 40°C.

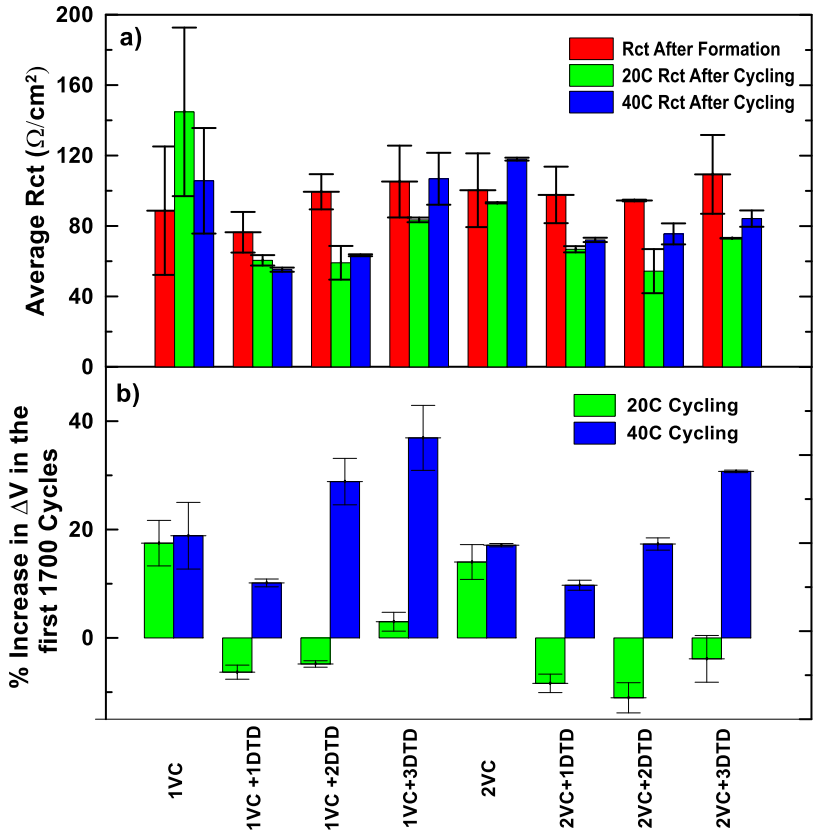

Figure 4.5 (a) EIS results for all cells after formation (red) and post-cycling. Post-cycling results are differentiated, 20°C cells are in green and 40°C cells are in blue. b) The percent increase in ΔV in the first 1700 cycles for each cell type, separated by temperature.

a)

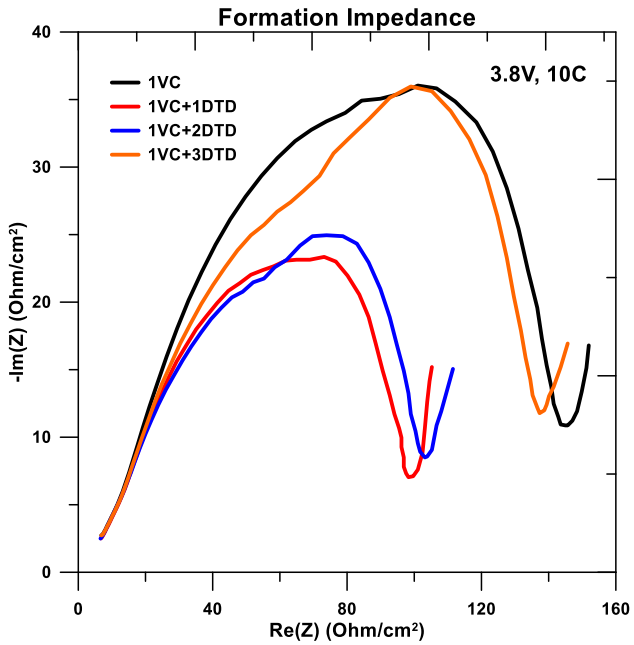

b)

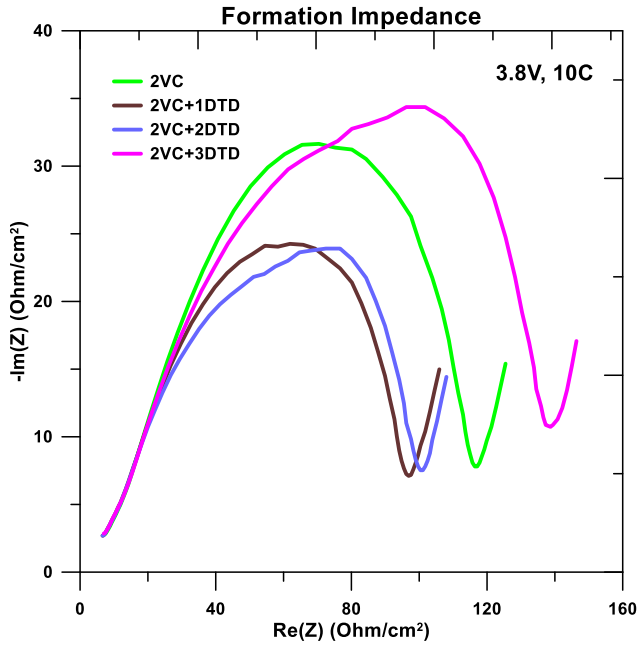

Figure 4.6 a) Shows the a raw EIS spectrum of all cells containing 1%VC in the electrolyte. b) Shows the a raw EIS spectrum of all cells containing 2%VC in the electrolyte EIS measurements were taken at 10 ± 0.1°C at 3.8V. Data were collected with ten points per decade from 100 kHz to 10 mHz with a signal amplitude of 10 mV

4.2 NMR and GC-MS Results

Figure 4.7 shows the Li^+ and PF_6^- molality in the electrolytes of the cells displayed in Figure 1 after testing as measured by NMR. No evidence of $LiPO_2F_2$ (lithium difluorophosphate) was seen in any of the samples measured. The black dotted line in each panel is the initial molality of the salt (1.33 m). In most cases, the Li^+ and PF_6^- results are statistically the same due to the confidence intervals for the ^{19}F NMR and ^{1}Li NMR measurements. Both the 20 and 40°C results show that there was a significant decrease in salt molality during cycling for cells with 1% DTD and either 1 or 2% VC. This is rather surprising given that these same cells were those with the best capacity retention and the smallest impedance growth. It is known that electrolyte oxidation involving PF_6^- can remove Li^+ ions from the electrolyte in order to maintain charge neutrality.[139] These removed lithium ions would then contribute to the lithium inventory of the cell, hence increasing capacity.

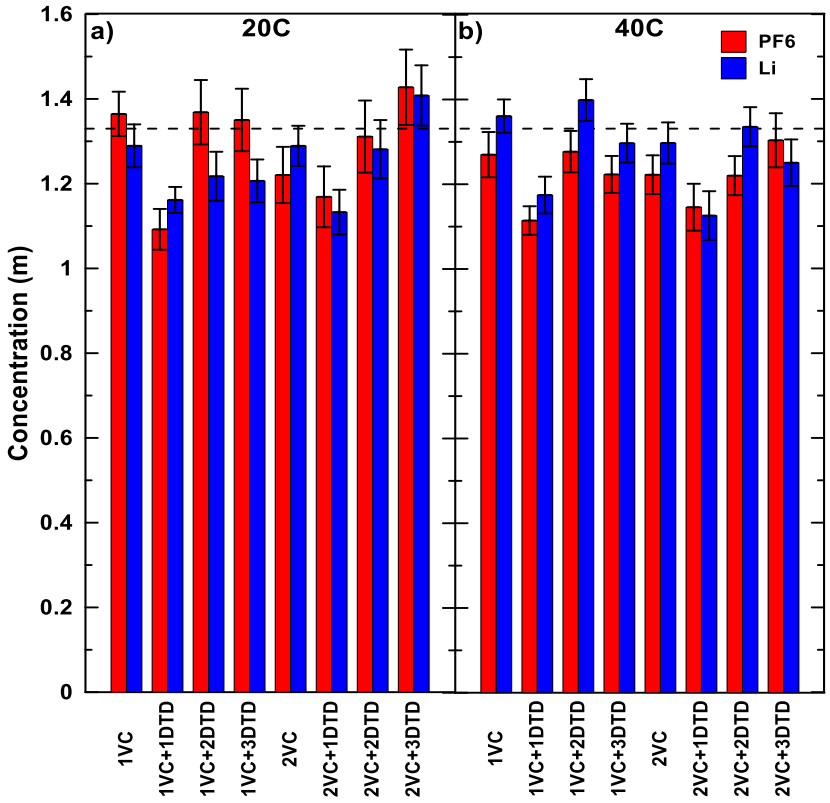

Figure 4.7 Average calculated Li^+ and PF_6^- concentrations for each electrolyte blend. a) Results shown for cells cycled at 20°C. b) Results shown for cells cycled at 40°C.

If a cell contains 1 mL of electrolyte with 1.5 M $LiPF_6$, then the electrolyte contains 1.5×10^{-3} moles of Li^+. Figure 4.7 suggests that approximately 0.2 M of Li^+ from the electrolyte could be added to the inventory for the cells with 1% DTD. The capacity of extra lithium would be 8 mAh corresponding to 3×10^{-4} moles of Li^+. Figure 4.1 and 4.2 shows that the fractional capacity retention for cells tested at 40°C is improved by about 0.05 between cells with 1% VC + 1% DTD or 2% VC + 1% DTD compared to cells with 1% VC or cells with 2% VC. Since the cells have an initial capacity of 215 mAh, this 0.05 improvement in fractional capacity retention corresponds to 11 mAh which is close to the 8 mAh that could be due to the inventory added from the loss of salt. This simple calculation does not prove that loss of Li salt is the reason for the improved capacity retention of cells with VC + 1% DTD, but it is certainly very suggestive.

Figure 4.8 shows the ratio of EC to EMC+DMC in these cells after the testing period. The results are further separated by temperature, and the original ratio is denoted by the black dotted line. Most cells showed the consumption of linear carbonates over EC, and cells with a higher percentage of DTD typically had a greater EC to a linear carbonate ratio. No DEC or transesterification products (like DMOHC and DEOHC) were detected by the GC-MS, as well as no VC or DTD. Overall, no major changes were found to occur in the electrolytes of the cells analyzed. This speaks to the robustness of the electrolyte, being able to withstand a relatively high charging rate and over 2000 cycles without major changes observed in the electrolyte.

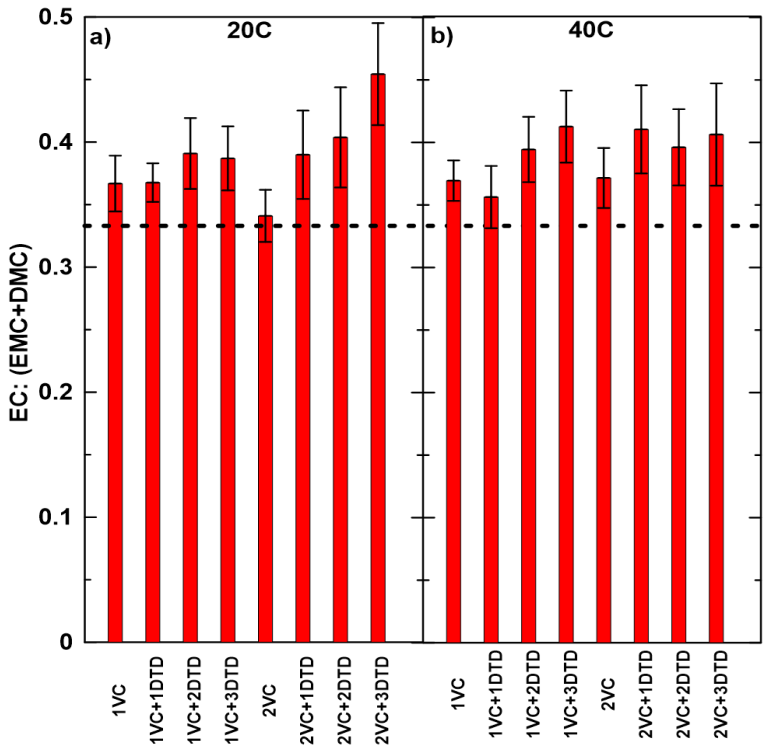

Figure 4.8 Ratio of EC:(EMC+DMC) (linear carbonates) found in cells after cycling using GC-MS. a) Results shown for cells cycled at 20°C. b) Results shown for cells cycled at 40°C.

4.3 μXRF results

Transition metal deposition on the negative electrode was examined using scanning μXRF. Figure 4.7 shows the results of the μXRF measurements for Ni, Co, and Mn for cells of each electrolyte type. The results are further separated by the cell cycling temperature. It is found that 0.01%-0.03% of the total original amounts of transition metals in the positive electrode were deposited onto the negative electrode from the samples tested. The levels of transition metals are in agreement with the levels reported by Thompson et al. who included additives in their cells, and much lower than the levels

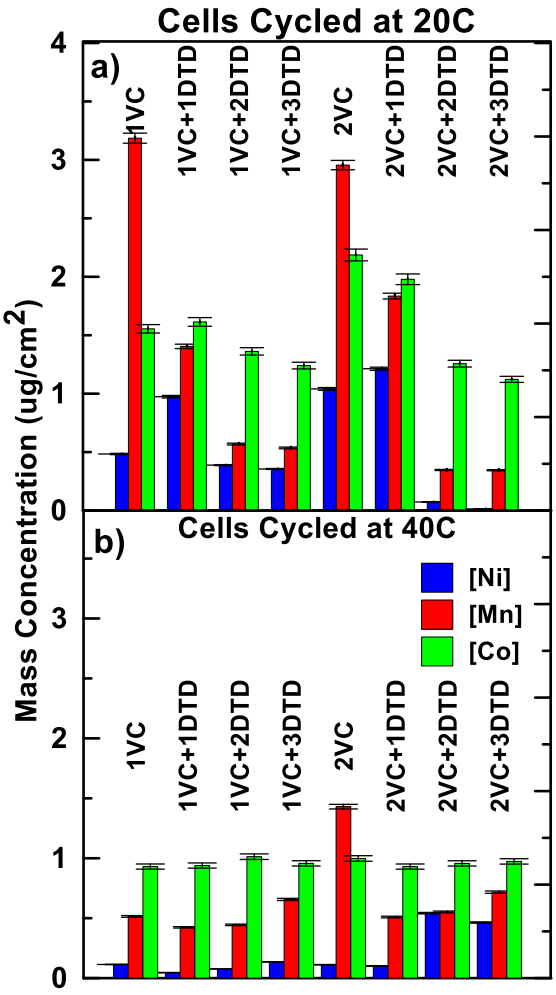

Figure 4.9 μXRF results of negative electrode pieces for each electrolyte blend. Results are reported for Ni, Mn and Co. a) Results shown for cells cycled at 20°C. b) Results shown for cells cycled at 40°C.

reported by Gilbert et al. who did not include additives in their cells.[60,97] The overall amount of transition metal deposition was higher for the 20°C samples than the 40°C samples. It is possible that small amounts of lithium plating could be occurring in cells tested at 1C at 20°C. Perhaps the plated lithium can undergo ion exchange effectively with dissolved transition metals as $xLi + M^{x+} \rightarrow xLi^{+} + M$, hence leading to higher amounts of transition metals on the negative electrode in cells tested at 20°C. In most samples, Co and Mn comprised most of the transition metal dissolution. Ni concentrations were small,

especially at 40°C. For the 20°C measurements, the VC only samples had the highest Mn concentrations compared to the other samples containing DTD. However, this observation does not replicate in the 40°C samples, where the 1% VC sample was very similar to the other DTD samples. If one only looks at the 20°C samples, the presence of DTD may somehow prevent transition metal dissolution. Again, this observation is not seen for the 40°C samples.

When comparing the μXRF results in Figure 4.9 to the cycling results seen in Figure 4.1 and 4.2, the capacity fade seen does not correlate well with the amount of transition metal dissolution. The capacity fade is caused by a different mechanism. Harlow et al. showed that for cells of the same chemistry as those considered here tested at 40ºC, the major contributors to capacity loss were lithium inventory loss and impedance growth.[70]

4.4 Concluding Remarks

NMC532/graphite cells made with a variety of combinations of the electrolyte additives VC and DTD went through a prolonged charging/discharging protocol at 1C between 3.0 V to 4.3 V at both 20 and 40ºC. This allowed for a thorough screening of the cells to determine which combination of the two additives yielded cells with the least amount of capacity fade and lowest internal resistance changes. Quantitative analysis of the electrolytes after cycling determined the composition changes. Finally, the transition metal loading on the negative electrode was measured.

At both 20 and 40ºC, the cells with the additives 1% VC + 1% DTD and 2% VC+1% DTD showed the best capacity retention. Most of the cells attained over 2000 cycles with the best performing cells showing no indication of imminent failure. EIS

measurements showed that cells with DTD had lower charge transfer impedance after cycling than cells without DTD. The additive choice, 1% VC +1% DTD would be a good option for an application that favours lower impedance. It was also shown that the more DTD added to a cell, the more gas would be produced during formation. Cells with 1% VC or 2%VC+3%DTD had some of the worst cycling performances and also the largest volumes of gas produced during formation. During cycling these cells produced volumes of gas only slightly larger than that of the best performing cells.

NMR results suggested that the cells containing 1% DTD had more significant salt consumption from the electrolyte than cells without or with more than 1% DTD. This was surprising as these cells had the best performance. It was suggested that this salt loss may add Li to the cycling inventory but further work will need to be done to verify the mechanism. GC-MS work showed no transesterification by-products or other post-cycling products. The EC to linear carbonate ratio increased when compared to the original electrolyte suggesting the consumption of linear carbonates during the long term cycling. In most cases, change in the EC:linear carbonate ratio was more significant for cells containing more than a total of 3% of the additives. Since no other products were seen (at the sensitivity of the instruments used), it is assumed the reacted solvent and salt contributed to the SEI formation at one or both electrodes. This is opposite to what is seen in the literature where studies of the thermal and electrochemical degradation of electrolytes produced several decomposition products.[96,140,141] However, these papers studied electrolytes systems without any additives, showing the importance of additives to electrolyte stability.

Transition metals transferred to the negative from the positive electrode represented 0.03% or less of the original transition metals in the positive electrode. Cells cycled at 20°C had a higher loading of transition metal on the negative electrode surface compared to the 40°C cells. The reason behind this is unclear and warrants further investigation. Due to the limited amount of transition metal transferred to the negative electrode, it is unlikely that transition metal dissolution contributed significantly to the capacity loss seen.

CHAPTER 5 − STUDYING THE DYNAMICS OF $LIPF_6$ SALT IN ELECTROLYTE SOLVENTS

This work was adapted from the article:

E.R. Logan, D.S Hall, Marc M.E. Cormier, T. Taskovic, Michael Bauer, Ines Hamam, Helena Hebecker, Laurent Molino, and J.R. Dahn

Ester-Based Electrolytes for Fast Charging of Energy Dense Lithium-Ion Batteries,

J. Phys. Chem. C 2020, 124, 12269−12280

Tina Taskovic and Eric Logan performed the PFG-NMR measurements and subsequent figures.

5.1 Importance of transport properties to Li-ion cell modelling

As discussed in the background, Li-ions cells require an electrolyte that will allow for efficient transport of Li-ions between the electrodes (high conductivity). Measuring conductivity is a common and easy way to evaluate an electrolyte in question.[142] However, conductivity, dielectric constant, and viscosity alone do not give a full picture of the ionic transport in an electrolyte.

Many researchers who study cell performance using physics-based models require additional transport properties to have their models be relatively accurate. Some of these properties include the Li-ion transference number, diffusivity, and activity coefficients.[39] This chapter focuses on measuring the diffusivity values of the $LiPF_6$ salt in two different electrolyte environments, DMC, and MA (Methyl Acetate).

Outside of the desire to understand the bulk transport properties of electrolytes on a fundamental level, there is a demand from the electric vehicle (EV) industry to push for higher charging rates. The US Advanced Battery Consortium has sent the goal to produce cells that can achieve 80% capacity in 15 mins by 2023.[143] High discharging rates are only required for times when high power is needed (i.e. the acceleration of an electric vehicle). One method to increase charging rates is to create cells with thin electrodes that inherently have small diffusion lengths.[144] However, thinner electrodes limit the volumetric energy density of a cell, which is not ideal for EV applications. Thus, the electrolyte has been the focus when it comes to designing cells capable of fast charging rates. Currently, some electrolyte systems are known to allow plating of lithium on the graphite electrode during a high-rate charging.[145] Lithium plating is a severe degradation mechanism that occurs when the graphite potential dips below 0 V vs Li/Li^+.[146] This scenario follows Equation 5.1.

$$xLi^+ + xe^- \rightarrow xLi \qquad (x \leq 0 \leq 1) \qquad (5.1)$$

Faster charging rates can lead to the incomplete utilization of the active material during operation. Slow Li^+ diffusion (D) through the electrolyte will increase overpotentials, which can lead to lithium plating at the negative electrode. Another valuable property is the Li^+ transference number (t^+), which is defined as the fraction of ionic current contributed by Li^+ movement. If the transference number is low < 0.5, a concentration gradient will form during battery operations, as most of the total ionic conductivity comes from the anion motion. These gradients become exacerbated at higher charging rates that can also limit the operating voltage of the cell and limit the thickness of the electrodes used. A higher cation transference number would lessen these gradients and

facilitate faster-charging rates. A cation transference number of 1.0 would be the ideal scenario. Figure 5.1 shows a representation of how increasing the Li^+ transference number lessens the concentration gradient across the cell for increasing charging rates. Upon charge, ions move from the positive electrode to the negative electrode causing the salt concentration to increase on the positive electrode side.

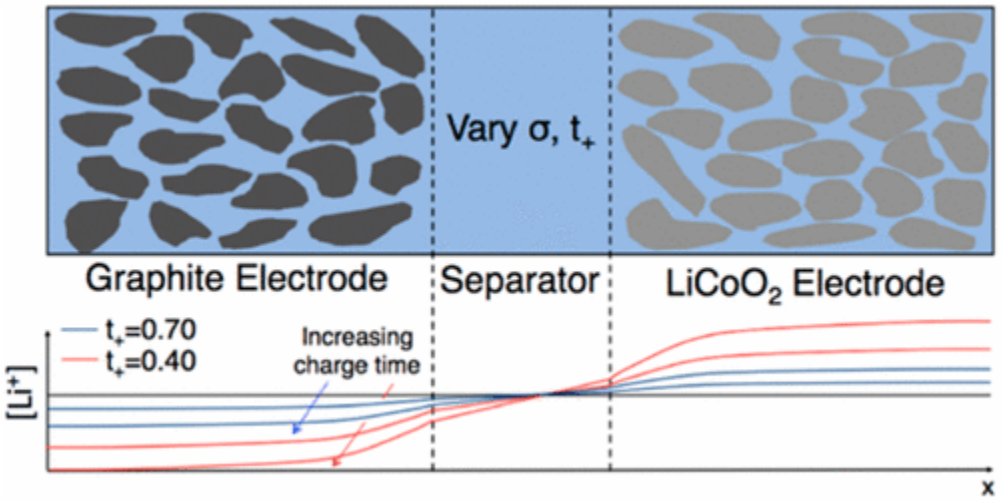

Figure 5.1 A representation of Li^+ concentration variation across a cell (x=cell coordinate position) during charge. The black line is the scenario where the t^+ =1.0. The blue line is when t^+ =0.7, and the red line is when t^+ =0.4. The scenarios where the charging rate is increased are marked and show an increase in gradient size. Reproduced with permission from ACS Energy Lett. 2, (11), 2563-2575 (2017). Copyright 2017, American Chemical Society.[147]

The diffusion coefficient and transference number determine the concentration gradients that form under load. Lastly, the salt activity coefficient $f^{\pm}$ is another valuable property that determines any voltage polarization resulting from the gradient.[148] Figure 5.2 shows examples of electrolyte salt concentrations gradients across a cell during discharge. This work was a simulation of an NCA/graphite cell; the rate (1C) and the thickness of the electrodes were kept constant. During discharge, ions move from the negative electrode to the positive, causing a shift in salt concentration in the opposite direction. As the cell

continues to discharge, at one point, the salt concentration dips to zero on the positive electrode side. Once salt concentration dips to zero, the ionic current is not accessible to that area.

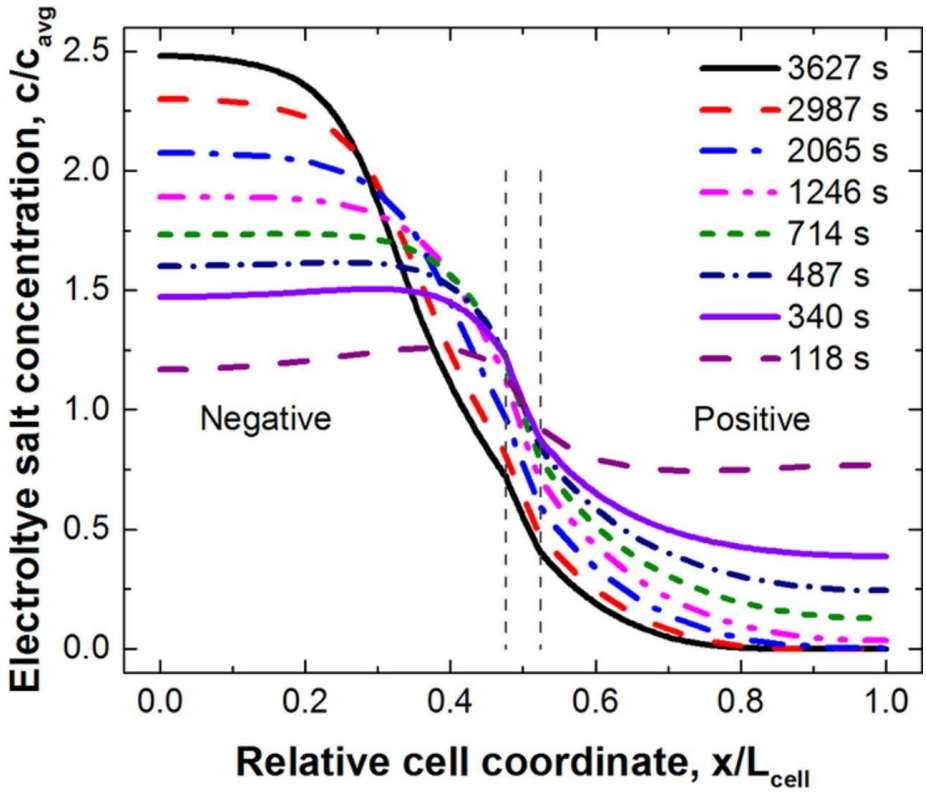

Figure 5.2 Simulated electrolyte salt concentration as a function of cell coordinate of an NCA/Gr cell discharged at the C/1 rate. Both positive and negative electrodes were 245 μm in thickness. Reproduced with permission from J. Electrochem. Soc., 163, (2), A138-A149 (2016). Copyright 2001, The Electrochemical Society.[149] Under CC BY-NC-ND 4.0.

The transport properties D, t^+ and $f^{\pm}$ must be known to create models and simulations of cell performance. However, data is needed for a range of concentrations. Despite electrolytes having concentrations around 1.0 M to 1.5 M, it is known from simulations that the localized concentration within the negative electrode can exceed 2 M (Figure 5.2 is also an example).[149,150] Measuring transport properties for a variety of concentrations is therefore useful for accurate electrochemical modelling.

Aliphatic esters are increasingly studied for use in Li-ion cell electrolytes due to their low melting points and viscosities. Commonly they are added as a co-solvent to traditional carbonate-based electrolytes and have been found to mitigate the issue of lithium-plating at high charging rates. Lower molecular weight esters (like MA) tend to have the highest conductivity but tend not to form stable SEI's. It was found by Petibon et al. that electrolytes with esters significantly improve with the addition of additives.[151] The increasing interest in using esters in Li-ion cell electrolytes comes with the desire for more transport data on these systems.

5.2 Pulsed field Gradient NMR

Pulsed field gradient NMR (PFG-NMR) is a two-dimensional (2D) NMR technique that has been used for the study of self-diffusion and transport of species in solution.[124] One-dimensional (1D) NMR indeed has two-dimensions (frequency vs intensity), the term 1D refers to single-frequency axes derived from the Fourier transformation. 2D NMR then refers to the two frequency axes seen on the spectrum. 2D NMR implies that there are multiple pulses in the operational sequence. Compared to electrochemical methods, NMR has the advantage of providing ion-specific information on transport properties.[148] Therefore, electrolytes with multiple components can be investigated.

PFG-NMR creates a linear magnetic field gradient along the length of the NMR tube, such that the field is slightly stronger at one end than the other.[152] Modern high field NMR spectrometers are equipped with hardware that can rapidly ramp up the magnetic field in any of the three orthogonal axes. PFG allows spatial resolution in NMR measurements and is the basis for all imaging.

The diffusion measurement used is diffusion-ordered spectroscopy (DOSY), which is a spin-echo technique.[126] Stejskal, and Tanner first described the Echo technique in 1965.[153] Figure 5.3 shows the basic principle around PFG where δ is the gradient width (pulse time) and Δ is the signal (diffusion) delay time.

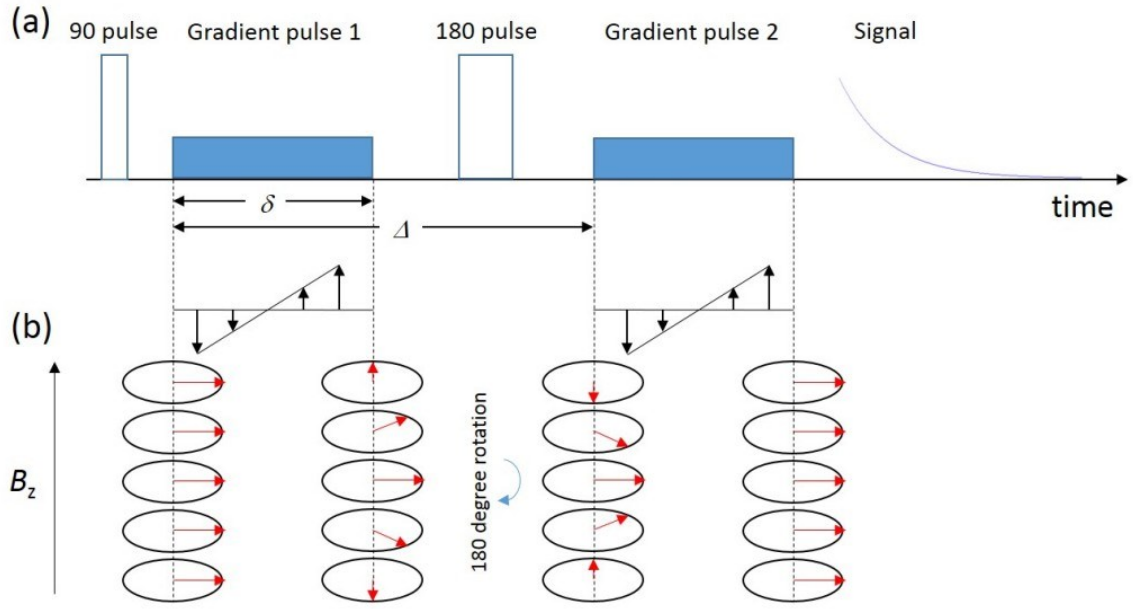

Figure 5.3 a) Schematic diagram of the PFG spin-echo pulse sequence. b) The phase evolution of the spins at different locations along the gradient direction.[154]

At the start of the sequence, the 90° pulse flips the spins into the X-Y plane, where spins begin to precess with their characteristic frequencies.[152] Next, the application of a gradient δ encodes a spatial component to the spin, providing a "snapshot" of the current positioning. Due to the gradient not being uniform, the precessional frequencies will change. At the end of the applied gradient, a magnetization helix is observed aligned to the z-axis. The second gradient applies an opposite dephasing to the magnetization, and the signal is restored to back to its original positioning. The 180° pulse that occurs between the two applied gradients at Δ/2 creates the "echo" by inverting the dispersed magnetization

such that once Δ is reached, the magnetization is negative of what it was following the first gradient pulse.[152] However, because the time before the second pulse (Δ) is when diffusion takes place, the "echo" will dampen out signals where the mean molecular displacement is on the order of the pitch of the magnetization helix. The resulting translational diffusion is based on the decay of the spin-echo signal or, in other words, the diffusion decay profile. Rapid diffusion rates result in rapid decay rates. The DOSY work done in this chapter uses PFG-simulated echoes to limit the chances of chemical shift changes and J-coupling evolution. The big difference is that instead of a 180° pulse, two 90° pulses are used.[152] Most DOSY pulse sequences used in the literature, and the sequence used in this work have additional pulses than the ones shown above that can manage gradient stabilization, fluid convection and artifact removal.

To obtain the diffusion coefficient for a specific signal, the same 2D experiments are done for a variety of magnetic field strengths. The resultant attenuation curve (intensity vs gradient-field strength) is fitted using the Stejskal-Tanner formula, Equation 5.2.[153]

$$I = I_o exp\left[-D[2\pi G_i \delta]^2 \frac{\Delta-\delta}{3}\right] \quad (5.2)$$

where D is the diffusion coefficient, I is the integrated intensity (resonance of the desired compound). I_0 is the intensity at a small gradient field strength. γ is the gyromagnetic ratio, G_i is the gradient strength, δ is the gradient width (pulse time) and Δ is the signal delay time. To perform the experiment, δ and Δ are optimized manually to ensure that the gradient ramp adequately digitizes the decay profile.

5.3 Experimental Methods

The electrolyte samples for the PFG-NMR experiments were prepared in an argon-filled glovebox (>0.1 ppm water content). Six samples were prepared in total, 0.1, 0.2, 0.5, 1.0, 2.0, and 3.0 m $LiPF_6$ in dimethyl carbonate (DMC) (purity 99.95%) and in methyl acetate (MA) (purity > 99.95%). Fluorinated ethylene propylene (FEP) tube liners (Aldrich) were used to house the electrolyte sample for the NMR experiments. Deuterated acetone (Aldrich) was added in between the glass NMR tube and the liner. Figure 5.4 shows an example of the set-up. The tops of the NMR samples were wrapped with parafilm to ensure limited electrolyte evaporation. All experiments were at 300.0 ± 0.1 K.

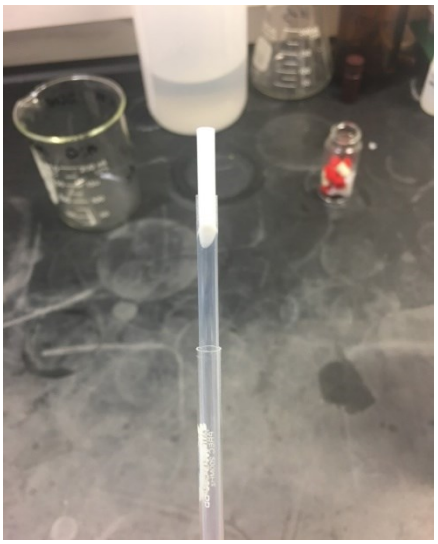

Figure 5.4 A picture of the liner-glass tube set-up.

^{7}Li and ^{19}F self-diffusivities were measured by using a double stimulated echo with a longitudinal eddy current delay pulse sequence along with bipolar pulse pairs. The time between gradient pulses Δ and the gradient pulse delay δ were optimized for each run. The strength of the field gradient (g) was increased in 16 equidistant steps for each sample. The maximum gradient strength reached for all samples was 32.35 G/cm. To obtain diffusivity

values, fits of the signal attenuation and the parameters of the pulse sequence were used with Stejskal's and Tanner's equation.[153] This calculation was performed by using the Bruker Topspin software 2.1.

5.4 Results

Figure 5.5 shows the diffusion constants calculated from the results of the DOSY experiments. Both the cation (Li^+) and anion (PF_6^-) results are shown for DMC and MA electrolytes for each salt concentration measured. The error bars seen for each diffusivity value were calculated based on the attenuation curve fit quality. Work from Krachkovskiy et al.[148] and Feng et al.[155] are included for comparison. It is generally known that diffusion rates of ions in solution are faster at low concentrations, due to the high degree of ionic dissociation and negligible ion pairing.[156] The results show that salt diffusion in MA is faster than in DMC and the EC-linear carbonate mixture. This is expected due to the conductivity of MA being high.[144] In the concentration range of 0.1−3.0 m, the diffusivity of Li^+ is nearly a factor of 2 higher in MA compared to DMC. The diffusivity of PF_6^- is also considerably higher in MA compared to DMC. This result is remarkable given the molecular similarity of these two solvents.

It is important to note that PFG-NMR is unable to differentiate between nuclei in neutral and charged aggregates.[148] This inability to differentiate will introduce error into the calculation of the transference number for a specific charged species. Solwijk et al.[157] suggested that diffusivity of free ions and neutral aggregates can be separated by additionally measuring specific conductivity (κ) of the solution. Then the charge diffusivity D_κ can be calculated via Equation 5.3.

$$D_\kappa = \frac{k_B T}{c_s e^2}\kappa \tag{5.3}$$

where k_B denotes the Boltzmann constant, T is temperature, e is the elementary charge, and c_s is the known total salt concentration (number density of molecules). However, in this work, specific conductivity was not measured; therefore the results seen may also have contributions from neutral aggregates.

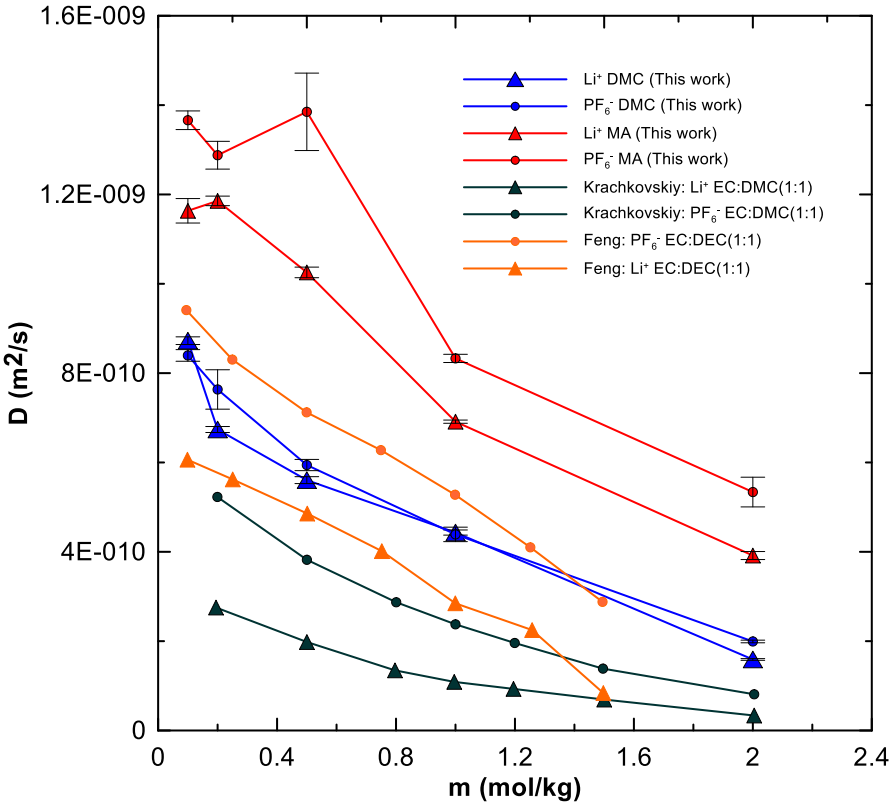

Figure 5.5 Lithium ion diffusion coefficients in $LiPF_6$ solutions in MA or DMC, measured by ^7Li and ^{19}F PFG-NMR as a function of salt concentration. All measurements were performed at 300K.[144] Work from Krachkovskiy et al.[148] also used PFG-NMR with EC: DMC(1:1) mixtures and is included in this figure also at 300K. Also, work from Feng et al.[155] used PFG-NMR on EC: DEC(1:1) mixtures and included in the figure at 300K.

Figure 5.5 also shows for each electrolyte tested that the diffusion coefficient for ^{19}F in PF^-_6 is higher than the diffusion coefficient for ^7Li in Li^+; the literature supports these findings .[147] Li^+ ions are preferentially solvated where more molecules are found in its

solvation shell compared to the bulker anion, resulting in slower diffusion rates for the cation.

As stated earlier, both diffusion constants and Li^+ transference numbers are essential properties to evaluating the performance of a Li-ion cell electrolyte. If it is assumed that the effective diffusivity of the neutral ionic aggregate is zero, then the diffusivity of charged species would be equal to their diffusion coefficients. [155] The sum of the ionic diffusivity can then be considered as the total charge diffusivity. The cation transference number (t^+), in this case, the Li^+ transference number, can then be calculated from the diffusion constants (Equation 5.4). It is essentially the fraction of the total ionic conductivity carried by the Li^+ cation.

$$Li\ t^+ = \frac{D_{Li^+}}{D_{Li^+} + D_{PF_6^-}} \tag{5.4}$$

Figure 5.6 shows the calculated Li^+ transference numbers with the error propagated from the diffusion coefficients. The results from Krachkovskiy et al.[148] and Feng et al.[155] are also included for comparison. It is desired to have Li^+ transference numbers that are as high as possible.[147] This would mitigate against the concentration profiles produced in cells and especially for scenarios of high-rate charging. Unfortunately, using high conductivity electrolytes does not always lead to high Li^+ transference numbers. Electrolytes with high conductivity and high Li^+ transference numbers are elusive due to the limitations of ion transport when the anion is immobilized.[147]

Figure 5.5 results show that the transference numbers found are higher than the values reported by Krachkovskiy et al[148] and Feng et al.[155], where similar transference numbers were measured in both DMC and MA (on the order of 0.4−0.5). However,

electrolytes in MA have a consistently lower transference number by a small margin. These electrolytes may be a benefit to high-rate charging applications. However, using them on their own would most likely lead to cell failure, as they would not be able to form a passivating layer on the negative electrode.[151]

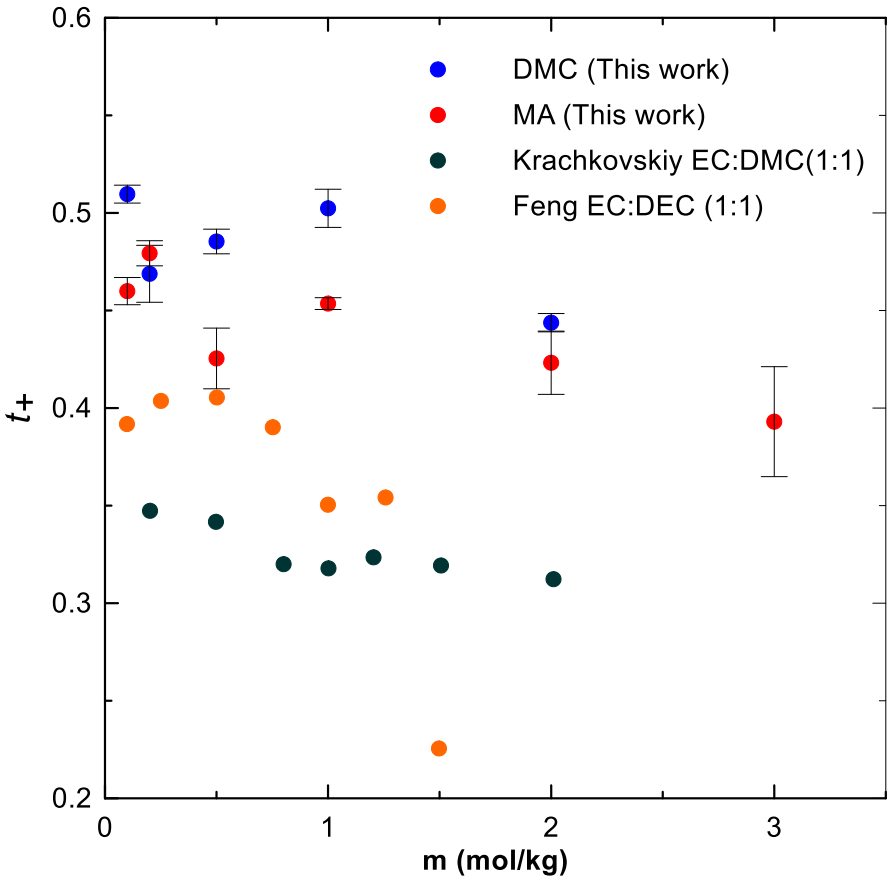

Figure 5.6 Li-ion transference number as calculated from PFG-NMR measurements for $LiPF_6$ in both DMC and MA as a function of salt concentration.[144] Work from Krachkovskiy et al.[148] and Feng et al.[155] is also included. All data is reported at 300K

5.5 Conclusions

Chapter 5 reports the results from PFG-NMR, DOSY experiments on Li-ion cell electrolytes. Electrolytes DMC and MA were compared for a variety of salt concentrations (0.1-3.0M). Diffusion coefficients of the cation (Li^+) and anion (PF_6^-) were reported and

found that MA had the highest reported rates when compared to the DMC and other results from the literature. For DMC and MA, the anion diffusion coefficient was higher than the cation. This work supports the use of MA as an electrolyte for possible fast-charging applications.[70,151,158] From the diffusion coefficients, the cation transference number is possible to calculate (ignoring ion-pairing effects). The results are reported, and DMC and MA were found to have very similar results (0.4-0.5).

CHAPTER 6 – CONCLUSIONS

6.1 Concluding Remarks

The Li-ion cell battery is a technology that has impacted the lives of most people in the world.[159] Their most common application is in the powering of many different consumer electronics. However, further work is needed to make them more affordable, safer, and longer-lasting. Hopefully, then Li-ion batteries can be more widely adopted into applications like electric vehicles and grid energy storage.

The results from this thesis show an electrolyte analysis method that can test a variety of electrolytes, especially for cells that have had cycled for an extended period. In addition, a method to measure diffusion constants of salt in electrolytes is described in this thesis and opens another avenue for fundamental electrolyte analysis.

The focus of this Thesis is the electrolyte, specifically understanding how the electrolyte changes in cells after a prolonged period of cycling. The importance of the electrolyte was outlined in Chapter 2, with an emphasis on how the electrolyte is the main contributor to a stable SEI.[160] A stable SEI layer is vital for a cell to have a long lifetime. The SEI can also be modified by additives to limit the reactions between the negative electrode and the electrolyte. The methods developed in Chapter 3 were used to investigate the degradation products that can possibly be produced.[60] Additionally, the method allows for further analysis of the electrodes.

The extraction method for cell electrolytes and sample preparation for analysis in NMR and GC-MS are described in Chapter 3. From one extraction, two different

measurements were made. NMR and GC-MS allowed for direct quantification of known electrolyte components in the extraction mixture while GC-MS additionally was used to identify possible degradation products present in the same mixture. It was found that the extraction solvent used (acetonitrile) did not affect the surface of the negative electrode. The negative electrodes were recovered for further analysis by μ-XRF.

Chapter 4 used the methods described in Chapter 3 to test cells with various combinations of the additives VC and DTD. In Chapter 4, it was found that the cells with 1VC or 2VC, and 1DTD had the best capacity retention and cycling performance. Electrolyte analysis of all the cells found no known degradation products (within the detection limits of the techniques used), but it was discovered that cells with 1% or 2% VC and 1% DTD had considerable salt consumption. The correlation between salt consumption in the electrolyte and cell cycling performance needs to be further investigated and verified. However, it may be an indication of some novel degradation mechanism brought on by using VC and DTD in a specific ratio. Analysis of the negative electrodes found small amounts of transition metal deposited on the surface, with little correlation to capacity losses seen in the cells tested. Therefore, it is expected that cells lost capacity due to thickening of the negative electrode SEI which consumes lithium inventory. The additive combination 1% or 2% VC and 1DTD is excellent for use in Li-ion cell electrolytes; however, further work is needed to understand the fundamental reasons why.

The work in Chapter 5 takes a different look at electrolytes and investigates their physical transport properties. A PFG-NMR technique was introduced to perform DOSY experiments that, when processed, provided the diffusion coefficients of various species in solution.[152] Further estimations can be made then to calculate Li-ion transference numbers.

In Chapter 5, the movement of the $LiPF_6$ cation and anion in either DMC or MA was investigated by DOSY. It was found that when salt is in MA, both the cation and anion had faster diffusion rates compared to the same salt in DMC. MA, thus, is a useful solvent to use in electrolyte formulations catered to high-rate charging. However, MA and DMC were found to be comparable when it comes to the calculated transference numbers, but together were higher when compared to values reported in the literature.[155,161] Obtaining physical constants such as diffusion coefficients are essential to researchers who use physics-based models to predict the suitability of an electrolyte in a cell. However, it is vital that the constants obtained are accurate to make these models mirror reality as much as possible.

6.2 Future work

The results of Chapter 4 inspired an experiment currently underway. To investigate why the additive combination 1% or 2% VC and 1% DTD performed so well. The same type of cells used in Chapter 4 were filled with the same electrolyte except that the only additive combination used 1%VC +1%DTD. The big experimental difference is that the cells are cycling at 70°C to promote the kinetics of possible electrolyte decomposition reactions. Cells will be taken off at different degrees of capacity loss, such as at 10% and 20%. The NMR and GC-MS method will be used to analyze the electrolyte from these cells. In addition, Li-ion differential thermal analysis (DTA) will be used also to estimate the concentration of each electrolyte component.[79] It is expected that the capacity loss would be connected to the state of the electrolyte. Keeping the cells identical allows for a thorough analysis of the electrolyte decomposition progression, if any. Significantly less dilution will be made before GC-MS and NMR experiments so that hopefully trace decomposition products can be detected. Additionally, the same electrolyte will be thermally aged in a

pouch bag (the same laminate material used to house the cells used in Chapter 4) for different lengths of time. This will be done to see how the electrolyte behaves in the absence of charged electrodes. Differences and similarities in the analysis can provide important mechanistic information.

To further understand the connection between the 1% or 2% VC and 1% DTD additive combination and the excessive salt consumption seen in cells with that combination, cells identical to that of Chapter 4 are filled with the 1%VC+ 1%DTD combination, but the concentration of $LiPF_6$ salt is varied. Electrolytes with 0.2M, 0.6M, 1.5M and 2M concentrations of salt will be compared to see the degree of consumption after a period of cycling at room temperature. Lower salt concentrations will inevitably lead to cell failure due to the electrolyte not being as conductive.[39] However, doing an experiment like this will put a spotlight on any mechanisms that the additive combination has with the $LiPF_6$ salt.

The methods described in Chapter 3 will be further improved. Currently, the pure electrolyte from a cell goes through two dilutions using acetonitrile. The initial one happens within the cell, followed by the subsequent dilution using a 10.0ml volumetric flask. The large dilutions may prevent some decomposition products from being detected in the GC-MS as their concentration would be too low. Therefore, using a 5.0 ml volumetric flask (or less) perhaps could be a solution. An additional benefit to reducing the dilution factors will be to minimize solvent use per cell, keeping in line with green chemistry principles.[162]

Future work can use the methods discussed in Chapter 3 to investigate different electrolytes with different additive systems. Chapter 4 describes an electrolyte using three different carbonates, two different additives and one type of salt. However, many more

combinations are possible. Frequently, a new additive is introduced to Li-ion cells and often it is unknown how it may behave in the cell and how it compares to an established additive(s). The only way to find out is to test it in a systematic way as was done in Chapter 4. In addition, several reports have mentioned using various salts in electrolyte formulations.[163,164] It is essential when studying electrolyte systems that only one variable is changed in a matrix of cells. That way, changes seen can be attributed to that single alteration. Some notable additives to study in the future include $LiPO_2F_2$ (salt), fluoroethylene carbonate, and other fluorophosphate complexes like lithium tris(oxalate)phosphate (LiTFOP).[70,144]

Another area of work to focus on in the future will be to develop a method to identify and quantify the components of the SEI formed on the negative electrode surface. It will be interesting to measure components such as LiF, Li_2CO_3 and other inorganic SEI components.[18] It has been shown in Chapter 3 that acetonitrile does not dissolve inorganic components. Therefore, it is a possibility that after the electrolyte analysis method is complete, the negative electrode from cells can go through additional analysis. This is akin to the μ-XRF measurements performed. The method by Schwenke et al.[94] has been shown to be suitable for SEI analysis; the method has also been described in Chapter 3. However, improvements to this method can be made to ensure that the internal standards used are stable. Another option is to develop the NMR method to have an external standard. It is also worth investigating the conflicting reports of whether LEDC or LEMC is present in Li-ion cell SEIs. The work done by Schwenke et al.[94] shows a significant amount of LEDC in their SEI analysis and no LEMC. This must be verified given the significant claims that Wang et al.[29] made describing that LEMC is the primary component. LEMC has been

described to go through rapid hydrolysis to form LEDC. The method by Schwenke et al.[94] must be altered to avoid any hydrolysis reactions. This could be done by possibly not using D_2O to dissolve the SEI components and using dimethyl sulfoxide instead as it has a high dielectric constant.

Future work will also involve the use of a novel low-field benchtop NMR system which is being purchased now with NSERC RTI funding. These systems use permanent magnetics that range from 40MHz to 100 MHz in size.[165] The systems are calibrated to 2-3 nuclei and require no deuterated solvents. The system is also easily transportable. No liquid helium cooling is needed making the technique a lot greener compared to traditional high-field systems. In addition, the benchtop system can make quantitative work more streamlined, and economical.

Work done in Chapter 5, looking at the salt diffusion in MA and DMC, can be expanded to several other electrolyte systems. It will be important to collect data on established electrolyte systems currently used in commercial cells. These include different concentrations of $LiPF_6$ in EC mixed with one or more linear carbonates. Examples include EC:EMC:DMC (25:5:70 v:v:v) and EC:EMC (3:7 v:v). Additionally, MA will be investigated further through the addition of co-solvents such as FEC. Currently underway are diffusion measurements of "anode-free" electrolyte systems.[166] These are often dual salt systems, with one example containing lithium difluoro(oxalate)borate (LiDFOB) and lithium tetrafluoroborate ($LiBF_4$) in FEC:DEC (1:2 v:v). These electrolyte systems were created for lithium metal cycling. The diffusion data has not been reported before for these novel electrolyte systems and could be useful to the future development of lithium metal cells. However, as stated in Chapter 5, NMR cannot differentiate between neutral and

charged species. Therefore, future work will need to be combined with direct conductivity measurements to differentiate the charged and neutral species. This will also improve the accuracy of calculated transference numbers.

Recently, a novel DOSY method was created to probe the solution structure of Li-ion cell electrolytes.[167] It is a DOSY method that uses an internal standard, toluene, which has a negligible coordinating ability to the electrolyte. It can be used to determine the solvation state and average solvation number of electrolyte solvents. In addition, it is possible to see viscosity changes. Typically, vibrational spectroscopy is used for this purpose but due to so many electrolyte compounds having similar functional groups it can be difficult to interpret vibrational spectra.[168] Future work will explore using DOSY-NMR as an experiment to obtain a larger range of physiochemical properties of modern electrolytes.

REFERENCES

(1) Marris, E. Why Young Climate Activists Have Captured the World's Attention. *Nature*. NLM (Medline) September 1, 2019, pp 471–472.

(2) BBC. Who is Greta Thunberg, the teenage climate change activist ? https://www.bbc.com/news/world-europe-49918719 (accessed Jun 12, 2020).

(3) Drew, R. Canadian Indigenous water activist Autumn Peltier addresses UN on clean water | CBC News https://www.cbc.ca/news/world/canadian-indigenous-water-activist-autumn-peltier-addresses-un-on-clean-water-1.5301559 (accessed Jun 12, 2020).

(4) Klein, J. A.; Yeh, E.; Bump, J.; Nyima, Y.; Hopping, K. Coordinating Environmental Protection and Climate Change Adaptation Policy in Resource-Dependent Communities: A Case Study from the Tibetan Plateau. *Adv. Glob. Chang. Res.* **2011**, *42*, 423–438.

(5) Mulvaney, K. World climate change report card: These countries are meeting goals https://www.nationalgeographic.com/environment/2019/09/climate-change-report-card-co2-emissions/ (accessed Jun 12, 2020).

(6) Rinscheid, A.; Pianta, S.; Weber, E. U. Fast Track or Slo-Mo? Public Support and Temporal Preferences for Phasing out Fossil Fuel Cars in the United States. *Clim. Policy* **2020**, *20*, 30–45.

(7) Center for Climate and Energy Solutions. Global Emissions: Center for climate and energy solutions https://www3.epa.gov/climatechange/ghgemissions/gwps.html (accessed Jun 13, 2020).

(8) Coren, M. J. Nine countries say they'll ban internal combustion engines. So far, it's just words https://qz.com/1341155/nine-countries-say-they-will-ban-internal-combustion-engines-none-have-a-law-to-do-so/ (accessed Jun 13, 2020).

(9) Zeng, X.; Li, M.; Abd El-Hady, D.; Alshitari, W.; Al-Bogami, A. S.; Lu, J.; Amine, K. Commercialization of Lithium Battery Technologies for Electric Vehicles. *Adv. Energy Mater.* **2019**, *9* (27), 1–25.

(10) Lithium-ion Battery Market Size and Share | Industry Analysis by 2027 https://www.alliedmarketresearch.com/lithium-ion-battery-market (accessed Jun 13, 2020).

(11) Micromeritics Instrument Corporation. Zeta Potential Analysis of Lithium Ion Battery Electrolytes https://www.azom.com/article.aspx?ArticleID=14584 (accessed Jun 19, 2020).

(12) Oliveira, L.; Messagie, M.; Rangaraju, S.; Sanfelix, J.; Hernandez Rivas, M.; Van Mierlo, J. Key Issues of Lithium-Ion Batteries - From Resource Depletion to Environmental Performance Indicators. *J. Clean. Prod.* **2015**, *108*, 354–362.

(13) Nazari, A.; Farhad, S. Heat Generation in Lithium-Ion Batteries with Different Nominal Capacities and Chemistries. *Appl. Therm. Eng.* **2017**, *125*, 1501–1517.

(14) Noh, H.-J.; Youn, S.; Yoon, C. S.; Sun, Y.-K. Comparison of the Structural and Electrochemical Properties of Layered $Li[Ni_xCo_yMn_z]O_2$ (x = 1/3, 0.5, 0.6, 0.7, 0.8 and 0.85) Cathode Material for Lithium-Ion Batteries. *J. Power Sources* **2013**, *233*, 121–130.

(15) Aurbach, D.; Talyosef, Y.; Markovsky, B.; Markevich, E.; Zinigrad, E.; Asraf, L.; Gnanaraj, J. S.; Kim, H.-J. Design of Electrolyte Solutions for Li and Li-Ion Batteries: A Review. *Electrochim. Acta* **2004**, *50*, 247–254.

(16) Xing, L.; Zheng, X.; Schroeder, M.; Alvarado, J.; Von, A.; Cresce, W.; Xu, K.; Li, Q.; Li, W. Deciphering the Ethylene Carbonate−Propylene Carbonate Mystery in Li-Ion Batteries. *Acc. Chem. Res* **2018**, *51*, 282-289 .

(17) Cai, W.; Yao, Y.-X.; Zhu, G.-L.; Yan, C.; J-iang, L.-L.; He, C.; Huang, J.-Q.; Zhang, Q. A Review on Energy Chemistry of Fast-Charging Anodes. *Chem. Soc. Rev.* **2020**, *49*, 3806-3833.

(18) Wang, A.; Kadam, S.; Li, H.; Shi, S.; Qi, Y. Review on Modeling of the Anode Solid Electrolyte Interphase (SEI) for Lithium-Ion Batteries. *npj Comput. Mater.* **2018**, *4*, 1-25.

(19) Yoshida, H.; Fukunaga, T.; Hazama, T.; Terasaki, M.; Mizutani, M.; Yamachi, M. Degradation Mechanism of Alkyl Carbonate Solvents Used in Lithium-Ion Cells during Initial Charging. *J. Power Sources* **1997**, *68* (2), 311–315.

(20) Qian, Y.; Hu, S.; Zou, X.; Deng, Z.; Xu, Y.; Cao, Z.; Kang, Y.; Deng, Y.; Shi, Q.; Xu, K.; Deng, Y. How Electrolyte Additives Work in Li-Ion Batteries. *Energy Storage Mater.* **2019**, *20*, 208–215.

(21) Kang, Y.; Wang, J.; Du, L.; Liu, Z.; Zou, X.; Tang, X.; Cao, Z.; Wang, C.; Xiong, D.; Shi, Q.; Qian, Y.; Deng, Y. Overcharge Investigations of $LiCoO_2$/Graphite Lithium Ion Batteries with Different Electrolytes. *ACS Appl. Energy Mater.* **2019**, *2*, 8615–8624.

(22) Peled, E. The Electrochemical Behavior of Alkali and Alkaline Earth Metals in Nonaqueous Battery Systems—The Solid Electrolyte Interphase Model. *J. Electrochem. Soc.* **1979**, *126*, 2047.

(23) Peled, E. Advanced Model for Solid Electrolyte Interphase Electrodes in Liquid and Polymer Electrolytes. *J. Electrochem. Soc.* **1997**, *144*, L208.

(24) Malmgren, S.; Ciosek, K.; Hahlin, M.; Gustafsson, T.; Gorgoi, M.; Rensmo, H.; Edström, K. Electrochimica Acta Comparing Anode and Cathode Electrode/Electrolyte Interface Composition and Morphology Using Soft and Hard X-Ray Photoelectron Spectroscopy. *Electrochim. Acta* **2013**, *97*, 23–32.

(25) Meyer, B. M.; Leifer, N.; Sakamoto, S.; Greenbaum, S. G.; Grey, C. P. High Field Multinuclear NMR Investigation of the SEI Layer in Lithium Rechargeable Batteries. *Electrochem. Solid-State Lett.* **2005**, *8*, A145-A148.

(26) Zhuang, G. V.; Ross, P. N. Analysis of the Chemical Composition of the Passive Film on Li-Ion Battery Anodes Using Attentuated Total Reflection Infrared Spectroscopy. *Electrochem. Solid-State Lett.* **2003**, *6,* A136-A139.

(27) Edström, K.; Herstedt, M.; Abraham, D. P.; Angström. A New Look at the Solid Electrolyte Interphase on Graphite Anodes in Li-Ion Batteries. *J. Power Sources* **2006**, *153*, 380–384.

(28) Nie, M.; Chalasani, D.; Abraham, D. P.; Chen, Y.; Bose, A.; Lucht, B. L. Lithium Ion Battery Graphite Solid Electrolyte Interphase Revealed by Microscopy and Spectroscopy. *J. Phys. Chem. C* **2013**, *117*, 1257–1267.

(29) Wang, L.; Menakath, A.; Han, F.; Wang, Y.; Zavalij, P. Y.; Gaskell, K. J.; Borodin, O.; Iuga, D.; Brown, S. P.; Wang, C.; Xu, K.; Eichhorn, B. W. Identifying the Components of the Solid–Electrolyte Interphase in Li-Ion Batteries. *Nat. Chem.* **2019**, *11*, 789–796.

(30) Madec, L.; Petibon, R.; Tasaki, K.; Xia, J.; Sun, J. P.; Hill, I. G.; Dahn, J. R. Mechanism of Action of Ethylene Sulfite and Vinylene Carbonate Electrolyte Additives in $LiNi_{1/3}Mn_{1/3}Co_{1/3}O_2$/Graphite Pouch Cells: Electrochemical, GC-MS and XPS Analysis. *Phys. Chem. Chem. Phys.* **2015**, *17*, 27062–27076.

(31) Balasubramanian, M.; Lee, H. S.; Sun, X.; Yang, X. Q.; Moodenbaugh, A. R.; McBreen, J.; Fischer, D. A.; Fu, Z. Formation of SEI on Cycled Lithium-Ion Battery Cathodes Soft X-Ray Absorption Study. *Electrochem. Solid-State Lett.* **2002**, *5*, A22-A25.

(32) Menkin, S.; Golodnitsky, D.; Peled, E. Artificial Solid-Electrolyte Interphase (SEI) for Improved Cycleability and Safety of Lithium-Ion Cells for EV Applications. *Electrochem. commun.* **2009**, *11*, 1789–1791.

(33) Ramasubramanian, A.; Yurkiv, V.; Foroozan, T.; Ragone, M.; Shahbazian-Yassar, R.; Mashayek, F. Lithium Diffusion Mechanism through Solid-Electrolyte Interphase in Rechargeable Lithium Batteries. *J. Phys. Chem. C* **2019**, *123*, 10237–10245.

(34) Malmgren, S.; Ciosek, K.; Hahlin, M.; Gustafsson, T.; Gorgoi, M.; Rensmo, H.; Edström, K. Comparing Anode and Cathode Electrode/Electrolyte Interface Composition and Morphology Using Soft and Hard X-Ray Photoelectron Spectroscopy. *Electrochim. Acta* **2013**, *97*, 23–32.

(35) Han, X.; Sun, J.; Li, R.; Chemcomm; Communication, C. Design of a LiF-Rich Solid Electrolyte Interface Layer through Salt-Additive Chemistry for Boosting Fast-Charging Phosphorus-Based Lithium Ion Battery Performance. *Chem. Commun* **2020**, *56*, 6047–6049.

(36) Bhattacharya, S.; Riahi, A. R.; Alpas, A. T. Electrochemical Cycling Behaviour of Lithium Carbonate (Li_2CO_3) Pre-Treated Graphite Anodes - SEI Formation and Graphite Damage Mechanisms. *Carbon N. Y.* **2014**, *77*, 99–112.

(37) Xu, K. Nonaqueous Liquid Electrolytes for Lithium-Based Rechargeable Batteries. *Chem. Rev.* **2004**, *104*, 4303–4417.

(38) Goodenough, J. B.; Kim, Y. Challenges for Rech argeable Li Batteries. *Chem. Mater.* **2010**, *22*, 587–603.

(39) Logan, E. R.; Tonita, E. M.; Gering, K. L.; Li, J.; Ma, X.; Beaulieu, L. Y.; Dahn, J. R. A Study of the Physical Properties of Li-Ion Battery Electrolytes Containing Esters. *J. Electrochem. Soc.* **2018**, *165*, 21–30.

(40) Winter, M.; Barnett, B.; Xu, K. Before Li Ion Batteries. *Chem. Rev.* **2018**, *118*, 11433–11456.

(41) Fong, R.; Von Sacken, U.; Dahn, J. Studies of Lithium Intercalation into Carbons Using Nonaqueous Electrochemical Cells. *J. Electrochem. Soc.* **1990**, *137*, 2009-2013.

(42) Xu, K. Electrolytes and Interphases in Li-Ion Batteries and Beyond. *Chem. Rev.* **2014**, *114*, 11503–11618.

(43) Xu, K. Toward Reliable Values of Electrochemical Stability Limits for Electrolytes. *J. Electrochem.* **1999**, *146*, 4172-4178.

(44) Nanjundiah, C. Electrochemical Stability of $LiMF_6$ (M = P, As, Sb) in Tetrahydrofuran and Sulfolane. *J. Electrochem. Soc.* **1988**, *135*, 2914-2917.

(45) Ishikawa, M.; Sugimoto, T.; Kikuta, M.; Ishiko, E.; Kono, M. Pure Ionic Liquid Electrolytes Compatible with a Graphitized Carbon Negative Electrode in Rechargeable Lithium-Ion Batteries. *J. Power Sources* **2006**, *162*, 658–662.

(46) Sloop, S. E.; Pugh, J. K.; Wang, S.; Kerr, J. B.; Kinoshita, K. Chemical Reactivity of PF_5 and $LiPF_6$ in Ethylene Carbonate/Dimethyl Carbonate Solutions. *Electrochem. Solid-State Lett.* **2001**, *4*, A42-A44.

(47) Logan, E. R.; Tonita, E. M.; Gering, K. L.; Ma, L.; Bauer, M. K. G.; Li, J.; Beaulieu, L. Y.; Dahn, J. R. A Study of the Transport Properties of Ethylene Carbonate-Free Li Electrolytes. *J. Electrochem. Soc.* **2018**, *165*, 705–716.

(48) Ding, M. S.; Xu, K.; Zhang, S. S.; Amine, K.; Henriksen, G. L.; Jow, T. R. Change of Conductivity with Salt Content, Solvent Composition, and Temperature for Electrolytes of $LiPF_6$ in Ethylene Carbonate-Ethyl Methyl Carbonate. *J. Electrochem. Soc.* **2001**, *148*, A1196-A1204.

(49) Peled, E.; Menkin, S. Review-SEI: Past, Present and Future. *J. Electrochem. Soc.* **2017**, *164*, 1703–1719.

(50) Krause, L. J.; Chevrier, V. L.; Jensen, L. D.; Brandt, T. The Effect of Carbon Dioxide on the Cycle Life and Electrolyte Stability of Li-Ion Full Cells Containing Silicon Alloy. *J. Electrochem. Soc.* **2017**, *164*, 2527–2533.

(51) Campion, C. L.; Li, W.; Lucht, B. L. Thermal Decomposition of $LiPF_6$-Based Electrolytes for Lithium-Ion Batteries. *J. Electrochem. Soc.* **2005**, *152*, A2327-A2334.

(52) Ma, L.; Glazier, S. L.; Petibon, R.; Xia, J.; Peters, J. M.; Liu, Q.; Allen, J.; Doig, R. N. C.; Dahn, J. R. A Guide to Ethylene Carbonate-Free Electrolyte Making for Li-Ion Cells. *J. Electrochem. Soc.* **2017**, *164*, A5008–A5018.

(53) Borodin, O.; Smith, G. D.; Fan, P. Molecular Dynamics Simulations of Lithium Alkyl Carbonates. *J. Phys. Chem. B* **2006**, *110*, 22773–22779.

(54) Freunberger, S. A. Interphase Identity Crisis. *Nat. Chem.* **2019**, *11*, 761–763.

(55) Yang, C. R.; Wang, Y. Y.; Wan, C. C. Composition Analysis of the Passive Film on the Carbon Electrode of a Lithium-Ion Battery with an EC-Based Electrolyte. *J. Power Sources* **1998**, *72*, 66–70.

(56) Strehle, B.; Solchenbach, S.; Metzger, M.; Schwenke, K. U.; Gasteiger, H. A. The Effect of CO_2 on Alkyl Carbonate Trans-Esterification during Formation of Graphite Electrodes in Li-Ion Batteries . *J. Electrochem. Soc.* **2017**, *164*, A2513–A2526.

(57) Verma, P.; Maire, P.; Novák, P. A Review of the Features and Analyses of the Solid Electrolyte Interphase in Li-Ion Batteries. *Electrochim. Acta* **2010**, *55*, 6332–6341.

(58) Nie, M.; Chalasani, D.; Abraham, D. P.; Chen, Y.; Bose, A.; Lucht, B. L. Lithium Ion Battery Graphite Solid Electrolyte Interphase Revealed by Microscopy and Spectroscopy. *J. Phys. Chem. C* **2013**, *117*, 1257–1267.

(59) Sasaki, T.; Abe, T.; Iriyama, Y.; Inaba, M.; Ogumi, Z. Formation Mechanism of Alkyl Dicarbonates in Li-Ion Cells. *J. Power Sources* **2005**, *150*, 208–215.

(60) Thompson, L. M.; Stone, W.; Eldesoky, A.; Smith, N. K.; McFarlane, C. R. M.; Kim, J. S.; Johnson, M. B.; Petibon, R.; Dahn, J. R. Quantifying Changes to the Electrolyte and Negative Electrode in Aged NMC532/Graphite Lithium-Ion Cells. *J. Electrochem. Soc.* **2018**, *165*, A2732–A2740.

(61) Takeuchi, E. S. Anode Passivation and Electrolyte Solvent Disproportionation: Mechanism of Ester Exchange Reaction in Lithium-Ion Batteries. *J. Electrochem. Soc.* **1997**, *144*, 1944-1951.

(62) Kim, H.; Grugeon, S.; Gachot, G.; Armand, M.; Sannier, L.; Laruelle, S. Ethylene Bis-Carbonates as Telltales of SEI and Electrolyte Health, Role of Carbonate Type and New Additives. *Electrochim. Acta* **2014**, *136*, 157–165.

(63) Petibon, R.; Rotermund, L.; Nelson, K. J.; Gozdz, A. S.; Xia, J.; Dahn, J. R. Study of Electrolyte Components in Li Ion Cells Using Liquid-Liquid Extraction and Gas Chromatography Coupled with Mass Spectrometry. *J. Electrochem. Soc.* **2014**, *161*, A1167–A1172.

(64) Rinkel, B. L. D.; Hall, D. S.; Temprano, I.; Grey, C. P. Electrolyte Oxidation Pathways in Lithium-Ion Batteries. *ChemRxiv* **2020**.Preprint.

(65) Gachot, G.; Ribière, P.; Mathiron, D.; Grugeon, S.; Armand, M.; Leriche, J. B.; Pilard, S.; Laruelle, S. Gas Chromatography/Mass Spectrometry as a Suitable Tool for the Li-Ion Battery Electrolyte Degradation Mechanisms Study. *Anal. Chem.* **2011**, *83*, 478–485.

(66) Grützke, M.; Kraft, V.; Weber, W.; Wendt, C.; Friesen, A.; Klamor, S.; Winter, M.; Nowak, S. Supercritical Carbon Dioxide Extraction of Lithium-Ion Battery Electrolytes. *J. Supercrit. Fluids* **2014**, *94*, 216–222.

(67) Sasaki, T.; Abe, T.; Iriyama, Y.; Inaba, M.; Ogumi, Z. Suppression of an Alkyl Dicarbonate Formation in Li-Ion Cells. *J. Electrochem. Soc.* **2005**, *152*, A2046.

(68) Sasaki, T.; Abe, T.; Iriyama, Y.; Inaba, M.; Ogumi, Z. Formation Mechanism of Alkyl Dicarbonates in Li-Ion Cells. *J. Power Sources* **2005**, *150*, 208–215.

(69) Peng, H.-J.; Urbonaite, S.; Villevieille, C.; Wolf, H.; Leitner, K.; Novák, P. Consequences of Electrolyte Degradation for the Electrochemical Performance of $Li_{1+x}(Ni_aCo_bMn_{1-a-b})_{1-x}O_2$. *J. Electrochem. Soc.* **2015**, *162*, A7072–A7077.

(70) Harlow, J. E.; Ma, X.; Li, J.; Logan, E.; Liu, Y.; Zhang, N.; Ma, L.; Glazier, S. L.; Cormier, M. M. E.; Genovese, M.; Buteau, S.; Cameron, A.; Stark, J. E.; Dahn, J. R. A Wide Range of Testing Results on an Excellent Lithium-Ion Cell Chemistry to Be Used as Benchmarks for New Battery Technologies. *J. Electrochem. Soc.* **2019**, *166*, A3031–A3044.

(71) Petibon, R.; Chevrier, V. L.; Aiken, C. P.; Hall, D. S.; Hyatt, S. R.; Shunmugasundaram, R.; Dahn, J. R. Studies of the Capacity Fade Mechanisms of $LiCoO_2$ /Si-Alloy: Graphite Cells . *J. Electrochem. Soc.* **2016**, *163*, A1146–A1156.

(72) Christe, K. O.; Dixon, D. A.; McLemore, D.; Wilson, W. W.; Sheehy, J. A.; Boatz, J. A. On a Quantitative Scale for Lewis Acidity and Recent Progress in Polynitrogen Chemistry. *J. Fluor. Chem.* **2000**, *101*, 151–153.

(73) Kawamura, T.; Okada, S.; Yamaki, J. ichi. Decomposition Reaction of $LiPF_6$-Based Electrolytes for Lithium Ion Cells. *J. Power Sources* **2006**, *156*, 547–554.

(74) Aurbach, D.; Markovsky, B.; Salitra, G.; Markevich, E.; Talyossef, Y.; Koltypin, M.; Nazar, L.; Ellis, B.; Kovacheva, D. Review on Electrode-Electrolyte Solution Interactions, Related to Cathode Materials for Li-Ion Batteries. *J. Power Sources* **2007**, *165*, 491–499.

(75) Wilken, S.; Treskow, M.; Scheers, J.; Johansson, P.; Jacobsson, P. Initial Stages of Thermal Decomposition of $LiPF_6$-Based Lithium Ion Battery Electrolytes by Detailed Raman and NMR Spectroscopy. *RSC Adv.* **2013**, *3*, 16359–16364.

(76) Li, W.; Lucht, B. L. Inhibition of the Detrimental Effects of Water Impurities in Lithium-Ion Batteries. *Electrochem. Solid-State Lett.* **2007**, *10*, 115-118.

(77) Sloop, S. E.; Kerr, J. B.; Kinoshita, K. The Role of Li-Ion Battery Electrolyte Reactivity in Performance Decline and Self-Discharge. *J. Power Sources* **2003**, *119–121*, 330–337.

(78) Han, J. G.; Jeong, M. Y.; Kim, K.; Park, C.; Sung, C. H.; Bak, D. W.; Kim, K. H.; Jeong, K. M.; Choi, N. S. An Electrolyte Additive Capable of Scavenging HF and PF5 Enables Fast Charging of Lithium-Ion Batteries in $LiPF_6$-Based Electrolytes. *J. Power Sources* **2020**, *446*, 1–9.

(79) Day, R. P.; Xia, J.; Petibon, R.; Rucska, J.; Wang, H.; Wright, A. T. B.; Dahn, J. R. Differential Thermal Analysis of Li-Ion Cells as an Effective Probe of Liquid Electrolyte Evolution during Aging. *J. Electrochem. Soc.* **2015**, *162*, A2577–A2581.

(80) Andersson, A. M.; Edström, K. Chemical Composition and Morphology of the Elevated Temperature SEI on Graphite. *J. Electrochem. Soc.* **2001**, *148*, A1100-A1109.

(81) Harris, O. C.; Lee, S. E.; Lees, C.; Tang, M. Review: Mechanisms and Consequences of Chemical Cross-Talk in Advanced Li-Ion Batteries. *J.Phys Energy* **2020,** 032002.

(82) Joshi, T.; Eom, K.; Yushin, G.; Fuller, T. F. Effects of Dissolved Transition Metals on the Electrochemical Performance and SEI Growth in Lithium-Ion Batteries. *J. Electrochem. Soc.* **2014**, *161*, A1915–A1921.

(83) Li, Y.; Bettge, M.; Polzin, B.; Zhu, Y.; Balasubramanian, M.; Abraham, D. P. Understanding Long-Term Cycling Performance of $Li_{1.2}Ni_{0.15}Mn_{0.55}Co_{0.1}O_2$–Graphite Lithium-Ion Cells . *J. Electrochem. Soc.* **2013**, *160*, A3006–A3019.

(84) Ziv, B.; Borgel, V.; Aurbach, D.; Kim, J.-H.; Xiao, X.; Powell, B. R. Investigation of the Reasons for Capacity Fading in Li-Ion Battery Cells. *J. Electrochem. Soc.* **2014**, *161*, A1672–A1680.

(85) Abraham, D. P.; Spila, T.; Furczon, M. M.; Sammann, E. Evidence of Transition-Metal Accumulation on Aged Graphite Anodes by SIMS. *Electrochem. Solid-State Lett.* **2008**, *11*, 226–229.

(86) Gowda, S. R.; Gallagher, K. G.; Croy, J. R.; Bettge, M.; Thackeray, M. M.; Balasubramanian, M. Oxidation State of Cross-over Manganese Species on the Graphite Electrode of Lithium-Ion Cells. *Phys. Chem. Chem. Phys.* **2014**, *16*, 6898–6902.

(87) Xiong, D. J.; Ellis, L. D.; Petibon, R.; Hynes, T.; Liu, Q. Q.; Dahn, J. R. Studies of Gas Generation, Gas Consumption and Impedance Growth in Li-Ion Cells with Carbonate or Fluorinated Electrolytes Using the Pouch Bag Method. *J. Electrochem. Soc.* **2017**, *164*, 340–347.

(88) Jung, R.; Metzger, M.; Maglia, F.; Stinner, C.; Gasteiger, H. A. Chemical versus Electrochemical Electrolyte Oxidation on NMC111, NMC622, NMC811, LNMO, and Conductive Carbon. *J. Phys. Chem. Lett.* **2017**, *8*, 4820–4825.

(89) Renfrew, S. E.; McCloskey, B. D. Residual Lithium Carbonate Predominantly Accounts for First Cycle CO_2 and CO Outgassing of Li-Stoichiometric and Li-Rich Layered Transition-Metal Oxides. *J. Am. Chem. Soc.* **2017**, *139*, 17853–17860.

(90) Jung, R.; Metzger, M.; Maglia, F.; Stinner, C.; Gasteiger, H. A. Oxygen Release and Its Effect on the Cycling Stability of $LiNi_xMn_yCo_zO_2$ (NMC) Cathode Materials for Li-Ion Batteries . *J. Electrochem. Soc.* **2017**, *164*, A1361–A1377.

(91) Metzger, M.; Sicklinger, J.; Haering, D.; Kavakli, C.; Stinner, C.; Marino, C.; Gasteiger, H. A. Carbon Coating Stability on High-Voltage Cathode Materials in H_2O-Free and H_2O-Containing Electrolyte . *J. Electrochem. Soc.* **2015**, *162*, A1227–A1235.

(92) Plichta, E.; S., S.; Uchiyama, M.; Salomon, M.; Chua, D.; Ebner, W. B.; Lin, H. W. An Improved Li/Li_xCoO_2 Rechargeable Cell. *J. Electrochem. Soc.* **1989**, *136*, 1865-1869.

(93) Kang, S. H.; Abraham, D. P.; Xiao, A.; Lucht, B. L. Investigating the Solid Electrolyte Interphase Using Binder-Free Graphite Electrodes. *J. Power Sources* **2008**, *175*, 526–532.

(94) Schwenke, K. U.; Solchenbach, S.; Demeaux, J.; Lucht, B. L.; Gasteiger, H. A. The Impact of CO_2 Evolved from VC and FEC during Formation of Graphite Anodes in Lithium-Ion Batteries. *J. Electrochem. Soc.* **2019**, *166*, A2035–A2047.

(95) Guéguen, A.; Streich, D.; He, M.; Mendez, M.; Chesneau, F. F.; Novák, P.; Berg, E. J. Decomposition of $LiPF_6$ in High Energy Lithium-Ion Batteries Studied with Online Electrochemical Mass Spectrometry . *J. Electrochem. Soc.* **2016**, *163*, A1095–A1100.

(96) Sahore, R.; Dogan, F.; Bloom, I. D. Identification of Electrolyte-Soluble Organic Cross-Talk Species in a Lithium-Ion Battery via a Two-Compartment Cell. *Chem. Mater.* **2019**, *31*, 2884–2891.

(97) Gilbert, J. A.; Shkrob, I. A.; Abraham, D. P. Transition Metal Dissolution, Ion Migration, Electrocatalytic Reduction and Capacity Loss in Lithium-Ion Full Cells. *J. Electrochem. Soc.* **2017**, *164*, A389–A399.

(98) Tarascon, J. M. Synthesis Conditions and Oxygen Stoichiometry Effects on Li Insertion into the Spinel $LiMn_2O_4$. *J. Electrochem. Soc.* **1994**, *141*, 1421-1431.

(99) Solchenbach, S.; Hong, G.; Freiberg, A. T. S.; Jung, R.; Gasteiger, H. A. Electrolyte and SEI Decomposition Reactions of Transition Metal Ions Investigated by On-Line Electrochemical Mass Spectrometry. *J. Electrochem. Soc.* **2018**, *165*, A3304–A3312.

(100) Shin, H.; Park, J.; Sastry, A. M.; Lu, W. Degradation of the Solid Electrolyte Interphase Induced by the Deposition of Manganese Ions. *J. Power Sources* **2015**, *284*, 416–427.

(101) Ochida, M.; Domi, Y.; Doi, T.; Tsubouchi, S.; Nakagawa, H.; Yamanaka, T.; Abe,

T.; Ogumi, Z. Influence of Manganese Dissolution on the Degradation of Surface Films on Edge Plane Graphite Negative-Electrodes in Lithium-Ion Batteries. *J. Electrochem. Soc.* **2012**, *159*, A961–A966.

(102) Blyr, A.; Du Pasquier, A.; Amatucci, G.; Tarascon, J. M. Origin of Self-Discharge Mechanism in $LiMn_2O_4$-Based Li-Ion Cells: A Chemical and Electrochemical Approach. *Ionics (Kiel).* **1997**, *3*, 321–331.

(103) Ates, M. N.; Jia, Q.; Shah, A.; Busnaina, A.; Mukerjee, S.; Abraham, K. M. Mitigation of Layered to Spinel Conversion of a Li-Rich Layered Metal Oxide Cathode Material for Li-Ion Batteries. *J. Electrochem. Soc.* **2014**, *161*, A290–A301.

(104) Jang, D. H.; Oh, S. M. Effects of Carbon Additives on Spinel Dissolution and Capacity Losses in 4 V $Li/Li_xMn_2O_4$ Rechargeable Cells. *Electrochim. Acta* **1998**, *43*, 1023–1029.

(105) Evertz, M.; Horsthemke, F.; Kasnatscheew, J.; Börner, M.; Winter, M.; Nowak, S. Unraveling Transition Metal Dissolution of $Li_{1.04}Ni_{1/3}Co_{1/3}Mn_{1/3}O_2$ (NCM 111) in Lithium Ion Full Cells by Using the Total Reflection X-Ray Fluorescence Technique. *J. Power Sources* **2016**, *329*, 364–371.

(106) Shkrob, I. A.; Kropf, A. J.; Marin, T. W.; Li, Y.; Poluektov, O. G.; Niklas, J.; Abraham, D. P. Manganese in Graphite Anode and Capacity Fade in Li Ion Batteries. *J. Phys. Chem. C* **2014**, *118*, 24335–24348.

(107) Lee, Y. K.; Park, J.; Lu, W. A Comprehensive Experimental and Modeling Study on Dissolution in Li-Ion Batteries. *J. Electrochem. Soc.* **2019**, *166*, A1340–A1354.

(108) Tornheim, A.; Sahore, R.; He, M.; Croy, J. R.; Zhang, Z. Preformed Anodes for High-Voltage Lithium-Ion Battery Performance: Fluorinated Electrolytes, Crosstalk, and the Origins of Impedance Rise. *J. Electrochem. Soc.* **2018**, *165*, A3360–A3368.

(109) Wang, C.; Xing, L.; Vatamanu, J.; Chen, Z.; Lan, G.; Li, W.; Xu, K. Overlooked Electrolyte Destabilization by Manganese (II) in Lithium-Ion Batteries. *Nat. Commun.* **2019**, *10*,1-9.

(110) Zhang, Z.; Hu, L.; Wu, H.; Weng, W.; Koh, M.; Redfern, P. C.; Curtiss, L. A.; Amine, K. Fluorinated Electrolytes for 5 V Lithium-Ion Battery Chemistry. *Energy Environ. Sci.* **2013**, *6*, 1806–1810.

(111) Ma, L.; Young, S.; Ellis, L. D.; Huang, Q.; Ma, X.; Chatzidakis, M.; Li, H.; Thompson, L.; Eldesoky, A.; McFarlane, C. R. M.; Botton, G. A.; Hill, I. G.; Dahn, J. R. Impact of a Titanium-Based Surface Coating Applied to $Li[Ni_{0.5}Mn_{0.3}Co_{0.2}]O_2$ on Lithium-Ion Cell Performance. *ACS Appl. Energy Mater.* **2018**, *1*, 7052–7064.

(112) Burns, J. C.; Petibon, R.; Nelson, K. J.; Sinha, N. N.; Kassam, A.; Way, B. M.; Dahn, J. R. Studies of the Effect of Varying Vinylene Carbonate (VC) Content in Lithium Ion Cells on Cycling Performance and Cell Impedance. *J. Electrochem. Soc.* **2013**, *160*, A1668–A1674.

(113) Ma, X.; Harlow, J. E.; Li, J.; Ma, L.; Hall, D. S.; Buteau, S.; Genovese, M.; Cormier, M.; Dahn, J. R. Hindering Rollover Failure of $Li[Ni_{0.5}Mn_{0.3}Co_{0.2}]O_2$/Graphite Pouch Cells during Long-Term Cycling. *J. Electrochem. Soc.* **2019**, *166*, A711–A724.

(114) Harlow, J. E.; Glazier, S. L.; Li, J.; Dahn, J. R. Use of Asymmetric Average Charge-and Average Discharge-Voltages as an Indicator of the Onset of Unwanted Lithium Deposition in Lithium-Ion Cells. *J. Electrochem. Soc.* **2018**, *165*, 3595–3601.

(115) Aiken, C. P.; Xia, J.; Wang, D. Y.; Stevens, D. A.; Trussler, S.; Dahn, J. R. An Apparatus for the Study of In Situ Gas Evolution in Li-Ion Pouch Cells. *J. Electrochem. Soc.* **2014**, *161*, A1548–A1554.

(116) Lasia, A. *Electrochemical Impedance Spectroscopy and Its Applications*; Springer New York: New York, NY, 2014; Vol. 9781461489.

(117) Keefe, A. S.; Buteau, S.; Hill, I. G.; Dahn, J. R. Temperature Dependent EIS Studies Separating Charge Transfer Impedance from Contact Impedance in Lithium-Ion Symmetric Cells. *J. Electrochem. Soc.* **2019**, *166*, A3272–A3279.

(118) Yamada, Y.; Furukawa, K.; Sodeyama, K.; Kikuchi, K.; Yaegashi, M.; Tateyama, Y.; Yamada, A. Unusual Stability of Acetonitrile-Based Superconcentrated Electrolytes for Fast-Charging Lithium-Ion Batteries. *J. Am. Chem. Soc.* **2014**, *136*, 5039–5046.

(119) Poole, C. *Gas Chromatography*; Elsevier, 2014.

(120) Thompson, L. Changes to the Electrolyte in Aged Li-Ion Cells, M.Sc Thesis, Dalhousie University, 2018.

(121) RESTEK. Guide to GC Column Selection and Optimizing Separations https://www.restek.com/pdfs/GNBR1724-UNV.pdf (accessed Jul 7, 2020).

(122) Harris, D. C.; Lucy, C. A. *Quantitative Chemical Analysis*; Freeman Custom Publishing: New York, NY, 2016.

(123) Valente, I. M.; Moreira, L.; Alves, G.; Rodrigues, J. A. Another Glimpse over the Salting-out Assisted Liquid-Liquid Extraction in Acetonitrile/Water Mixtures. *J. Chromatogr. A* **2013**, *1308*, 58–62.

(124) Silverstein, R. M.; Webster, F. X.; Kiemle, D. J.; Bryce, D. L. *Spectrometric Identification of Organic Compounds*, 8th ed.; Wiley, 2014.

(125) Rankin, N. J.; Preiss, D.; Welsh, P.; Burgess, K. E. V; Nelson, S. M.; Lawlor, D. A.; Sattar, N. The Emergence of Proton Nuclear Magnetic Resonance Metabolomics in the Cardiovascular Arena as Viewed from a Clinical Perspective. *Atherosclerosis* **2014**, *237*, 287–300.

(126) Callaghan, P. T. *Principles of Nuclear Magentic Resonance Microscopy*; Oxford University Press, 1993.

(127) Wider, G.; Dreier, L. Measuring Protein Concentrations by NMR Spectroscopy. *J. Am. Chem. Soc.* **2006**, *128*, 2571–2576.

(128) Dreier, L.; Wider, G. Concentration Measurements by PULCON Using X-Filtered or 2D NMR Spectra. *Magn. Reson. Chem.* **2006**, *44* (7 SPEC. ISS.), 206–212.

(129) Haschke, M. Laboratory Micro-X-Ray Fluorescence Spectroscopy. *Springer Ser. Surf. Sci.* **2014**, *55*, 229–341.

(130) Bruker. Periodic Table of Elements and X-ray Energies Innovation with Integrity Handheld XRF https://www.bruker.com/fileadmin/user_upload/8-PDF-Docs/X-rayDiffraction_ElementalAnalysis/HH-XRF/Misc/Periodic_Table_and_X-ray_Energies.pdf (accessed Jul 7, 2020).

(131) Deutsches Elektronen-Synchrotron DESY. X-ray Fluorescence (XRF) Spectroscopy http://photon-science.desy.de/users_area/industrial_users/methods__techniques/x_ray_fluorescence_xrf_spectroscopy/index_eng.html (accessed Jul 6, 2020).

(132) Li, J.; Li, H.; Stone, W.; Glazier, S.; Dahn, J. R. Development of Electrolytes for Single Crystal NMC532/Artificial Graphite Cells with Long Lifetime. *J. Electrochem. Soc.* **2018**, *165*, A626–A635.

(133) Li, J.; Li, H.; Stone, W.; Glazier, S.; Dahn, J. R. Development of Electrolytes for Single Crystal NMC532/Artificial Graphite Cells with Long Lifetime. *J. Electrochem. Soc.* **2018**, *165*, A626–A635.

(134) Li, J.; Cameron, A. R.; Li, H.; Glazier, S.; Xiong, D.; Chatzidakis, M.; Allen, J.; Botton, G. A.; Dahn, J. R. Comparison of Single Crystal and Polycrystalline $LiNi_{0.5}Mn_{0.3}Co_{0.2}O_2$ Positive Electrode Materials for High Voltage Li-Ion Cells . *J. Electrochem. Soc.* **2017**, *164*, A1534–A1544.

(135) Madec, L.; Xia, J.; Petibon, R.; Nelson, K. J.; Sun, J. P.; Hill, I. G.; Dahn, J. R. Effect of Sulfate Electrolyte Additives on $LiNi_{1/3}Mn_{1/3}Co_{1/3}O_2$/Graphite Pouch Cell Lifetime: Correlation between Xps Surface Studies and Electrochemical Test Results. *J. Phys. Chem. C* **2014**, *118*, 29608–29622.

(136) Li, X.; Yin, Z.; Li, X.; Wang, C. Ethylene Sulfate as Film Formation Additive to Improve the Compatibility of Graphite Electrode for Lithium-Ion Battery. *Ionics (Kiel).* **2014**, *20*, 795–801.

(137) Sano, A.; Maruyama, S. Decreasing the Initial Irreversible Capacity Loss by Addition of Cyclic Sulfate as Electrolyte Additives. *J. Power Sources* **2009**, *192*, 714–718.

(138) Hall, D. S.; Allen, J. P.; Glazier, S. L.; Ellis, L. D.; Ma, L.; Peters, J. M.; Hill, I. G.; Dahn, J. R. The Solid-Electrolyte Interphase Formation Reactions of Ethylene Sulfate and Its Synergistic Chemistry with Prop-1-Ene-1,3-Sultone in Lithium-Ion Cells. *J. Electrochem. Soc.* **2017**, *164*, A3445–A3453.

(139) Smith, A. J.; Burns, J. C.; Xiong, D.; Dahn, J. R. Interpreting High Precision Coulometry Results on Li-Ion Cells. *J. Electrochem. Soc.* **2011**, *158*, 1136–1142.

(140) Henschel, J.; Horsthemke, F.; Philipp Stenzel, Y.; Evertz, M.; Girod, S.; Lürenbaum, C.; Wiemers-Meyer, S.; Winter, M.; Nowak, S. Lithium Ion Battery Electrolyte Degradation of Field-Tested Electric Vehicle Battery Cells-A Comprehensive Analytical Study. *J. Power Sources* **2020**, *447, 1-8*.

(141) Henschel, J.; Luca Schwarz, J.; Glorius, F.; Winter, M.; Nowak, S. Further Insights into Structural Diversity of Phosphorus-Based Decomposition Products in Lithium Ion Battery Electrolytes via Liquid Chromatographic Techniques Hyphenated to Ion Trap-Time-of-Flight Mass Spectrometry. *Anal. Chem* **2019**, *91*, 3980-3988.

(142) Gering, K. L. Prediction of Electrolyte Conductivity: Results from a Generalized Molecular Model Based on Ion Solvation and a Chemical Physics Framework. *Electrochim. Acta* **2017**, *225*, 175–189.

(143) Liu, Y.; Zhu, Y.; Cui, Y. Challenges and Opportunities towards Fast-Charging Battery Materials. *Nat. Energy* **2019**, *4*, 540–550.

(144) Logan, E. R.; Hall, D. S.; Cormier, M. M. E.; Taskovic, T.; Bauer, M.; Hamam, I.; Hebecker, H.; Molino, L.; Dahn, J. R. Ester-Based Electrolytes for Fast Charging of Energy Dense Lithium-Ion Batteries. *J. Phys. Chem. C* **2020**, *124*, 12269–12280.

(145) Campbell, I. D.; Marzook, M.; Marinescu, M.; Offer, G. J. How Observable Is Lithium Plating? Differential Voltage Analysis to Identify and Quantify Lithium Plating Following Fast Charging of Cold Lithium-Ion Batteries. *J. Electrochem. Soc.* **2019**, *166*, A725–A739.

(146) Petzl, M.; Danzer, M. A. Nondestructive Detection, Characterization, and Quantification of Lithium Plating in Commercial Lithium-Ion Batteries. *J. Power Sources* **2014**, *254*, 80–87.

(147) Diederichsen, K. M.; McShane, E. J.; McCloskey, B. D. Promising Routes to a High Li^+ Transference Number Electrolyte for Lithium Ion Batteries. *ACS Energy Lett.* **2017**, *2*, 2563–2575.

(148) Krachkovskiy, S. A.; Bazak, J. D.; Fraser, S.; Halalay, I. C.; Goward, G. R. Determination of Mass Transfer Parameters and Ionic Association of $LiPF_6$: Organic Carbonates Solutions . *J. Electrochem. Soc.* **2017**, *164*, A912–A916.

(149) Gallagher, K. G.; Trask, S. E.; Bauer, C.; Woehrle, T.; Lux, S. F.; Tschech, M.; Lamp, P.; Polzin, B. J.; Ha, S.; Long, B.; Wu, Q.; Lu, W.; Dees, D. W.; Jansen, A. N. Optimizing Areal Capacities through Understanding the Limitations of Lithium-Ion Electrodes. *J. Electrochem. Soc.* **2016**, *163*, A138–A149.

(150) Oldiges, K.; Diddens, D.; Ebrahiminia, M.; Hooper, J. B.; Cekic-Laskovic, I.; Heuer, A.; Bedrov, D.; Winter, M.; Brunklaus, G. Understanding Transport Mechanisms in Ionic Liquid/Carbonate Solvent Electrolyte Blends. *Phys. Chem. Chem. Phys.* **2018**, *20*, 16579–16591.

(151) Petibon, R.; Harlow, J.; Le, D. B.; Dahn, J. R. The Use of Ethyl Acetate and Methyl Propanoate in Combination with Vinylene Carbonate as Ethylene Carbonate-Free Solvent Blends for Electrolytes in Li-Ion Batteries. *Electrochim. Acta* **2015**, *154*, 227–234.

(152) Holzgrabe, U.; Wawer, I.; Diehl, B. *NMR Spectroscopy in Pharmaceutical Analysis*; Elsevier: Oxford, 2008.

(153) Stejskal, E. O.; Tanner, J. E. Spin Diffusion Measurements: Spin Echoes in the Presence of a Time-Dependent Field Gradient. *J. Chem. Phys.* **1965**, *42*, 288–292.

(154) Bertram, M. Gradients in NMR Spectroscopy – Part 5_ The Pulsed Gradient Spin Echo (PGSE) Experiment _ Magritek https://magritek.com/2016/07/18/gradients-in-nmr-spectroscopy-part-5-the-pulsed-gradient-spin-echo-pgse-experiment/ (accessed Jul 12, 2020).

(155) Feng, Z.; Higa, K.; Han, K. S.; Srinivasan, V. Evaluating Transport Properties and Ionic Dissociation of LiPF 6 in Concentrated Electrolyte. *J. Electrochem. Soc.* **2017**, *164*, A2434–A2440.

(156) Valøen, L. O.; Reimers, J. N. Transport Properties of $LiPF_6$-Based Li-Ion Battery Electrolytes. *J. Electrochem. Soc.* **2005**, *152*, A882.

(157) Stolwijk, N. A.; Kösters, J.; Wiencierz, M.; Schönhoff, M. Electrochimica Acta On the Extraction of Ion Association Data and Transference Numbers from Ionic Diffusivity and Conductivity Data in Polymer Electrolytes. *Electrochim. Acta* **2013**, *102*, 451–458.

(158) Ma, X.; Li, J.; Glazier, S. L.; Ma, L.; Gering, K. L.; Dahn, J. R. A Study of Highly Conductive Ester Co-Solvents in $Li[Ni_{0.5}Mn_{0.3}Co_{0.2}]O_2$/Graphite Pouch Cells. *Electrochim. Acta* **2018**, *270*, 215–223.

(159) Li, M.; Lu, J.; Chen, Z.; Amine, K. 30 Years of Lithium-Ion Batteries. *Adv. Mater.* **2018**, *30*, 1–24.

(160) Peled, E.; Menkin, S. Review-SEI: Past, Present and Future. *J. Electrochem. Soc.* **2017**, *164*, 1703–1719.

(161) Krachkovskiy, S. A.; Bazak, J. D.; Fraser, S.; Halalay, I. C.; Goward, G. R. Determination of Mass Transfer Parameters and Ionic Association of $LiPF_6$: Organic Carbonates Solutions. *J. Electrochem. Soc.* **2017**, *164*, A912–A916.

(162) Anastas, P.; Eghbali, N. Green Chemistry: Principles and Practice. *Chem. Soc. Rev.* **2010**, *39*, 301–312.

(163) Dedryvère, R.; Leroy, S.; Martinez, H.; Blanchard, F.; Lemordant, D.; Gonbeau, D. XPS Valence Characterization of Lithium Salts as a Tool to Study Electrode/Electrolyte Interfaces of Li-Ion Batteries. *J. Phys. Chem. B* **2006**, *110*, 12986–12992.

(164) Zhang, S. S.; Xu, K.; Jow, T. R. Low-Temperature Performance of Li-Ion Cells with a LiBF4-Based Electrolyte. *J. Solid State Electrochem.* **2003**, *7*, 147–151.

(165) What is Benchtop NMR? Uses of Benchtop NMR Spectroscopy https://www.nanalysis.com/what-is-benchtop-nmr (accessed Jul 17, 2020).

(166) Genovese, M.; Louli, A. J.; Weber, R.; Martin, C.; Taskovic, T.; Dahn, J. R. Hot Formation for Improved Low Temperature Cycling of Anode-Free Lithium Metal Batteries. *J. Electrochem. Soc.* **2019**, *166*, 3342–3347.

(167) Su, C. C.; He, M.; Amine, R.; Chen, Z.; Amine, K. Internally Referenced DOSY-NMR: A Novel Analytical Method in Revealing the Solution Structure of Lithium-Ion Battery Electrolytes. *J. Phys. Chem. Lett.* **2018**, *9*, 3714–3719.

(168) Chapman, N.; Borodin, O.; Yoon, T.; Nguyen, C. C.; Lucht, B. L. Spectroscopic and Density Functional Theory Characterization of Common Lithium Salt Solvates in Carbonate Electrolytes for Lithium Batteries. *J. Phys. Chem. C* **2017**, *121*, 2135–2148.

APPENDIX A- LICENSE AGREEMENTS

Lithium Ion Battery Graphite Solid Electrolyte Interphase Revealed by Microscopy and Spectroscopy

Author: Mengyun Nie, Dinesh Chalasani, Daniel P. Abraham, et al
Publication: The Journal of Physical Chemistry C
Publisher: American Chemical Society
Date: Jan 1, 2013

PERMISSION/LICENSE IS GRANTED FOR YOUR ORDER AT NO CHARGE

This type of permission/license, instead of the standard Terms & Conditions, is sent to you because no fee is being charged for your order. Please note the following:

- Permission is granted for your request in both print and electronic formats, and translations.
- If figures and/or tables were requested, they may be adapted or used in part.
- Please print this page for your records and send a copy of it to your publisher/graduate school.
- Appropriate credit for the requested material should be given as follows: "Reprinted (adapted) with permission from (COMPLETE REFERENCE CITATION). Copyright (YEAR) American Chemical Society." Insert appropriate information in place of the capitalized words.
- One-time permission is granted only for the use specified in your request. No additional uses are granted (such as derivative works or other editions). For any other uses, please submit a new request.

BACK CLOSE WINDOW

Copyright Clearance Center Marketplace™

Royal Society of Chemistry - License Terms and Conditions

This is a License Agreement between Tina Taskovic ("You") and Royal Society of Chemistry ("Publisher") provided by Copyright Clearance Center ("CCC"). The license consists of your order details, the terms and conditions provided by Royal Society of Chemistry, and the CCC terms and conditions.

All payments must be made in full to CCC.

Order Date	16-Jul-2020	Type of Use	Republish in a thesis/dissertation
Order license ID	1049003-1	Publisher	ROYAL SOCIETY OF CHEMISTRY
ISSN	1463-9084	Portion	Chart/graph/table/figure

LICENSED CONTENT

Publication Title	Physical chemistry chemical physics	Country	United Kingdom of Great Britain and Northern Ireland
Author/Editor	Royal Society of Chemistry (Great Britain)	Rightsholder	Royal Society of Chemistry
Date	01/01/1999	Publication Type	e-Journal
Language	English	URL	http://firstsearch.oclc.org/journal=1463-9076;screen=info;ECOIP

REQUEST DETAILS

Portion Type	Chart/graph/table/figure	Distribution	Worldwide
Number of charts / graphs / tables / figures requested	1	Translation	Original language of publication
Format (select all that apply)	Electronic	Copies for the disabled?	No
Who will republish the content?	Academic institution	Minor editing privileges?	No
Duration of Use	Life of current edition	Incidental promotional use?	No
Lifetime Unit Quantity	Up to 499	Currency	CAD
Rights Requested	Main product		

NEW WORK DETAILS

Title	COMPOSITIONAL AND FUNDAMENTAL CHARACTERIZATION OF LI-ION CELL ELECTROLYTES	Institution name	Dalhousie University
Instructor name	Tina Taskovic	Expected presentation date	2020-08-14

ADDITIONAL DETAILS

Order reference number	N/A	**The requesting person / organization to appear on the license**	Tina Taskovic

REUSE CONTENT DETAILS

Title, description or numeric reference of the portion(s)	Figure 13	**Title of the article/chapter the portion is from**	Mechanism of action of ethylene sulfite and vinylene carbonate electrolyte additives in LiNi1/3Mn1/3Co1/3O2/graphit pouch cells: electrochemical, GC-MS and XPS analysis
Editor of portion(s)	N/A		
Volume of serial or monograph	N/A		
Page or page range of portion	27074	**Author of portion(s)**	Royal Society of Chemistry (Great Britain)
		Issue, if republishing an article from a serial	N/A
		Publication date of portion	2015-01-21

CCC Republication Terms and Conditions

1. Description of Service; Defined Terms. This Republication License enables the User to obtain licenses for republication of one or more copyrighted works as described in detail on the relevant Order Confirmation (the "Work(s)"). Copyright Clearance Center, Inc. ("CCC") grants licenses through the Service on behalf of the rightsholder identified on the Order Confirmation (the "Rightsholder"). "Republication", as used herein, generally means the inclusion of a Work, in whole or in part, in a new work or works, also as described on the Order Confirmation. "User", as used herein, means the person or entity making such republication.

2. The terms set forth in the relevant Order Confirmation, and any terms set by the Rightsholder with respect to a particular Work, govern the terms of use of Works in connection with the Service. By using the Service, the person transacting for a republication license on behalf of the User represents and warrants that he/she/it (a) has been duly authorized by the User to accept, and hereby does accept, all such terms and conditions on behalf of User, and (b) shall inform User of all such terms and conditions. In the event such person is a "freelancer" or other third party independent of User and CCC, such party shall be deemed jointly a "User" for purposes of these terms and conditions. In any event, User shall be deemed to have accepted and agreed to all such terms and conditions if User republishes the Work in any fashion.

3. Scope of License; Limitations and Obligations.

   3.1. All Works and all rights therein, including copyright rights, remain the sole and exclusive property of the Rightsholder. The license created by the exchange of an Order Confirmation (and/or any invoice) and payment by User of the full amount set forth on that document includes only those rights expressly set forth in the Order Confirmation and in these terms and conditions, and conveys no other rights in the Work(s) to User. All rights not expressly granted are hereby reserved.

   3.2. General Payment Terms: You may pay by credit card or through an account with us payable at the end of the month. If you and we agree that you may establish a standing account with CCC, then the following terms apply: Remit Payment to: Copyright Clearance Center, 29118 Network Place, Chicago, IL 60673-1291. Payments Due: Invoices are payable upon their delivery to you (or upon our notice to you that they are available to you for downloading). After 30 days, outstanding amounts will be subject to a service charge of 1-1/2% per month or, if less, the maximum rate allowed by applicable law. Unless otherwise specifically set forth in the Order Confirmation or in a separate written agreement signed by CCC, invoices are due and payable on "net 30" terms. While User may exercise the rights licensed immediately upon issuance of the Order Confirmation, the license is automatically revoked and is null and void, as if it had never been issued, if

ELSEVIER LICENSE
TERMS AND CONDITIONS

Jul 16, 2020

This Agreement between Dalhousie University -- Tina Taskovic ("You") and Elsevier ("Elsevier") consists of your license details and the terms and conditions provided by Elsevier and Copyright Clearance Center.

License Number	4871090658578
License date	Jul 16, 2020
Licensed Content Publisher	Elsevier
Licensed Content Publication	Energy Storage Materials
Licensed Content Title	How electrolyte additives work in Li-ion batteries
Licensed Content Author	Yunxian Qian,Shiguang Hu,Xianshuai Zou,Zhaohui Deng,Yuqun Xu,Zongze Cao,Yuanyuan Kang,Yuanfu Deng,Qiao Shi,Kang Xu,Yonghong Deng
Licensed Content Date	Jul 1, 2019
Licensed Content Volume	20
Licensed Content Issue	n/a
Licensed Content Pages	8
Start Page	208
End Page	215

Type of Use	reuse in a thesis/dissertation
Portion	figures/tables/illustrations
Number of figures/tables/illustrations	5
Format	electronic
Are you the author of this Elsevier article?	No
Will you be translating?	No
Title	COMPOSITIONAL AND FUNDAMENTAL CHARACTERIZATION OF LI-ION CELL ELECTROLYTES
Institution name	Dalhousie University
Expected presentation date	Aug 2020
Portions	Figure 5
Requestor Location	Dalhousie University 5885 spring garden raod unit 903 Halifax, NS B3H1Y3 Canada Attn: Dalhousie University
Publisher Tax ID	GB 494 6272 12
Total	0.00 CAD
Terms and Conditions	

INTRODUCTION

Identification of Electrolyte-Soluble Organic Cross-Talk Species in a Lithium-Ion Battery via a Two-Compartment Cell

Author: Ritu Sahore, Fulya Dogan, Ira D. Bloom
Publication: Chemistry of Materials
Publisher: American Chemical Society
Date: Apr 1, 2019

Promising Routes to a High Li Transference Number Electrolyte for Lithium Ion Batteries

Author: Kyle M. Diederichsen, Eric J. McShane, Bryan D. McCloskey
Publication: ACS Energy Letters
Publisher: American Chemical Society
Date: Nov 1, 2017